



UNIVERSITÀ DI PISA

FACOLTÀ DI SCIENZE MATEMATICHE, FISICHE E  
NATURALI

CORSO DI LAUREA MAGISTRALE IN FISICA TEORICA

# New Directions for Causal Dynamical Triangulations

*Author*

Giuseppe CLEMENTE

*Supervisor*

Prof. Massimo D'ELIA

Master Thesis

Pisa, 21 September 2017



# New Directions for Causal Dynamical Triangulations

A numerical approach to Quantum Gravity

Giuseppe Clemente

## Abstract

The purpose of this study is to investigate and propose new algorithms and methods of analysis in the context of the Causal Dynamical Triangulations (CDT) approach to Quantum Gravity.

Grounded upon Markov Chain Monte-Carlo methods and physical insight from the Wilsonian Renormalization Group framework, the CDT research program is acquiring growing interest because of recent observations strongly supporting the presence of continuous order critical points in the phase diagram of 4D simulations. This could validate the *asymptotic safety* conjecture advanced by Weinberg in 1976, stating the existence of a non-Gaussian UV fixed point around which one could renormalize non-perturbatively the Einstein-Hilbert gravity with cosmological constant, then opening the possibility to explore quantum-gravitational effects by lattice regularization. Research in this direction is currently being undertaken by Ambjorn et al..

In the first part of this thesis, an overview of the CDT program is presented, and numerical methods are discussed.

The algorithm currently adopted by the CDT community is analyzed in detail and implemented in C++; moreover, a new class of algorithms, generalizing the standard one and named TBlocked, is proposed in order to cure the presence of slow modes in a region of the phase diagram, but gives also the opportunity to parallelize the standard algorithm.

Simulation results and a validation of some standard results are presented, and the standard and TBlocked implementations are compared.

In the last part of this thesis the current lack of definitions for observables in pure-gauge gravity is discussed; in particular, no observable encoding geometric features in a satisfactory way has been found in the foregoing literature on CDT.

Driven by this need, a new and almost complete class of observables characterizing geometric properties of the spatial slices is proposed, based upon the analysis of eigenvalues and eigenvectors of the Laplace-Beltrami matrices associated with the graph dual to the slices. This method, that actually pertains to the realm of spectral graph theory, acts like a Fourier transform generalized on graphs, and gives sense to previously inaccessible concepts in CDT, like a coarse-grained definition of the scalar curvature or of any microscopically defined observable, straightforward to define for regular lattices but not so obvious for random lattices. Main results are obtained and discussed, but this work does not exhaust all the types of analysis that are enabled by this method.

It is in the hopes of the author to investigate further applications and generalizations of this method in the future.

# Acknowledgements

I am grateful to my family and friends, who have always encouraged my passions and endured my flaws and my absence in recent times.

Special thanks to my aunt Adele, who believe in my future and gave me significant moral and economical support, my friend Enrico, who helped me with some drawing of the thesis, and finally my supervisor Massimo, who, amongst his many commitments, found always the time to follow my researches and give me firm advices.

# Contents

<b>1</b>	<b>Introduction</b>	<b>6</b>
1.1	Quantum Gravity approaches . . . . .	7
1.1.1	Non-conservative approaches . . . . .	7
1.1.2	Conservative approaches . . . . .	8
1.2	Introduction to Causal Dynamical Triangulations . . . . .	10
1.3	Aims and structure of the thesis . . . . .	12
<b>2</b>	<b>Overview of Causal Dynamical Triangulation</b>	<b>14</b>
2.1	The path-integral formalism . . . . .	14
2.1.1	Path-integral for field theories and analytic continuation . . . . .	16
2.2	Discretization: the Regge action . . . . .	18
2.3	Wick rotation . . . . .	24
2.3.1	Volume fixing . . . . .	25
2.4	Renormalization Group . . . . .	26
2.4.1	Asymptotic safety . . . . .	30
2.5	Current state of the research in CDT . . . . .	31
2.5.1	Overview of the phase diagram . . . . .	31
2.5.2	Hunting for observables in Quantum Gravity . . . . .	33
2.5.3	Continuum limit and RG transformation in CDT . . . . .	34
<b>3</b>	<b>Numerical Implementation</b>	<b>35</b>
3.1	Detailed Balance . . . . .	36
3.2	Alexander moves . . . . .	39
3.2.1	Alexander moves in 2D . . . . .	40
3.2.2	Alexander moves in 3D . . . . .	41
3.2.3	Alexander moves in 4D . . . . .	44
3.3	Description and analysis of the standard algorithm . . . . .	48
3.3.1	Example: acceptance probability computation in 3D . . . . .	50
3.4	A modification to the standard algorithm: the TBlocked algorithms . . . . .	51
3.4.1	Steps and detailed balance for a general TBlocked algorithm . . . . .	52
3.4.2	Further generalizations and applications . . . . .	54
<b>4</b>	<b>Simulation results</b>	<b>55</b>
4.1	Phase diagram . . . . .	55
4.1.1	Spatial volume distribution in the different phases . . . . .	55
4.1.2	Validation of the phase diagram . . . . .	58
4.2	De Sitter phase . . . . .	63
4.2.1	Profile of the universe . . . . .	63
4.2.2	Spectral dimension . . . . .	65

4.2.3	Numerical resources . . . . .	69
4.3	Tests for the TBlocked algorithm . . . . .	70
4.3.1	Average estimates compatibility . . . . .	70
4.3.2	Comparison of efficiency for the Standard and TBlocked algorithms . . . . .	70
<b>5</b>	<b>Laplace-Beltrami spectral analysis</b>	<b>76</b>
5.1	Motivations . . . . .	76
5.1.1	Spectral analysis of local observables . . . . .	81
5.2	Properties of the eigenspectrum of the Laplace-Beltrami matrix . . . . .	82
5.2.1	Interpretation of the first eigenvalues and eigenvectors . . . . .	82
5.2.2	Heat-kernel expansion and McKean-Singer coefficients . . . . .	84
5.3	Spectral graph analysis on Euclidean slices . . . . .	87
5.4	An alternative derivation of the spectral dimension . . . . .	89
5.4.1	Spectral dimension for simple cases . . . . .	89
5.4.2	Spectral dimension of spatial slices in CDT . . . . .	92
5.5	Visualizing large-scale structures: Laplacian eigenmaps . . . . .	94
5.5.1	Example: eigenmaps of tori . . . . .	95
5.5.2	2D and 3D eigenmaps of a spatial slice . . . . .	95
5.6	Analysis of the spectra of eigenvalues . . . . .	101
5.6.1	Correlation of eigenvalues in the slice time direction . . . . .	102
5.7	Analysis of the spatial scalar curvature . . . . .	103
5.8	Generalizations of the Laplace-Beltrami analysis . . . . .	106
5.8.1	Generalization to the full triangulation . . . . .	106
5.8.2	Applications to matter coupling . . . . .	109
<b>6</b>	<b>Conclusions</b>	<b>110</b>
<b>Appendix A</b>	<b>Data structures</b>	<b>113</b>
A.1	Data structures for the standard implementation . . . . .	113
A.2	Data structures for the TBlocked implementation . . . . .	116
<b>Appendix B</b>	<b>Scalar curvature on the slices</b>	<b>118</b>

# Chapter 1

## Introduction

Theoretical physics is today facing one of the most difficult challenges of the last century, namely the unification of Quantum Mechanics and Gravitation, the quest for a theory of Quantum Gravity (QG). There is a certain number of issues that make this research arduous. First of all, experimental tests to probe quantum properties of spacetime are not yet available, since the energy scale that is estimated to allow these observations is of the order of the Planck Energy ( $E_{Pl} \equiv m_{Pl}c^2 \equiv \sqrt{\frac{\hbar c}{G}}c^2 = 1,22 \times 10^{19}$  GeV). Nevertheless, some QG phenomenology from cosmological observations (like the gravitational B-mode polarization) or gravity-induced quantum effects (like spin-foam decoherence) could be useful to cut out or constrain QG theories in a recent future. Secondly, standard perturbative methods fail to quantize the Einstein gravity, suggesting that new degrees of freedom enter the scene at Planckian scales. To see why, let us consider the 4D Einstein-Hilbert (EH) action

$$S_{EH} = \frac{1}{16\pi G} \int d^4x \sqrt{-g} (R - 2\Lambda), \quad (1.1)$$

where  $R$  is the *Ricci curvature scalar*,  $G$  is the *Newton constant*, and  $\Lambda$  is the *cosmological constant*. Since the mass dimension of the spacetime measure is  $-4$ , and that of the Ricci scalar is  $+2$ , to yield a dimensionless action the coefficient  $1/G$  must possess positive mass dimension  $+2$  (indeed  $1/G = \frac{m_{Pl}^2}{\hbar c}$ ), making the EH theory non-renormalizable by power counting. For theories with dimensionless coupling constants like QED or QCD, the loop momentum divergences are logarithmic and can usually be renormalized at all orders of the loop expansion by introducing a finite number of counterterms. This is not the case of the EH theory: for each loop in the Feynman diagram expansion about a flat background, due to the mass dimension  $2$  of  $1/G$ , two more powers of loop momentum in the numerator are needed to make the expression dimensionless. Divergences, dominated by the high-momentum sector of the loop integrals, worsen for increasing loop order in the expansion. This kind of divergences are called *ultraviolet* in the standard terminology, and are associated to short scales or equivalently high-energies/momenta. It can be shown, already from the two loop expansion, that for the Einstein-Hilbert theory an infinite number of counterterms (and then coefficients) should be introduced to remove ultraviolet divergences [1].

## 1.1 Quantum Gravity approaches

The obvious reaction to the previous result is to regard the Einstein description of gravity not as a fundamental theory, but as an effective theory, that is, only valid in the range of energy scales much lower than the Planck Mass, or equivalently, valid for scales much larger than the Planck Length ( $l_{Pl} \equiv \sqrt{\frac{\hbar G}{c^3}} \simeq 1.6 \times 10^{-35}\text{m}$ ). This observation is not such a big deal for most physicists, but from the point of view of a theoretician it is really unsatisfactory, since it represents a huge lack in our understanding of nature at the fundamental level.

It was not the first time in theoretical physics that a theory accurate at low energies turned out to be non-renormalizable. For example, the Fermi theory of beta decays is non-renormalizable by power counting (the Fermi constant  $G_F$  has mass dimension -2); however, today we know that it is only the low energy limit ( $E \ll M_W, M_Z$ ) of the more accurate theory of electroweak interactions.

So, it was historically expected that a new and more general theory of Quantum Gravity should exist, with the Einstein gravity theory as low energy limit. In this section we will describe briefly some of the most popular approaches to the quantum gravity problem. This list is by no means exhaustive, and the order is not by importance. An introduction to some popular approaches is given in [2]. We apologize in advance with researchers that follow approaches not mentioned here.

### 1.1.1 Non-conservative approaches

We shall use the term ‘non-conservative’ to identify all approaches of Quantum Gravity that are based on the introduction of different or additional degrees freedom with respect to the ones characterizing the Einstein gravity.

#### String theory

String theory certainly belongs to the class of non-conservative approaches of quantum gravity. It was originally formulated to describe strong interactions before quantum chromodynamics (QCD) was identified as the correct candidate. However, today it is considered by a large number of theoreticians a good candidate for a “theory of everything”, and by inclusion also a theory of Quantum Gravity. The main idea is that point-like particles are replaced by one-dimensional (string-like) objects. This also makes the theory free from the ultraviolet divergences discussed previously.

The spectrum of vibrational states of the strings characterize the properties of the emerging particles like mass or spin. The reason for which string theory is interesting for the QG problem is that it admits the existence of a massless spin 2 vibrational mode in the spectrum, that has been identified as the “graviton”, a hypothetical bosonic particle carrier of the gravitational interaction. Unfortunately, the theory requires more than four dimensions to be mathematically consistent, so also a mechanism of *dimensional reduction*<sup>1</sup> must be introduced in order to make the extra dimensions undetectable.

---

<sup>1</sup>In CDT, the term dimensional reduction is also used, but to indicate another effect. See section 4.2.2.

Research in string theory gave big contributions to mathematics, and evolved in many directions, like the study of the *AdS/CFT* correspondence. However, today it is not known yet to which extent string theory describes real world physics and which form one should work with.

### Causal sets

Another non-conservative approach to QG is *Causal sets* theory. The fundamental discreteness of the spacetime is assumed from the onset, and is represented by causal sets, sets of elementary physical points embedded on a Lorentzian manifold and equipped with a partial ordering encoding causality relations between them (informally, telling which one comes first and which later). This approach is motivated by the observation that the mere causal structure of a spacetime stores a remarkable amount of information, and is actually sufficient to determine the conformal class of the spacetime.

One needs to introduce a dynamics for causal sets, that is a rule for determining the most physically realizable causal structures from the quantum point of view, sought in the form of a path-integral<sup>2</sup>.

However, the appropriate dynamics that should be used to get physical results is still under active research by the causal sets community.

### 1.1.2 Conservative approaches

Another, less obvious, reaction to the result of non-renormalizability of QG is given by the so-called ‘conservative’ approaches, that do not give up on the Einstein formulation of gravity.

#### Loop quantum gravity

Maybe the simplest thing that could be thought to work around the ultraviolet divergences, still using the Einstein degrees of freedom, is postulating fundamental discreteness of space-time. Loop Quantum Gravity (LQG) [3] is the main approach following this philosophy. The Einstein theory is rephrased into the Einstein-Cartan<sup>3</sup> and in the Hamiltonian formalism. A Hilbert space of loop representations is constructed, and from quantization of operators on this space the granularity of space-time emerges with a scale of the order of the Planck scale.

The crucial point of LQG is the assumption that the information about states of the Hilbert space can be encoded by one-dimensional structures like loops and graphs. These structures are taken as a fundamental, and no continuum limit is actually performed. This is motivated by the observation that, being the Einstein theory invariant with respect to arbitrary diffeomorphisms, shrinking the lattice spacing does

---

<sup>2</sup>Generalities about the path-integral will be discussed in sec. 2.1, since it also the language on which it is formulated Causal Dynamical Triangulations, the approach investigated in this thesis. However, the configuration space of the latter, described by causal triangulations, is different from the one of causal sets, described by points with causal relations.

<sup>3</sup>The Einstein-Cartan theory is a generalization of the Einstein-Hilbert theory, and make manifest the interpretation of gravity as a gauge theory. It reduces to Einstein gravity if one does not take into account fermions, that make the torsion non-null. Here we consider conservative also theories based on the Einstein-Cartan formulation.

not change the physics since it is the lattice itself that encodes metrical information, not coordinates. Some specific types of directed graphs, called *spin networks* are eigenstates of the Area and Volume operators, that therefore turn out to be quantized making the spacetime granular. Many results have been derived, but, unfortunately, no semi-classical limit of LQG is still available.

### Causal dynamical triangulations

The instance of non-renormalizability presented above seems to cut out the possibility of a QG theory which is both conservative and continuum (i.e. valid on all scales, especially the smaller ones). However, there is another conservative approach called *Causal Dynamical Triangulations* (CDT), the leading actor of this thesis, that, despite the failure of perturbative renormalization, seeks an ultraviolet limit for the Einstein-Hilbert action by performing non-perturbative numerical simulations with Monte-Carlo methods. In Monte-Carlo simulations of quantum field theories, discreteness of the spacetime is introduced in the form of a lattice to make numerical computations possible in practice, but the ultraviolet limit, called “continuum limit” in technical terminology, has still to be found. This corresponds to the shrinking of the physical lattice spacing  $a \rightarrow 0$ , that can be controlled by the free parameters  $\vec{g} \equiv (g_1, g_2, \dots)$  of the theory.

In order to make this shrinking actually possible, microscopic details of the artificial lattice must disappear in the continuum limit in such a way that the typical scales  $\xi_s$  at which the physical fields and observables change, called *correlation lengths*, are kept much larger than the lattice spacing for  $a \rightarrow 0$ . So the continuum limit, if it exists, is attained only for a particular value of the free parameters  $\vec{g}_0$  for which the limit  $\vec{g} \rightarrow \vec{g}_0$  implies a shrinking of the lattice for fixed correlation lengths, or equivalently, diverging correlation lengths in lattice units  $\frac{\xi_s(\vec{g})}{a(\vec{g})} \rightarrow \infty$ .

In statistical physics, a diverging correlation length signals a critical behaviour of the system which undergoes a continuous transition<sup>4</sup>, and a phase diagram is built, representing the regions in the space of control parameters of the theory for which the behavior of the system is radically different (the so-called *phases*). The critical behavior of water or superconductivity for example can be described by a phase diagram, where lines between the phases are physically interesting since crossing them a phase transition happens.

Similarly, in quantum field theory with Monte-Carlo methods, one can build a phase diagram by performing simulations for different values of the free parameters of the theory  $\vec{g}$ , and study the behaviour of observables, called *order parameters*, which are related to the symmetries of the system. The *order parameter* associated to a transition<sup>5</sup>, said informally, quantifies how much a given symmetry of the theory is broken on average in the configurations sampled, and in the thermodynamic limit (infinite volumes) discriminates the transition line by taking distinct values on the two sides of it<sup>6</sup>.

---

<sup>4</sup>The terms “second-order phase transition” and “continuous phase transition” are interchangeable.

<sup>5</sup>It is not always possible to define an order parameter associated to a transition. For example, in the 2-dimensional XY model a continuous transition happen, called KosterlitzThouless transition, but no symmetry is actually broken.

<sup>6</sup>In our definitions of order parameter we do not require it to be zero in one phase and different from zero in the other (like magnetization for example); any pair of distinct values is allowed, since

It can be shown that microscopical information about the lattice could fade only for simulations running near a specific kind of transition line, called a *continuous order transition line*, for which the relevant observables change in a continuous way for arbitrarily large lattices. The ultimate aim of lattice simulations of quantum field theories, and therefore also of CDT simulations, is to represent continuum data, and for this to be possible it is necessary to study the phase diagram of the theory, and identify points of continuous phase transitions with diverging correlation lengths. To explain how the CDT approach could overcome the results of naive perturbation theory previously shown, we should analyze why the latter fails, and discuss how we can get around its divergences. Some questions are in order. First of all, is it meaningful to perturbatively expand around a specific (e.g. flat) background metric for the Einstein-Hilbert theory, which is intrinsically background independent? Background independence means that the formalism does not make any assumption about the actual shape of the spacetime. For matter fields the perturbation expansion is done with respect to the free vacuum, that is the low energy level of the free fields, but which should the vacuum in QG be? Secondly, renormalized quantities calculated in perturbation theory are truncated power series in the coupling coefficients, whereby the latter must be somewhat small for the whole approach to be consistent.

As shown before, naive perturbation theory does not work for Einstein gravity, but there is the possibility that the very renormalizability of the theory turns out to be a non-perturbative feature. This means that the phase diagram of gravity could indeed contain a point of continuous phase transition and diverging correlation length, but since perturbation theory fails, if it exists it must correspond to a theory with finite (non vanishing) coupling parameters. The existence of such a non-perturbative point, around which the theory is renormalizable, is at the heart of the Weinberg's conjecture named *asymptotic safety*.

Today we possess non-perturbative tools, that have been applied with success to perturbatively non-renormalizable theories like the *non-linear sigma model* or *Gross-Neveu models*. Non-perturbative techniques that can be used to test the asymptotic safety scenario are given by numerical simulations with Monte Carlo methods on lattices, where the quantum field theory is rephrased in the path-integral formalism, and the continuum limit, if it exists, can be attained by performing simulations near a continuous critical point in the phase diagram with diverging correlation length. This is the case of CDT, which will be discussed more in detail in subsequent chapters; in the following sections we will just describe the main features of CDT, and the structure of this thesis.

## 1.2 Introduction to Causal Dynamical Triangulations

*Causal Dynamical Triangulations* (CDT) [4] can be classified as a conservative, non-perturbative, background independent approach to Quantum Gravity, that applies Monte Carlo methods in a lattice regularization of the Einstein-Hilbert gravity via Regge triangulations. Numerical simulations are limited by memory requirements

---

it can always be redefined by an affine transformation.

of computers, so it is necessary to represent the configuration space of the theory, consisting of spacetime geometries  $(\mathcal{M}, g_{\mu\nu})$ , by discretizing the degrees of freedom. Furthermore, the discretization procedure, by means of the introduction of a certain lattice size  $a$ , makes the problem of searching a continuum limit well posed, as we argued above.

The representation used in CDT is given by the background independent formalism of *Regge calculus* [5], for which a smooth spacetime manifold is approximated by a piecewise flat *simplicial manifold*, where the flat elementary building blocks, called *simplexes* (or *simplices*), are glued to each others in order to form the spacetime geometry (see sec. 2.2). The *triangulation* attribute of CDT comes from this choice of discretization, since the “simplest simplices” used to approximate 2D surfaces are triangles glued each others by their sides (as for the meshes in 3D modeling). To represent 4D spacetimes, the simplexes of maximal dimension used are actually *pentachorons*, four-dimensional volume elements bounded by five tetrahedra.

We want to stress that these triangulations should not be intended as embedded in some coordinate system; they are treated as an abstract collection of geometrical entities (simplices) and relations between them. Furthermore, for technical reasons (explained in cap. 2), the triangulations used in CDT are also “causal”, which means that the triangulation is not equivalent to an Euclidean one, but the gluing of simplexes is constrained to preserve local causality. In particular, spacetime is *foliated*<sup>7</sup> into a set of spacelike surfaces  $\{\Sigma_t\}$  with fixed topology, labeled by their time coordinate  $t$ , so that vertices of the triangulation are restricted to lie on spatial slices, and *pentachorons* fill the spacetime between different slices.

On these Lorentzian triangulations then, an analytic continuation of the discretized action to the Euclidean space is performed (see sec. 2.3), but the causal structure persists. This feature is the one that distinguish CDT from the older approach to Quantum Gravity in the asymptotic safety scenario, called *Dynamical Triangulations* (DT) [6, 7]. The configuration space of DT consists of triangulations embedded on an Euclidean space from the onset (Regge action for a Riemannian manifold), and without the imposition of any causal structure. Causality observed in nature is explained in DT as emergent from a symmetry breaking of the spacetime isotropy. However the phase diagram of DT, does not seem to contain physically interesting phases. Nevertheless, recent results suggest that CDT may be a sort of effective theory with respect to DT, since in CDT topology changes are not allowed [8].

Finally, the term “dynamical” in CDT refers to the Monte-Carlo sampling of configurations by means of the path-integral formalism (see section 2.1). As will be explained in sec. 2.1.1, to every triangulation  $\mathcal{T}$  a probability is assigned, proportional to  $\mathcal{P}[\mathcal{T}] \propto e^{-S[\mathcal{T}]}$ , where  $S$  is the analytically continued Regge action. *Metropolis importance sampling* is a Monte-Carlo technique consisting in a properly defined local update of the triangulation at each step of the simulation (see chap. 3). In this way one obtains a set  $\{\mathcal{T}_i\}$  of configurations sampled according to the probability distribution  $\mathcal{P}[\mathcal{T}]$ . Observables  $\mathcal{O}[\mathcal{T}]$  are then computed from properties of the triangulations  $\mathcal{T}$ , such as the number of vertices or simplexes of a given type, and then

---

<sup>7</sup>Besides CDT, the formalism of foliations, also called ADM decomposition, is adopted by a wide class of classical and quantum approaches to gravity, like simulations in Numerical Relativity and Loop Quantum Gravity. The existence of a foliation corresponds to the assumption of *global hyperbolicity*, which means that spacetimes are both causal and such that the intersection of the past and future cones of two different points is compact.

their expectation values  $\langle \mathcal{O} \rangle$  is estimated by averaging over the sample

$$\overline{\mathcal{O}} = \sum_i \mathcal{O}[\mathcal{T}_i] \mathcal{P}[\mathcal{T}_i]. \quad (1.2)$$

There are many interesting results that make CDT an appealing theory of quantum gravity.

First of all, CDT has been proved to satisfy the *reflection positivity* property (chapter 3 of [4]), which is the Euclidean equivalent of the Lorentzian condition of *unitarity*. Unitarity is probably the most important request of consistency for any quantum theory, since is the necessary condition for having conservation of probabilities.

Secondly, the presence of two continuous order critical lines in the phase diagram, one of which only recently discovered [9], are encouraging to the quest for the continuum limit. However, further analysis must be undertaken to locate, if it exists, which point in this lines has diverging correlation lengths, and if the resulting continuum theory correctly represents physical data.

We must not forget to mention one of the most striking results of CDT: the emergence of a phase where the averaged global shape of the triangulations (in the sense defined in sec. 4.2) fits very well with that of a *de Sitter universe* with fluctuations, which is actually the best cosmological model for our physical universe. This is really surprising, since a dynamical background geometry arises, on its own, from a background independent approach.

This and other results would be discussed in detail in chap. 4.

### 1.3 Aims and structure of the thesis

In this thesis we have not focused on the continuum limit for two reasons: it usually requires a lot of time and resources (because of the characteristic slowing down of the algorithms near a critical point), and it is already being currently investigated by other groups. Instead, we have followed other directions, that ultimately we consider relevant also for the sake of the search of the continuum limit: on one hand we analyzed and generalized the algorithmic setup of the simulations (chapter 3), on the other hand we defined a new class of observables that characterize geometries (chapter 5).

The subjects of this thesis are organized as follows.

In the following chapter (2) we will give an overview of the foundations of CDT, and will discuss in detail the path-integral formalism, Regge discretization, analytic continuation, and some preliminary results about the phase diagram.

Chapter 3 examines algorithmic issues. Here Monte-Carlo importance sampling methods are discussed, as well as how to build a working implementation of CDT simulation. In particular, the algorithm currently used by the CDT community is analyzed, and a new class of algorithms, called *TBlocked*, is proposed in order to deal with some slow modes identified in the de Sitter phase. We have implemented both of these algorithms in C++.

In chapter 4 simulation results of our implementations are shown, validating some standard results from foregoing simulations in CDT. Furthermore, the autocorrelation times of both standard and *TBlocked* implementations are analyzed and compared. We found a marginal advantage of the *TBlocked* algorithm with respect to

the standard one, but the true relevance of the former is the observation that it is better suited to be implemented in a parallel machine, gaining in speed.

In chapter 5 the issue of present lack of observables characterizing geometric features in CDT is raised, and a new class of observables, based on the spectra of Laplacian-Beltrami matrices for graphs associated to spatial slices, is proposed and analyzed. These are obtained by using techniques from *spectral graph theory*, which are currently applied in a wide range of fields, scientific or not, like shape analysis in medical physics and 3D modeling, or the *PageRank* algorithm (the core of the Google Search engine, and the paramount reason for the Google's rise to success). The Laplace-Beltrami eigenspectrum and eigenvectors of a slice give qualitative and quantitative information about the geometry of the slice at various scales, and allows us to define a Fourier transform of functions defined on microscopic scales, like the scalar curvature on slices. In particular, we analyzed from different points of view, the geometries of slices, and obtained interesting results about their role within the full triangulation. Finally, we have exposed many proposal for further analyses and generalizations of the spectral methods, which might prove to be an important resource for the search of the continuum limit in the future.

# Chapter 2

## Overview of Causal Dynamical Triangulation

As already said in the previous chapter, Causal Dynamical Triangulations (CDT) is a background independent approach to Quantum Gravity, testing the asymptotic safety scenario with non-perturbative Markov Chain Monte Carlo (MCMC) methods [4].

The main steps of the CDT program are summarized as follows:

- Path-integral formulation of the Einstein-Hilbert theory.
- Discretization of the configuration space (Regge action).
- Analytic continuation from Lorentzian to Euclidean geometries (Wick rotation).
- Algorithmic implementation (Markov Chain updates).
- Phase diagram analysis.
- Identification of physical observables.
- Continuum limit.

In this chapter we will give an overview of these steps, with the exception of the algorithmic implementation, which will be discussed in the following chapter (3). Furthermore, we will introduce the theory of Renormalization Group in order to discuss the idea of asymptotic safety.

### 2.1 The path-integral formalism

As described in the previous chapter, for the CDT approach to properly describe a theory of Quantum Gravity in the asymptotic safety scenario, non-perturbative tools are necessary. Numerical methods employing Monte-Carlo techniques have been applied with success to investigate, in principle with arbitrary precision, non-perturbative features of statistical and quantum field systems (e.g., confinement in QCD).

For this reason, Monte-Carlo simulations are the natural settings for the CDT approach<sup>1</sup>. Monte-Carlo methods allow to consistently extract information from a discrete representation of a high dimensional configuration space. To perform numerical simulations of a quantum field theory, first of all we need to represent it by using the *path-integral formalism*, developed in 1948 by R. Feynman.

### Example: path-integral for a non-relativistic particle

Consider the evolution of a single non-relativistic particle in Quantum Mechanics. The *propagator* in space-time coordinates  $U(x_B, t_B; x_A, t_A)$ , is the probability amplitude for the particle to be observed at the space-time point  $A = (x_A, t_A)$  after it is “prepared” to be at the space-time point  $B = (x_B, t_B)$ . Formally it corresponds to the matrix element  $x_B, x_A$  of the unitary time-evolution operator  $\mathcal{U}(t_B, t_A)$ , that is:

$$U(x_B, t_B; x_A, t_A) = \langle x_B | \mathcal{U}(t_B, t_A) | x_A \rangle = \langle x_B | \mathcal{T} e^{-\frac{i}{\hbar} \int_{t_A}^{t_B} H(t) dt} | x_A \rangle, \quad (2.1)$$

where  $\mathcal{T}$  is the time-ordering symbol.

The dynamics of a quantum system is completely encoded in the propagator, since the time evolution of any initial wavefunction  $\psi_{t_0}(x) = \langle x | \psi_{t_0} \rangle$  is given by:

$$\psi_t(x) = \langle x | \psi_t \rangle = \langle x | \mathcal{U}(t, t_0) \int dx' | x' \rangle \langle x' | \psi_{t_0} \rangle = \int dx' U(x, t; x', t_0) \psi_{t_0}(x'), \quad (2.2)$$

where we inserted the completeness relation for the spatial basis  $\{|x\rangle\}$  ( $\int dx |x\rangle \langle x| = 1$ ).

For simplicity, let us consider a time independent Hamiltonian  $H(t) = H$  in the following. For any intermediate time  $t'$  ( $t_A < t' < t_B$ ) we can split the evolution operator as a product of two contributions, and insert between them the completeness relation for the spatial basis  $\{|x\rangle\}$ , obtaining the so called *Chapman-Kolmogorov equation*

$$U(x_B, t_B; x_A, t_A) = \langle x_B | e^{-\frac{i}{\hbar} H(t_B - t')} \left( \int_{-\infty}^{+\infty} dx' | x' \rangle \langle x' | \right) e^{-\frac{i}{\hbar} H(t' - t_A)} | x_A \rangle \quad (2.3)$$

$$= \int_{-\infty}^{+\infty} dx' U(x_B, t_B; x', t') U(x', t'; x_A, t_A). \quad (2.4)$$

This identity can be interpreted by saying that the probability amplitude for the particle to travel from  $(x_A, t_A)$  to  $(x_B, t_B)$  can be computed from the probability amplitudes to travel from  $(x_A, t_A)$  to an intermediate point  $(x', t')$  and then to  $(x_B, t_B)$ , by summing over all possible intermediate positions  $x'$ . One could think to reiterate this process an infinite number of times partitioning the interval  $[t_A, t_B]$  in infinitesimal steps.

At the end of the day, it can be shown that the propagator  $U(x_B, t_B; x_A, t_A)$  can be written as a sum over all possible paths  $X(t)$  from the event  $(x_A, t_A)$  to  $(x_B, t_B)$  in the form

$$U(x_B, t_B; x_A, t_A) = \int_{X(t_A)=x_A, X(t_B)=x_B} \mathcal{D}[X(t)] e^{\frac{i}{\hbar} S[X(t)]}, \quad (2.5)$$

---

<sup>1</sup>Analytical results of CDT in 2D have been obtained, but they seem to be unmanageable for the more interesting higher dimensions.

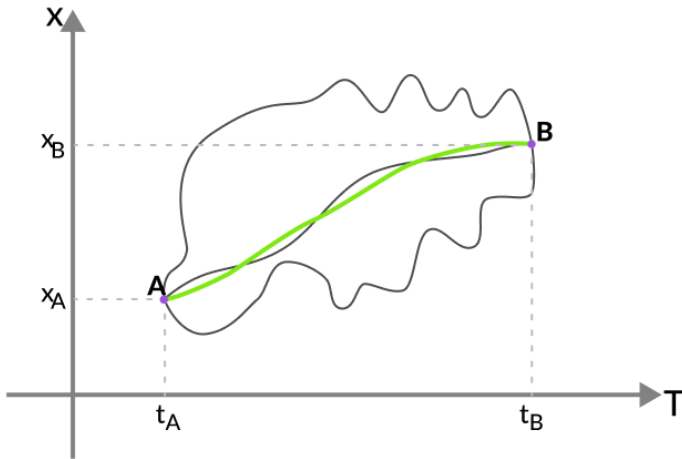


Figure 2.1: Examples of paths between two spacetime events A and B, where the green line represents the classical trajectory for a fictitious action. Only paths near the classical path will give a dominant contribution to the path-integral.

where  $S[X(t)]$  is the classical action functional of the system, evaluated on a trajectory  $X(t)$ .

To every path  $X(t)$  corresponds a phase  $e^{\frac{i}{\hbar}S[X(t)]}$ , and the sum of the phases from all possible paths (see figure 2.1) contributes to the probability amplitude. This can be interpreted by saying that different paths interfere with each others, and gives an intuitive explanation of why particles in QM possess wave properties (see the double slit experiment). In particular, the classical path  $X_{cl}(t)$  is by definition the one (assuming it unique) for which the classical action is stationary. More specifically, considering paths  $X(t) = X_{cl}(t) + \delta X(t)$ , differing from the classical one by an amount  $\delta X(t)$ , the action functional evaluated on them will be second order in the variation  $\delta X(t)$ , so that  $S[X(t)] = S[X_{cl}(t)] + \delta^2 S[X_{cl}(t)] + O(\|\delta X(t)\|^3)$ , where a metric in the space of paths has been defined<sup>2</sup>. This implies that paths for which  $\delta^2 S[X_{cl}(t)] \ll \hbar$  correspond almost to the same phase of the classical one  $S[X_{cl}(t)]$ , so, summing up their contributions results in constructive interference. On the converse, paths for which the action differ by much more than  $\hbar$  with respect to the action of the classical path destructively interfere with themselves because their contributions cancel out on average. The semi-classical limit of quantum mechanics can be interpreted in this framework as a saddle-point expansion of the path-integral for small values of  $\hbar$ , where trajectories far from the classical one are suppressed.

### 2.1.1 Path-integral for field theories and analytic continuation

The same path-integral formalism can be generalized to quantum field theories, where the degrees of freedom are the values of the fields  $\Phi$  at space-time coordinates

<sup>2</sup>In variational calculus it is customary to consider space of paths from  $t_A$  to  $t_B$  to be a Sobolev space and use the metric induced by the norm squared  $\|X(t)\|_{k,2}^2 \equiv \int_{t_A}^{t_B} \sum_{s=0}^k |X^{(s)}(t)|^2$ , where  $k$  is the maximum order of the derivatives which appear in the Lagrangian ( $k = 1$  for standard quantum mechanical problems).

$x^\mu$ . However here, instead of paths (i.e. trajectories evolving in time), the path-integral is a sum over field configurations on the whole spacetime; the space of configurations will be denoted by  $\mathcal{S}$ . Expressing all the fields involved with a single symbol  $\Phi$ , the path-integral evaluation of the (vacuum) expectation value for any observable  $\mathcal{O}$  in the configuration space  $\mathcal{S}$  is given by

$$\langle \mathcal{O} \rangle = \frac{1}{Z} \int_{\mathcal{S}} \mathcal{D}[\Phi] \mathcal{O}[\Phi] e^{\frac{i}{\hbar} S[\Phi]}, \quad \text{where} \quad Z = \int_{\mathcal{S}} \mathcal{D}[\Phi] e^{\frac{i}{\hbar} S[\Phi]}. \quad (2.6)$$

However, this form of the path-integral is still of no use to numerical implementations for two reasons. First of all, the path-integral is defined over a configuration space  $\mathcal{S}$  with uncountably infinite dimensions; this certainly cannot be managed by a computer, so we need to define a discretization of the dynamical variables into a finite-dimensional space, which represents with arbitrary precision the infinite-dimensional one. The representation used in CDT is based on the Regge formalism of triangulated manifolds, and will be discussed in the next section (sec. 2.2). Secondly, the term  $e^{\frac{i}{\hbar} S}$  is complex, and usually wildly oscillating through configurations, so integrating numerically is not a good idea.

Nevertheless, sometimes<sup>3</sup> it is possible to perform an analytic continuation of the action  $S(\alpha)$  with respect to some parameter  $\alpha \rightarrow \tilde{\alpha}$ , which makes the former phase term real and positive:  $S_E(\tilde{\alpha}) \equiv -iS(\tilde{\alpha}) \in \mathbb{R}$  such that  $e^{-S_E(\tilde{\alpha})/\hbar} > 0$ . This procedure is called *Wick rotation*, and the form used for CDT will be discussed more in details in section 2.3.

From a numerical point of view, the advantage of performing a Wick rotation is that now the path-integral measure  $\mathcal{D}[\Phi]e^{-S_E[\Phi]/\hbar}$  can be interpreted as a probability measure, whereas  $Z$  has the interpretation of a *partition function* of a statistical system in 4D<sup>4</sup>. Denoting by  $\mathcal{P}[\Phi] \equiv \frac{1}{Z}e^{-S_E[\Phi]}$  the probability density function of being in the configuration  $\Phi$ , after Wick rotation the vacuum amplitude (2.6) for any observable  $\mathcal{O}$  becomes

$$\langle \mathcal{O} \rangle = \int_{\mathcal{S}} \mathcal{D}[\Phi] \mathcal{O}[\Phi] \mathcal{P}[\Phi], \quad (2.7)$$

or, for discretized degrees of freedom

$$\langle \mathcal{O} \rangle = \sum_{\phi \in \mathcal{S}} \mathcal{O}(\phi) \mathcal{P}(\phi), \quad (2.8)$$

where  $\Phi$  is now a random variable that can takes values on  $\mathcal{S}$ ,  $\mathcal{P}(\phi)$  is the probability of the event  $\Phi = \phi$ , and  $\mathcal{O}(\cdot)$  is any function on  $\mathcal{S}$ .

In this form it is now possible to implement a numerical algorithm to estimate the average of any observable. Probably the most efficient class of algorithms is given by importance sampling Monte-Carlo methods, which will be discussed in chapter 3.

---

<sup>3</sup>There are many cases for which this is not possible, usually involving the presence of fermions. This phenomenon is called the *sign problem*, it is NP-hard, but many (more or less satisfying) solutions have been proposed over the years.

<sup>4</sup>When the time direction is compactified,  $Z$  can be interpreted also as a partition function for a thermodynamical system at finite temperature.

## 2.2 Discretization: the Regge action

For any observable  $\mathcal{O}$  depending on the manifold geometry the path-integral formulation of the Einstein-Hilbert can be summarized by the expressions

$$\langle \mathcal{O} \rangle = \frac{1}{Z} \int \mathcal{D}[g_{\mu\nu}] \mathcal{O}[g_{\mu\nu}] e^{\frac{i}{\hbar} S[g_{\mu\nu}]}, \quad Z = \int \mathcal{D}[g_{\mu\nu}] e^{\frac{i}{\hbar} S[g_{\mu\nu}]}, \quad (2.9)$$

where  $S$  is the usual Einstein-Hilbert action (1.1).

In order to perform numerical Monte-Carlo simulations of the Einstein-Hilbert theory we need to implement both discretization and Wick rotation procedures. Let us first consider discretization of the class of metrics modulo diffeomorphisms. In numerical simulations it is customary to discretize the degrees of freedom by localizing the information on the sites of a regular lattice, like a hypercubic grid. In Numerical Relativity, Cauchy methods are usually adopted, where spatial hypercubic grids containing the relevant degrees of freedom (spatial metric and extrinsic curvature) are evolved in physical time. However this does not seem to be appropriate for Quantum Gravity Monte-Carlo simulations, since the path-integral needs the evaluation of the action functional for full spacetimes. Furthermore, with a hypercubic grid the formalism cannot be manifestly background independent.

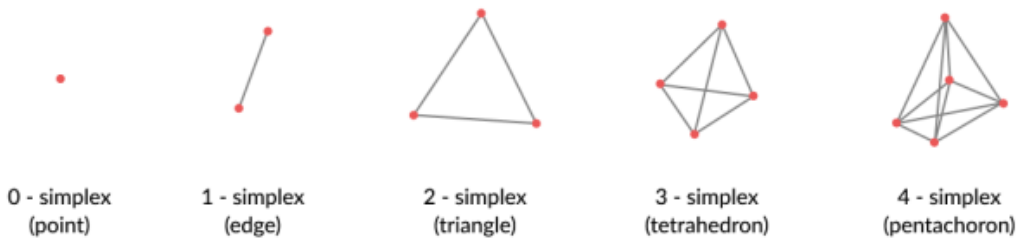


Figure 2.2: The types of  $k$ -simplices up to  $k = 4$

A more appealing discretization for Gravity comes from *Regge calculus*, a formalism invented by Tullio Regge in the sixties [5], which gives interesting insight about gravity and is actually useful in CDT. Each metric is associated to a manifold, and the idea of Regge calculus is to approximate this manifold by *simplices*, elementary flat building blocks of spacetime, glued together. This procedure is called *triangulation*, since triangles are the simplices corresponding to elementary surface areas. So, a discretized manifold, also called *simplicial* (piecewise flat) manifold, is represented in  $d$  dimensions by a hierarchy of  $k$ -simplices for  $k = 0, 1, \dots, d$ , where a 0-simplex is a vertex, a 1-simplex is an edge containing 2 vertices, a 2-simplex is a triangle containing 3 links and 3 vertices and so on (see figure 2.2). The way the simplices are glued contains information about the geometry of the simplicial manifold.

Let us consider for example a triangulated compact surface in Euclidean 2D like the one in figure 2.3. Compactness implies that each triangle is adjacent to exactly 3 other triangles, but vertices can be shared by an arbitrary number of triangles (at least 3). Physical points are localized in the interior of triangles, and information about the metric distance between points is represented by proximity relations between different triangles.

Information about curvature cannot be contained in triangles because, by definition,

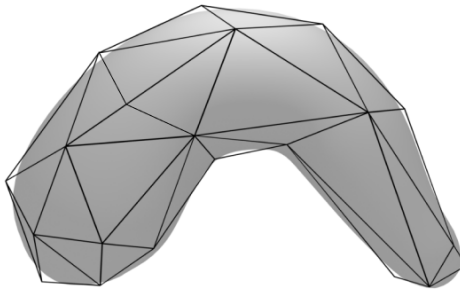


Figure 2.3: A 2-dimensional triangulation approximating a smooth surface.

their interior is flat. Regge showed that for a  $d$ -dimensional triangulation curvature information is completely encoded in the *deficit angle* around  $(d-2)$ -simplices, that corresponds to  $2\pi$  minus the angular amount by which a vector rotates when parallel transported around a given  $(d-2)$ -simplex. This can be shown easily in 2D by considering a vertex shared by a number  $n$  of equilateral triangles like in fig. 2.4. The angles of a single equilateral triangle measure  $\frac{\pi}{3}$  radians. The vertex A in figure contributes with zero curvature, because it is shared by exactly  $n = 6$  triangles, and then it is overall surrounded by  $6\frac{\pi}{3} = 2\pi$  radians, the same of a full angle, so the deficit angle is zero. Differently, the vertex B in figure is surrounded by  $n = 5$  triangles, so the deficit angle is  $2\pi - 5\frac{\pi}{3} = \frac{\pi}{3}$  and the curvature contribution of the vertex is positive, while it is negative the one of the vertex C in figure, since,  $n = 8$  equilateral triangles contributes to a negative deficit angle  $-2\frac{\pi}{3}$ . Adding up (scalar) curvature contributions from each vertex we obtain the total curvature of a triangulation.

Discretizing the configuration space is not enough; to sample triangulations  $\mathcal{T}$  with the correct probability distribution  $\mathcal{P}[\mathcal{T}] \propto e^{-S_E[\mathcal{T}]}$ , and before performing the analytical continuation to Euclidean space, we need a discretized form of the Einstein-Hilbert action as well. Let us rewrite the  $d$ -dimensional Einstein-Hilbert action in a convenient way

$$S[g_{\mu\nu}] = \underbrace{\frac{1}{16\pi G} \int d^d x \sqrt{-g} R}_{\text{total curvature}} - \underbrace{\frac{\Lambda}{8\pi G} \int d^d x \sqrt{-g}}_{\text{total volume}}. \quad (2.10)$$

It is clear that we need an expression for the total curvature and one for the total volume of any triangulation  $\mathcal{T}$  in  $d$  dimensions. As anticipated previously, Regge showed that the curvature is related to the deficit angle  $\varepsilon_{\sigma^{d-2}}$  of  $(d-2)$ -simplices  $\sigma^{d-2} \in \mathcal{T}$ . In particular, the contribution to the curvature of a simplex  $\sigma^{d-2}$  is exactly  $2\varepsilon_{\sigma^{d-2}} V_{\sigma^{d-2}}$ , where we denote by  $V_{\sigma^k}$  the  $k$ -volume of a given  $k$ -simplex  $\sigma^k$ . Adding up contributions from every  $(d-2)$ -simplex of the triangulation we obtain the discretized form of the total curvature

$$\int d^d x \sqrt{-g} R \longrightarrow \sum_{\sigma^{d-2} \in \mathcal{T}} 2\varepsilon_{\sigma^{d-2}} V_{\sigma^{d-2}}. \quad (2.11)$$

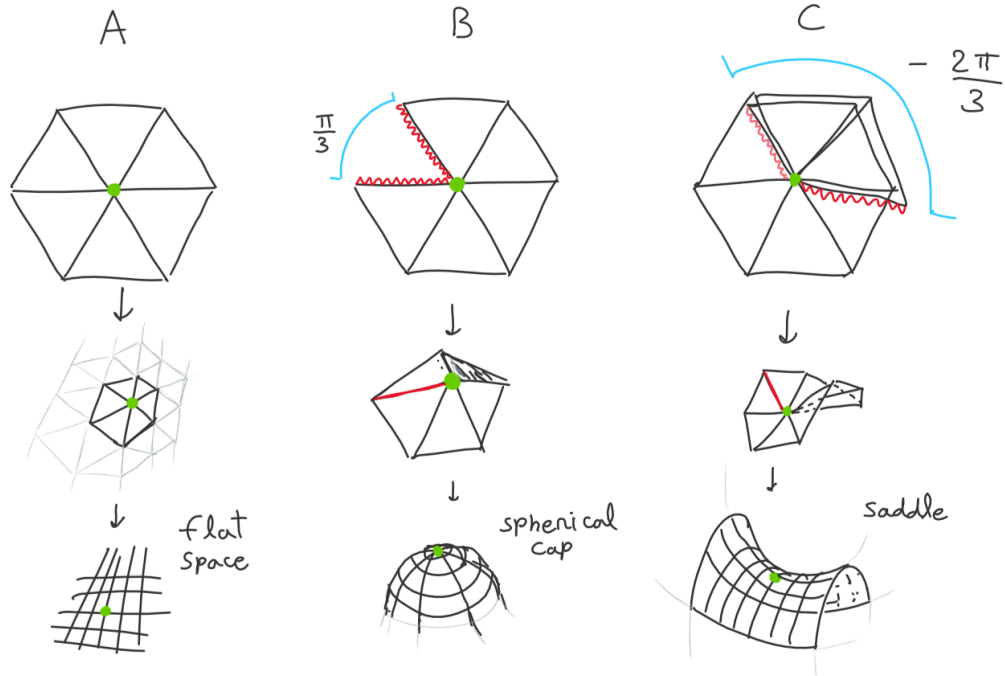


Figure 2.4: Example of the types of contributions to the curvature: zero (A), positive (B), negative (C).

The total (spacetime) volume is simply the sum of the volumes of all  $d$ -simplices

$$\int d^d x \sqrt{-g} \longrightarrow \sum_{\sigma^d \in \mathcal{T}} V_{\sigma^d}. \quad (2.12)$$

Using the last three equations we obtain the *Regge action*

$$S^{Regge}[\mathcal{T}] = \frac{1}{8\pi G} \left( \sum_{\sigma^{d-2} \in \mathcal{T}} \varepsilon_{\sigma^{d-2}} V_{\sigma^{d-2}} - \Lambda \sum_{\sigma^d \in \mathcal{T}} V_{\sigma^d} \right). \quad (2.13)$$

It is convenient to put eq. (2.13) in dimensionless form, by introducing the following dimensionless quantities

$$\mathcal{V}_{\sigma^k} \equiv \frac{V_{\sigma^k}}{a^k}, \quad \kappa = \frac{a^{d-2}}{16\pi G}, \quad \lambda = \frac{2\Lambda a^d}{16\pi G}, \quad (2.14)$$

where  $a$  is any length scale, and  $\kappa, \lambda$  are new parameters strictly related to the Newton constant and the cosmological constant respectively.

Finally, we obtain the nicer expression

$$S^{Regge}[\mathcal{T}] = \kappa \sum_{\sigma^{d-2} \in \mathcal{T}} \varepsilon_{\sigma^{d-2}} \mathcal{V}_{\sigma^{d-2}} - \lambda \sum_{\sigma^d \in \mathcal{T}} \mathcal{V}_{\sigma^d}. \quad (2.15)$$

Since CDT does not admit topology changes (as will be argued in the following section), the Gauss-Bonnet theorem in 2 dimensions implies that the curvature term in eq. (2.15) is constant<sup>5</sup>, so it does not contribute to the Monte-Carlo sampling of

<sup>5</sup>The total curvature of a 2-dimensional surface is equal to  $2\pi\chi$ , where  $\chi$  is the Euler characteristic.

2-dimensional triangulations.

For dimensions higher than two the curvature term is not anymore invariant with respect to homeomorphisms, so we should consider also the contributions to the action given by the deficit angles  $\varepsilon_{\sigma^{d-2}}$ , which for a generic triangulation are not easy to compute, since they involve the evaluation of dihedral angles and volumes for each  $(d-2)$ -simplex. One can overcome this difficulty resorting to the specific properties of triangulations adopted in CDT.

Indeed, as briefly explained in the introduction, CDT works with *foliated* triangulations<sup>6</sup> where vertices lies only on spatial slices. For this causal structure there are only two kinds of links (1-simplices): spacelike ones, connecting two vertices of the same slice, and timelike ones, connecting two vertices of consecutive slices. Then, a simplifying constraint can be imposed without loss of generality<sup>7</sup>: that each spacelike link has a fixed length-squared  $l_s^2 = a^2$ , while each timelike link has a fixed length-squared  $l_t^2 = -\alpha a^2$  ( $\alpha > 0$ ). With this constraint, only few types of

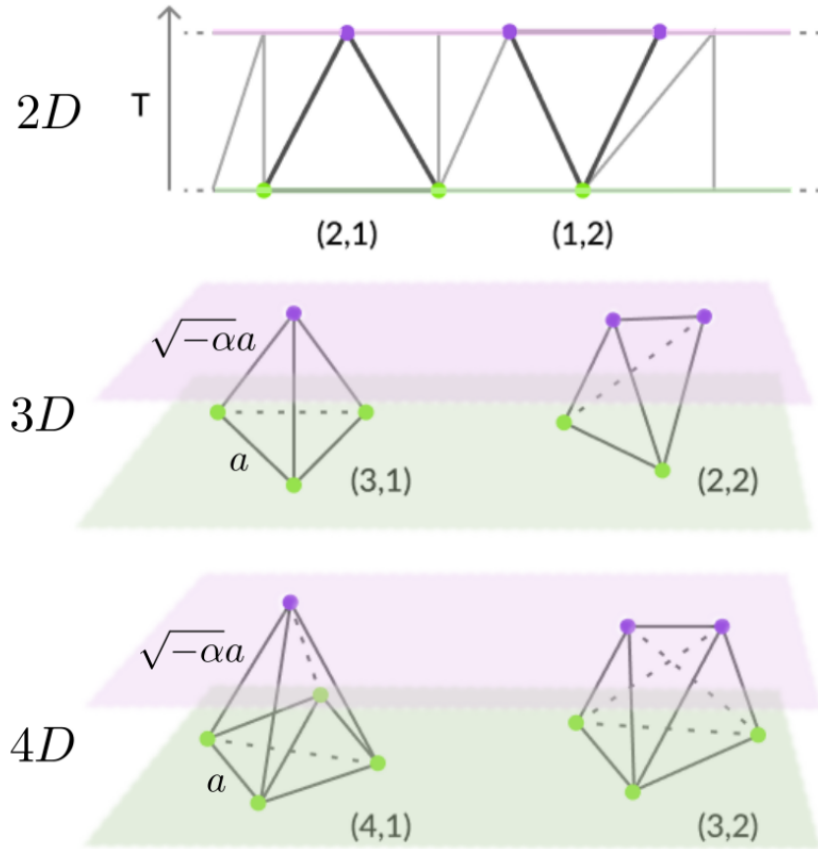


Figure 2.5: From the top to the bottom, all the types of maximal simplices in 2D, 3D and 4D, modulo time reversal.

$d$ -simplices are left, since all  $d$ -simplices with a given number  $m$  of vertices on a

<sup>6</sup>The condition of preferred foliation is surely convenient, but is not a strictly requirement of the CDT approach. Indeed, the article [10] shows that standard results of foliated CDT are retrieved also for a causal, but not foliated, triangulation.

<sup>7</sup>For example, approximating with arbitrary precision an Euclidean manifold using equilateral (and congruent) simplexes is always possible for a side length  $a$  small enough.

slice ( $1 \leq m \leq d - 1$ ) and  $d - m + 1$  vertices on a consecutive slice at later time label, form a class of congruent  $d$ -simplices that we will denote by  $(m, d - m + 1)$ . For example, in a (Lorentzian) 2-dimensional triangulation there will be only two types of triangles, related by time-reversal:  $(1, 2)$  and  $(2, 1)$ , where the three vertices are connected to themselves by one spacelike link and two timelike links. These are shown in figure 2.5, together with the different types of tetrahedra in 3D, and pentachorons in 4D. In this way, only a limited number of distinct dihedral angles and volumes are needed to write the Regge action for CDT triangulations. For a Lorentzian manifold angles and volumes are complex valued in general, but the action can be made real for a proper choice of the analytical continuation (some detail can be found in chapter 2 of [4]).

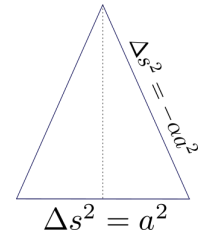
To be concrete, consider for example the 2D Regge action (eq. (2.15)). As argued above, in 2 dimensions the total curvature is a topological invariant  $2\pi\chi$ , so, assuming that all triangles have the same dimensionless (Lorentzian) volume  $\mathcal{V}_2$ , the action simply reads

$$S^{Regge,2D}[\mathcal{T}] = \kappa 2\pi\chi - \lambda \mathcal{V}_2 N_2[\mathcal{T}], \quad (2.16)$$

where  $N_2[\mathcal{T}]$  is the number of triangles in the triangulation  $\mathcal{T}$ .

The spacetime volume  $V_2$  of a  $(2, 1)$  is equal to its time-reversed counterpart  $(1, 2)$ , and can be computed simply by the “base times height divided by 2” formula, using the Lorentz-Pythagoras theorem for the height as shown in the figure on the right

$$V_2 = \frac{\sqrt{4\alpha + 1}}{4} a^2 \implies \mathcal{V}_2 = \frac{V_2}{a^2} = \frac{\sqrt{4\alpha + 1}}{4}, \quad (2.17)$$



so that the non-constant part of equation (2.16) becomes

$$S^{Regge,2D}[\mathcal{T}] = -\lambda \frac{\sqrt{4\alpha + 1}}{4} N_2[\mathcal{T}]. \quad (2.18)$$

Notice the  $\alpha$ -dependence of this action.

Similar, but more involved, geometric considerations can be applied to derive the expressions for volumes and dihedral angles of all the simplex types which appear in the  $d$ -dimensional Regge action. In this way, the sums in the expression for the Regge action (2.15) become a counting over all involved simplex types. Furthermore, since simplex types related by time-inversion have the same volume and dihedral angles, one can count them as the same type. For example in 2D there are two types of triangles,  $(1, 2)$  and  $(2, 1)$ , but their contribution to the action (2.16) is given by their volume  $\mathcal{V}_2$  multiplied by their number  $N_2[\mathcal{T}]$ , that shall depend on the triangulation  $\mathcal{T}$ .

For general dimensions the main idea is the same, but also  $k$ -simplices with  $k < d$  are involved. We will follow the conventions in [4], denoting the total number of simplices of given type in a  $d$  dimensional triangulation in the following way<sup>8</sup>:

<sup>8</sup>The numbers in table 2.2 are actually variables of the triangulations, but for simplicity we often omit the dependence.

$N_0$	number of vertices
$N_1$	number of links of any type
$N_1^{SL}$	number of spacelike links
$N_1^{TL}$	number of timelike links
$N_2$	number of triangles of any type
$N_2^{SL}$	number of spacelike triangles ( $d \geq 3$ only)
$N_2^{(2,1)}$	sum of the numbers of timelike triangles of types (2, 1) and (1, 2)
$N_3$	number of tetrahedra of any type
$N_3^{SL}$	number of spatial tetrahedra ( $d \geq 4$ only)
$N_3^{(3,1)}$	sum of the numbers of tetrahedra of types (3, 1) and (1, 3)
$N_3^{(2,2)}$	number of tetrahedra of type (2, 2)
$N_4$	number of pentachorons
$N_4^{(1,4)}$	sum of the numbers of pentachorons of types (1, 4) and (4, 1)
$N_4^{(2,3)}$	sum of the numbers of pentachorons of types (2, 3) and (3, 2)

In a triangulation however, these numbers are related by geometric identities, which depend also on the boundary conditions adopted. One identity comes from the topological invariance of the Euler characteristic<sup>9</sup>

$$\chi = \sum_{k=0}^d (-1)^k N_k, \quad (2.19)$$

where  $N_k$  is the total number of  $k$ -simplices. Other identities are given by a combination of local properties of simplicial manifolds and boundary conditions. For example in a compact 3-dimensional triangulation every spatial triangle is shared by exactly one tetrahedron of type (1, 3) and one of type (3, 1), so the relation  $N_2^{SL} = \frac{N_3^{(3,1)}}{2}$  must be true.

Ultimately, the general Regge action for a  $d$ -dimensional triangulation can be written in the following form

$$S^{Regge}[\mathcal{T}] = \sum_{\sigma} f_{\sigma} N_{\sigma}[\mathcal{T}], \quad (2.20)$$

where the sum is over all simplex types  $\{\sigma\}$ ,  $f_{\sigma}$  is an  $\alpha$ -dependent function containing information about volumes and dihedral angles for the  $\sigma$  simplex type, and  $N_{\sigma}[\mathcal{T}]$  is the number of simplices of type  $\sigma$  in the triangulation  $\mathcal{T}$  (one of the numbers in tab. 2.2).

After Wick rotation, this kind of action parametrization is the one actually used in CDT simulations, as we will show in the following section.

Another feature of CDT triangulations is that all slices must have the same topology, or equivalently, the topology of spatial slices cannot change in physical time. This is motivated by the observation that topology changes between different slices involve necessarily singular points where the light-cone structure degenerates, meaning that some geodesics are incomplete (cannot be extended to arbitrary times). But the gluing of  $d$ -simplices, having a flat interior and then an embedded Minkowskian light-cone, constrain the path of causal geodesics to be well defined everywhere.

---

<sup>9</sup>An interesting property of the Euler characteristic  $\chi$  of a 2-dimensional orientable surface is relation  $\chi = 2(1 - g)$ , where  $g$  is the *genus* of the surface, that is, informally speaking, the number of its holes.

The choice of the full spacetime topology, though, is arbitrary, but preserved during simulations. In principle, to evaluate the path-integral we should sum over all the contributions from distinct spacetime topologies, of the types  $[0, 1] \times \Sigma$  and  $S^1 \times \Sigma$ , where  $\Sigma$  is the fixed topology of  $(d - 1)$ -dimensional slices. However, actual CDT simulations are currently performed without topology transitions, since the updates of the triangulations are local homeomorphisms. the topology of slices  $\Sigma$  choices actually investigated are  $\Sigma \cong S^3$  (three-sphere) and  $\Sigma \cong T^3 \equiv S^1 \times S^1 \times S^1$  (three-torus).

In this thesis we will focus on triangulations with time-periodic boundary conditions and slices with spherical topology, that is  $S^1 \times S^3$ .

## 2.3 Wick rotation

In quantum field theory on Minkowski space, writing the invariant spacetime interval as  $ds^2 = -\alpha(dt)^2 + dx^2 + dy^2 + dz^2$  ( $\alpha = 1$ ), the standard Wick rotation of the action term  $iS(t) \mapsto -S_E(\tau)$  is implemented by the analytic continuation  $\alpha \mapsto \tilde{\alpha} = -\alpha$ , where  $\tau = \sqrt{\tilde{\alpha}}t = \sqrt{-\alpha}t^{10}$ .

A similar procedure can be applied to the Regge action. As mentioned in the previous section, spacelike and timelike links of a CDT triangulation have a length-squared  $l_s^2 = a^2$  and  $l_t^2 = -\alpha a^2$  ( $\alpha > 0$ ) respectively. The parameter  $\alpha$  is the one used to perform the analytical continuation  $\alpha \mapsto \tilde{\alpha} = -\alpha$  of the Lorentzian triangulation to a corresponding Euclidean one. The resulting Euclidean length-squared of former timelike links is now  $\tilde{\alpha}a^2$  where the definite positivity of the Euclidean metric enforces  $\tilde{\alpha} > 0$ .

For example, using the 2-dimensional Regge action ((2.18)), analytical continuation  $\alpha \rightarrow \tilde{\alpha}$  of the exponent of the phase term  $e^{iS}$  gives us

$$iS^{Regge,2D}(\alpha) \rightarrow iS^{Regge,2D}(-\tilde{\alpha}) = -\lambda \frac{\sqrt{4\tilde{\alpha}-1}}{4} N_2 = -S_E^{Regge,2D}(\tilde{\alpha}). \quad (2.21)$$

By a redefinition of the free parameter  $\lambda \leftarrow \lambda \frac{\sqrt{4\tilde{\alpha}-1}}{4}$  we obtain a simple form of the 2-dimensional, Wick rotated, Regge action

$$S_E^{Regge,2D} = \lambda N_2, \quad (2.22)$$

where in the last two equations the  $\mathcal{T}$  dependence is understood.

This means that a simple counting of triangles is sufficient to weight 2-dimensional triangulations. The resulting probability distributions

$$\mathcal{P}[\mathcal{T}] \propto e^{-\lambda N_2[\mathcal{T}]} \quad (2.23)$$

seems trivial, but in fact the complexity is hidden in the entropy encoded in the counting of all possible gluings between simplexes of the simplicial manifold. By inspecting expression (2.23) one immediately notices that, for  $\lambda = 0$ , triangulations with an arbitrary number of triangles are not suppressed (resulting in an “explosion” of the lattice during simulations in 2D). Exact analytical results show that there is

---

<sup>10</sup>Actually, the square root has two solutions, e.g. taking  $\alpha = 1$  then  $\tau = \sqrt{-1}t = \pm it$ ; the sign choice is a matter of convention, but in quantum field theory it must be consistent with the pole prescription ( $\epsilon$  term) used in the Feynman propagator.

a critical value  $\lambda_c = -\ln(2)$  such that, for  $\lambda \leq \lambda_c$  the average spacetime volume  $\langle N_2 \rangle$  is infinite, while for  $\lambda > \lambda_c$  it is finite.

In general,  $\tilde{\alpha}$  cannot take any positive value, since simplicial manifold constraints must be taken into account; e.g. in 2D the edge lengths  $l_s$  and  $l_t$  of the new Euclidean triangles must satisfy triangle inequalities, and can easily be shown that this implies  $\tilde{\alpha} > \frac{1}{4}$  (evident from eq. (2.21)). In 4D, similar considerations can be done, and the constraint reads

$$\tilde{\alpha} > \sqrt{\frac{7}{12}}. \quad (2.24)$$

Having computed dihedral angles and volumes of Lorentzian simplices as functions of  $\alpha$ , the new wick rotated quantities will be functions of  $\tilde{\alpha}$ , and therefore also the new Euclidean action  $S_E$ . After Wick rotation  $\alpha \mapsto \tilde{\alpha}$ , and using the identities between simplex numbers, eq. (2.20) becomes (for details read [11])

$$S_E^{(3D)}[\mathcal{T}] = -k_1 N_1[\mathcal{T}] + k_3 N_3[\mathcal{T}] + (\text{$\tilde{\alpha}$-dependent terms, zero if $\tilde{\alpha} = 1$}) \quad (2.25)$$

$$S_E^{(4D)}[\mathcal{T}] = -k_0 N_0[\mathcal{T}] + k_4 N_4[\mathcal{T}] + (\text{$\tilde{\alpha}$-dependent terms, zero if $\tilde{\alpha} = 1$}) \quad (2.26)$$

In particular, for the 4-dimensional case with spherical slice topology and time-periodic conditions  $S^1 \times S^3$ , the action can be conventionally parametrized as follows

$$S_E = -k_0 N_0 + k_4 N_4 + \Delta(N_4 + N_4^{(4,1)} - 6N_0), \quad (2.27)$$

where we the dependence on  $\mathcal{T}$  is understood, and we introduced the new parameter  $\Delta$ , which vanishes for  $\tilde{\alpha} = 1$  and therefore encodes the amount of asymmetry in the length of timelike and spacelike links. Having the freedom to choose any value of  $\tilde{\alpha}$ , at least in a certain range,  $\Delta$  should enter the action as a new free parameter for simulations representing different, but equivalently possible, analytic continuations<sup>11</sup>

Using the action parametrization (2.27) we get a parametrized family of probability distributions in the space of triangulations  $\mathcal{P}_{(k_0, k_4, \Delta)}[\mathcal{T}] \propto e^{-S_E(k_0, k_4, \Delta)[\mathcal{T}]}$ . Here the action parameters  $k_0$  and  $k_4$  are related to the Newton  $G$  and cosmological  $\Lambda$  constants respectively. Since  $N_4$  is the total number of pentachorons, quantifying the spacetime volume of the triangulation, the action (2.27) tells us that the more larger  $k_4$  is, the less probable are configurations with large volumes. In particular, for fixed  $k_0$  and  $\Delta$ , it is observed a critical  $k_4 = k_{4c}(k_0, \Delta)$  under which the volume diverges. So, the  $k_4$  parameters controls the average volume  $\langle N_4 \rangle$  of the sampled configurations.

### 2.3.1 Volume fixing

Unlike typical QFT simulations, in CDT simulations the size of the lattice can change during the simulation, since the same lattice structure encodes the gravitational degrees of freedom. However, it is customary to sample configurations choosing an approximately fixed volume  $N_4 = V$  for two reason: on one hand we want prevent the occurrence of arbitrarily large volume fluctuations, which could eventually exceed our memory resources; on the other hand it makes possible to implement a *finite size scaling* analysis, where the behaviour of observables for increasing volumes is studied and extrapolated, therefore giving useful information

---

<sup>11</sup>Unlike the quantum field theory case, where typically one fixes  $\alpha = 1$  at the onset.

about the critical behaviour of the system near a transition. The standard procedure used in DT and CDT is to *fine-tune* the parameter  $k_4$  in order to make the configurations fluctuate around the target volume  $V$ , enforcing  $\langle N_4 \rangle \simeq V$ , and then taking measures only when  $N_4 = V$ . For this reason, it is useful to impose a weak constraint on the configuration space by introducing a “volume fixing” factor in the probability function, like the Gaussian mollifier<sup>12</sup>

$$e^{-\Delta_\epsilon S} = e^{-\epsilon(N_4 - V)^2}, \quad (2.28)$$

where  $\epsilon$  is a positive and sufficiently small constant. This term makes more difficult to reach configurations with volumes  $N_4$  arbitrarily larger or smaller than the target volume  $V$ ; indeed, configurations with  $N_4 \gg V + 1/\sqrt{\epsilon}$  or  $N_4 \ll V - 1/\sqrt{\epsilon}$  are suppressed. Alternatively, one can choose to fix the average of the spatial volume  $N_3^{ST} = N_4^{(4,1)}/2$ . The form of the equations and the  $k_4$  fine-tuning are unchanged; for example, spatial volume fixing  $\langle N_4^{(4,1)} \rangle = V$  can be implemented by adding an action term

$$\Delta_\epsilon S = \epsilon(N_{41} - V)^2. \quad (2.29)$$

Since fixing for example the average spacetime volume  $\langle N_4 \rangle = V$  corresponds to *fine-tuning*<sup>13</sup> the  $k_4$  parameter to a specific value  $k_4(V; k_0, \Delta)$ , the latter is no more a free parameter of the Lagrangian<sup>14</sup>. By this procedure, the parameters which can be controlled are  $k_0$ ,  $\Delta$ , and the spacetime (or spatial) volume  $V$  at which measures of observables are taken corresponds to the average size of the lattice during the simulation.

## 2.4 Renormalization Group

In this section we will show how is it conceptually possible to non-perturbatively renormalize a theory within the framework of the Wilsonian Renormalization Group. The topics covered here do not restrict merely to CDT, but are needed to introduce more in detail the idea of asymptotic safety. A good quantum field theory, mathematically described by an action functional of the fields, should be able to describe physical systems at all scales *preserving its form*.

From the point of view of naive perturbation theory in quantum field theories, this simply means that no additional counterterms are needed to cancel the divergences that come out from the infinitely short scales (or high momenta), and the finite number of terms that makes up the Lagrangian are sufficient; this makes the theory predictive, because only a finite number of parameters needs to be fixed by experiments. The idea of a form-preserving theory with respect to a change of scale is systematized by the more general framework of the Wilsonian “Renormalization Group” (RG) [12].

In RG theory we need to define a so-called “coarse graining” procedure, that is a transformation of the dynamical variables implementing the idea of merging the

<sup>12</sup>Other spacetime volume fixing choices can be used, for example  $\Delta_\epsilon S = \epsilon|N_4 - V|$ .

<sup>13</sup>The fine-tuning of  $k_4$  can be implemented, for example, by estimating the average  $\bar{N}_4$  and standard deviation  $\Delta N_4$  of the sampled volumes for a given  $k_4^{old}$ , and performing iteratively a gradient descent  $k_4^{new} = k_4^{old} + \nu \frac{(\bar{N}_4 - V)}{\Delta N_4}$  (with a small  $\nu > 0$ ) to make it as close as possible to the target volume  $V$ . This must be done during the thermalization phase of the simulation.

<sup>14</sup>This change of variables can be interpreted as a Legendre transformation.

information about spatially nearby regions into fewer degrees of freedom<sup>15</sup>. To be more concrete, consider for example a real scalar field defined on a square lattice. The conceptually simplest implementation of coarse graining for this system is called “blocking”, and consists to regroup nearby sites into square blocks, and compute averages of the field values within them. The resulting system is a new scalar field, where the block’s positions take on the role of new sites, and the averages computed within blocks are the new field’s values.

In practice, other forms of coarse graining are adopted for field theories (like smoothly cut-off high-momentum Fourier components of the fields), and also inner degrees of freedom need to be suitably merged and rescaled by some renormalization factor, but the main idea of representing the system using a lower spatial resolution holds. After a coarse graining procedure, the spatial degrees of freedom of the dynamical variables will be different from the ones before, so, for the sake of comparing different scales, in addition to the concept of coarse graining, we need to define a “scale transformation” (or rescaling), that in layman terms is like changing the magnifying power of an imaginary microscope through which one observes a physical system.

A RG transformation  $\mathcal{R}_b$  is the consecutive application of a coarse graining and a rescaling by the same length factors  $b$ , so that it maps the degrees of freedom to themselves. However, for a statistical system for example, configurations with a certain probability distribution functions (p.d.f.) will be mapped to new configurations in the same probability space but with a different probability distribution function. If the space of all p.d.f. considered is parametrized by a vector  $\vec{g}$ , for example, the RG transform applied to configurations generated by a p.d.f., corresponding certain values of the parameters  $\vec{g}_0$ , maps them to new configurations that would seem to be generated by another p.d.f., corresponding to new parameters  $\vec{g}_1$ . Fixing the symmetries for the systems under study, we consider the most general class of theories described by a (possibly infinite) set of parameters  $\{g_i\} \equiv \vec{g} \in \mathcal{G}$ , that is, we identify a theory with a point  $\vec{g}$  in a parameter space  $\mathcal{G}$ . Hopefully, the RG transformation does not break the relevant symmetries, so it has to be an automorphism of the space of theories<sup>16</sup>  $\mathcal{G}$ , that is, starting from a theory/point  $\vec{g}_0 \in \mathcal{G}$  and applying a RG transformation  $\mathcal{R}_b$ , we obtain a new theory/point  $\vec{g}(b) = \mathcal{R}_b \vec{g}_0$  in the same space; indeed, by imposing that the physics observed in the RG transformed system has to be the same of the original one, we need to “tune” accordingly the parameters. The factor  $b$  can be taken infinitesimal and the initial theory/point can be any element of  $\mathcal{G}$ , so, the RG transformation defines a “Renormalization Group flow” on the whole parameter space  $\mathcal{G}$ . This has an interesting interpretation, since starting from a theory/point we can follow how it evolves in “RG time”, that is its RG “trajectory”, theories/points lying on these trajectories are similar at different scales.

Since the RG transformation consists of successive applications of coarse graining and “de-zooming” (rescaling), starting from a theory/point  $g_0 \in \mathcal{G}$  we can follow the flux direction and study how the physics changes going toward larger scales. This is useful for studying condensed matter systems, where most of the microscopic details

---

<sup>15</sup>There are actually many analogies between RG and *lossy* data compression techniques used in computer science.

<sup>16</sup>The term *theory* here could not be restricted solely to a Lagrangian theory, but to any parametrizable description of a physical system. For example, simple percolation processes can be described by the parameter  $p$ , the occupation probability, and a set of *rules*.

of atomic lattices are uninteresting to characterize macroscopic behavior.

We could also follow the inverse flux direction, that corresponds to going toward shorter scales/higher energies, and this is actually useful to characterize the behavior of quantum field theories, so it is of interest for the study of Quantum Gravity theories that need to be valid at arbitrarily short scales.

Theories/points in  $\mathcal{G}$  that do not evolve with respect to the RG transformation, so that their RG trajectory is static, are called “fixed points”. Fixed points are interpreted as scale invariant theories, and this observation displays a conceptual connection with the divergence of correlation lengths, since, by the same definition of scale invariant theory, there cannot be a ‘typical’ scale, so the only two cases left are  $\xi = 0, \infty$ .

In general, for a given space of theories/parameters  $\mathcal{G}$  we could have many fixed points. The “Gaussian fixed point”, for example, corresponds to a non-interacting (also called trivial) theory, that is, all parameters associated to interaction terms (couplings) in the Lagrangian are zero, then fields are free and the Lagrangian is quadratic in them, so the path-integral is exactly solvable because it is Gaussian. Furthermore, we can characterize the behavior of theories near a fixed point by analyzing the directions (inward or outward) of RG flow lines in the tangent plane of  $\mathcal{G}$ . As said before, since the RG flow is a transformation toward larger scales, RG flux lines converging into a fixed point span a region of theories/points which large-scale limit is the theory associated to the fixed point itself. So, the inward directions identify a region of theories around the fixed point that behave similarly on large scales. This explains why many seemingly unrelated physical systems possess similar (or “universal”) critical behaviors. This region is usually called “critical surface” of infrared (IR) attraction for the IR fixed point. The term attraction is motivated by the observation that parameters of theories in a critical surface are attracted towards specific values in their RG flow toward the fixed point (violet line in figure 2.6 for the point  $\mathbf{N}$ ). Theories/points near but off this surface would move away instead of being attracted.

Usually in quantum field theory we are interested in the short-scale/ultraviolet behavior of theories, so in this context it is more useful to follow the inverse RG flow. The directions around a fixed point for which RG flow is outward directed span a so-called critical surface of ultraviolet (UV) attraction, because the parameters that characterize the critical surface seem to be attracted towards the fixed point in going to shorter and shorter scales (green line in figure 2.6 for the point  $\mathbf{N}$ ). The fixed point is here the short-scale (UV) limit for theories in its critical surface, and for this reason it is called an UV fixed point. Since theories in a critical surface are equivalent in the UV limit, and differ only by a certain number of parameters, the dimensionality of the critical surface for an UV fixed point tells us how many parameters are “irrelevant” (or marginal) to characterize the universal behavior of theories near a fixed point.

The remaining parameters are called “relevant”, and must be fine-tuned to reach the critical surface, because theories/points not lying in the critical surface of an UV fixed point move away from the fixed point if one goes to shorter and shorter scales<sup>17</sup>. In this setting, if a theory belongs to the UV critical surface of a fixed point and can be described by a finite number of relevant parameters (i.e. the co-

---

<sup>17</sup>Since we are following the inverse RG flow, the definitions of what is relevant and what is irrelevant are exchanged with respect to the case of direct RG flow.

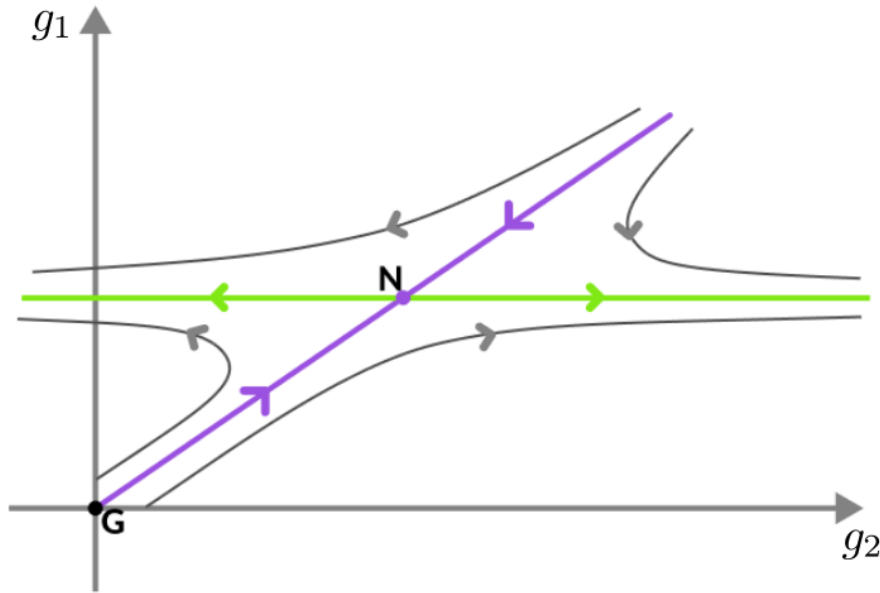


Figure 2.6: Example of RG flux diagram in a theory space with 2 parameters. The points **G** and **N** are respectively the Gaussian fixed point ( $\vec{g} = 0$ ) and a non-trivial fixed point.

dimension of the critical surface is finite), we say that the theory is renormalizable and is capable to describe physics at short distances. However, that the physics described by a theory in the critical surface of a fixed point is the one we are seeking from the onset must be verified a posteriori by comparison with experiments. The physics we want to model could be described by another fixed point, or worse, other symmetries and mechanisms we are not considering could intervene at short scales. The strength of the RG framework is that it automatically identifies the theories most consistent with given symmetries and dimensions, corresponding to the fixed points. In the best case scenario we find the correct description at short scales of the physics we are interested, otherwise we find a consistent but probably pointless theories. Despite theoretical efforts, the last word is left to experiments.

In conclusion, the procedure usually adopted to model and analyze a class of quantum field theories within the RG framework can be summarized by the following recipe:

- Choose dynamical variables and symmetries for the Lagrangian.
- Build the most general Lagrangian invariant to the symmetries chosen in the previous step, and parametrize its terms by a suitable set of *coupling coefficients* (they are allowed to be infinite).
- Define the RG transformation: *coarse graining* and *rescaling* of the dynamical variables keeping physics (observables) constant.
- Follow the flux of *running* couplings.
- Identify UV fixed points of the flux and their critical surfaces.
- Select, if it exists, the UV fixed point representing at best experimental data.

### 2.4.1 Asymptotic safety

Now we should possess all the tools to interpret the previous results of naive perturbation theory from the RG point of view: expanding quantities as formal series of “small” couplings is equivalent to considering theories in the UV critical surface of the Gaussian fixed point, since there the couplings would be attracted toward  $\vec{g} = 0$  in going to smaller and smaller scales. For example, an asymptotic free theory like QCD is one for which running couplings tends to zero for increasing energies ( $E \gg \Lambda_{QCD} \simeq 200$  Mev), so the Gaussian fixed point is UV (recall ‘high energy’  $\equiv$  ‘short scales’), and the theory is perturbatively renormalizable as a formal power series in the couplings. However, if the set of theories we are considering has a Gaussian fixed point that is IR instead of being UV, quantities measured at short scales could diverge, making the theory perturbatively non-renormalizable; this, likely, is the case of the Einstein-Hilbert Lagrangian.

But in the previous section we have shown that a class of parametrized Lagrangians could possess many RG fixed points in the space of theories  $\mathcal{G}$ . From these observations a possible solution to the quantum gravity problems seems to come immediately.

The conjecture of “Asymptotic safety”, advanced by S. Weinberg in 1976, states the existence of a non-trivial UV fixed point, with a critical surface of finite co-dimension, around which it is possible to renormalize non-perturbatively the quantum Einstein-Hilbert theory of gravity. Actually, the idea of Asymptotic safety has been applied also to other perturbatively non-renormalizable theories. For an asymptotic safe theory, the short-scale/high-energy limit of the theory is not attained for vanishing couplings (i.e. in the Gaussian fixed point), but for finite non-zero values of the couplings. In particular, the previously shown result of perturbative non-renormalizability of the Einstein-Hilbert action is, in the asymptotic safety scenario, arrogated to the IR character of the Gaussian fixed point, while the non-trivial UV fixed point can be used to generalize perturbative renormalization.

Strong evidences of the occurrence of the asymptotic safety scenario in Quantum Gravity comes from Functional Renormalization Group techniques, where a truncation of the space of the most general Lagrangians invariant with respect to diffeomorphisms is taken as parameter space  $\mathcal{G}$  for the RG flow [13]. In this framework, an UV-attractive non-trivial fixed point seems to arise using the Einstein-Hilbert truncation, where only  $G$  and  $\Lambda$  are taken as parameters and the parametrized action is given by eq. (1.1) (see figure 2.7). Further extensions of the functional space with terms polynomial in the Ricci scalar ( $f(R)$ -truncations) and in the Weyl curvature tensor, do not seem to affect very much the presence and stability of this fixed point, projected on the Einstein-Hilbert theory subspace. However, although useful to detect the possibility of a continuous quantum gravity, it is actually hard to obtain results about physically interesting observables by using only Functional Renormalization Group techniques.

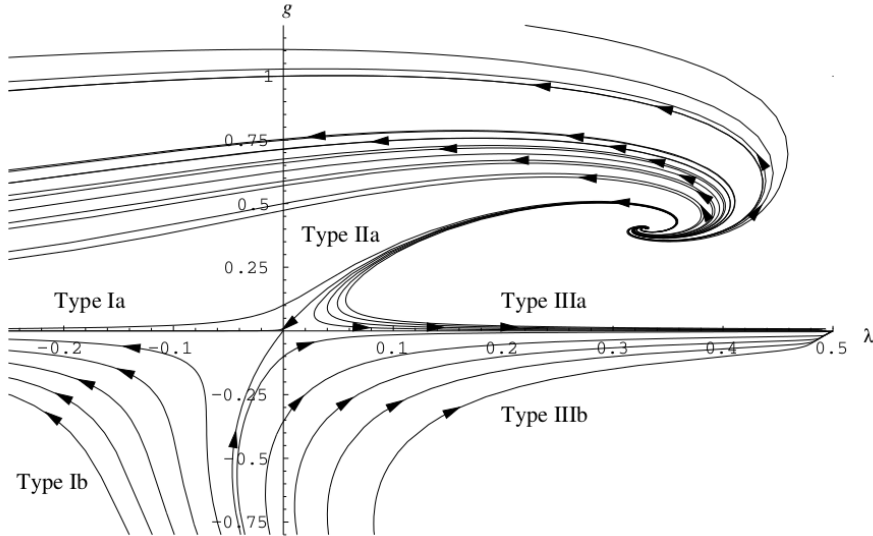


Figure 2.7: Plot of the functional RG flow in the Einstein-Hilbert truncation. The dimensionless parameters  $g$  and  $\lambda$  are related to the Newton and cosmological constants [13]. Taken from [13]

## 2.5 Current state of the research in CDT

Causal dynamical triangulation is a relatively recent approach and, like other approaches, still does not offer a conclusive answer to the QG problem. However, many interesting results have already been obtained, and the hopes toward the realization of an asymptotic safety scenario become increasingly serious. In particular, the presence of two continuous order transition lines in the phase diagram bodes well for a continuum limit, and research in this direction is currently being undertaken. We want to stress a problem that must not be underestimated though, that is the paucity of observables definitions. This problem is somewhat common to other QG approaches also, but the specific causal structure of triangulations in CDT probably makes it more arduous.

In the following subsections we will describe the current structure of the phase diagram, and discuss some open problems in CDT.

### 2.5.1 Overview of the phase diagram

Studying the behaviour of simulations at the same volume  $V$  but with different free parameters  $k_0$  and  $\Delta$  allows us to build a phase diagram with coordinates  $(k_0, \Delta)$  like the one qualitatively sketched in figure 2.8.

Three phases are distinguished by large scale observables like  $N_{3s}(t)$ , the spatial volume as a function of the slice time: *A phase* is characterized by an apparently random distribution of spatial volume among all slices like many small short-living universes, the spatial volume in *B phase* is completely localized at a single time slice like a single big short-living universe, while the single universe in *C phase* has volume distributed in a finite temporal extension, so it has some hopes to represent the physical universe. Recently it has been discovered that the *C phase* can be further divided into two phases, *C<sub>ds</sub>* called *de Sitter* phase and *C<sub>b</sub>* called *bifurcation*

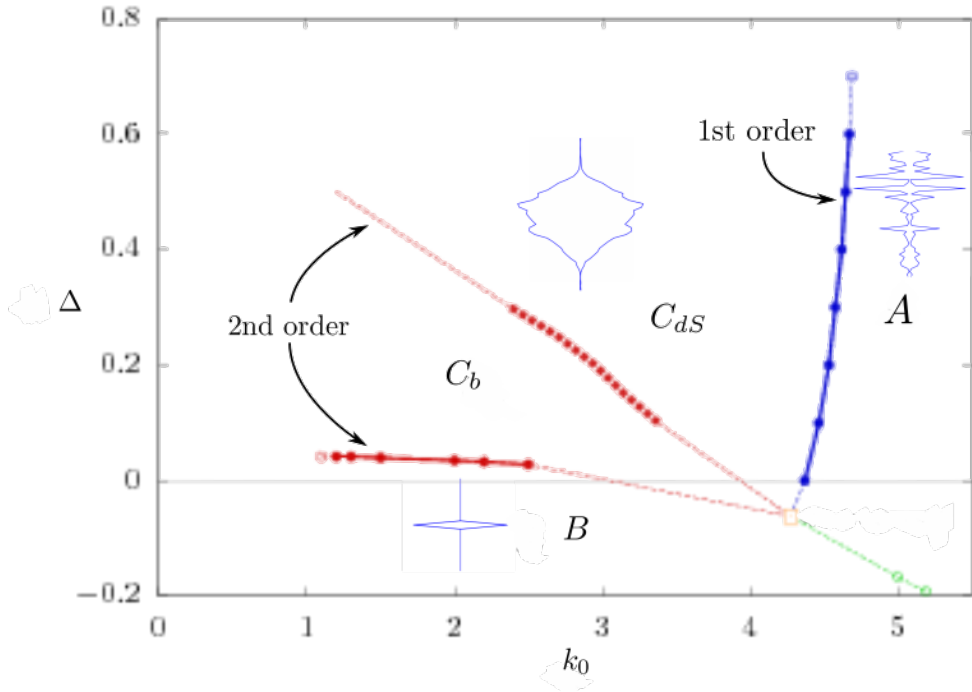


Figure 2.8: Phase diagram of CDT where the distribution of spatial volume along the slices, the so-called *profile*, is shown for each phase ( $C_{dS}$  and  $C_b$  have similar profiles, but differ by microscopic features). The (Wick-rotated) time for the profiles is in the vertical direction. Picture of the phase diagram taken from [9]

*phase*, discriminated, at the microscopic scale, by the presence of isolated vertices with high coordination (number of pentachorons sharing them) at alternated slices. As already mentioned in the previous chapter (1), special observables signalling a radical change of the properties of configurations through the phase diagram are called *order parameters*. These observables are related to specific symmetries of the configurations, and usually are interpreted as quantifiers of how much a symmetry is broken.

Let us consider for example the familiar 2-dimensional Ising model ferromagnetism, where the absolute value of the magnetization, the sum of all magnetic dipoles, act as an order parameter. The probability measure is invariant with respect to the group  $\mathbb{Z}_2$ , that acts on the configuration space as a flip of all the spins. For temperatures below a certain value  $T_c$  is observed an ordered phase where typical configurations have the majority of all spins aligned up and few down or viceversa, resulting in a long-range spin correlation and high value of the magnetization. In the thermodynamic limit this implies that it is unlikely that the system spontaneously flips all spins, so the  $\mathbb{Z}_2$  symmetry is broken, and the system is said to be *ordered*. For temperatures above the critical one the  $\mathbb{Z}_2$  symmetry is restored, spins are short-range correlated, and the average magnetization is almost zero. This corresponds to a *disordered* phase, since the system typically explores more configurations than in the ordered phase, resulting in a high entropy.

However, it is not easy to identify symmetries and associated order parameters for the Regge action used in CDT, since the actual dynamical variables, encoding geometric information of the triangulation, do not appear in the action except in the

form of a global counting of simplices. The actual order parameters used to characterize the phase diagram of 4-dimensional simulations in CDT will be described in sec. 4.1. Here we anticipate only that while the transition line between the  $A$  and  $C_{dS}$  phases is first-order, both the  $C_b|B$  and  $C_{dS}|C_b$  transition lines appears to be of continuous order, so they could actually contain one or more critical points with diverging correlation lengths near which it should be possible to perform a continuum limit, therefore validating the asymptotic safety scenario. It is not an easy task, however, since it is not easy to define meaningful correlation lengths. This is connected to the more general difficulty of defining observables in pure-gauge gravity, discussed in the next subsection.

### 2.5.2 Hunting for observables in Quantum Gravity

One of the main problems in quantum gravity is the identification and choice of meaningful observables, especially in the absence of matter fields (pure-gauge).

The following is a list of observables actually employed in pure-gauge CDT, many of which will be defined in chap. 4:

- Spatial volume per slice:  $N_{3s}(t)$ .  
(the number of spatial tetrahedra at the slice labeled by  $t$ )
- Order parameters for transitions (defined in subsec. 4.1.2):
  - $\text{conj}(k_0)$  for the  $A|C_{dS}$  transition;
  - $\text{conj}(\Delta)$  for the  $B|C_b$  transition;
  - $\text{OP}_2$  for the  $C_b|C_{dS}$  transition (discussed, but not analyzed here).
- Fractal dimensions for spacetime triangulations and spatial slices:
  - spectral (discussed in subsec. 4.2.2)
  - Hausdorff (not discussed here; check [4])

However, in our opinion, these observables give only a partial and unsatisfactory picture of the physics of triangulations. In particular, no observable characterizing the internal structure of triangulations at large scales is found in literature.

In chapter 5 we will propose a new class of observables to overcome this lack. Furthermore, somewhat related to the hunt for observables, is the search for an explicit RG transformation of triangulations. The RG analysis is a valuable tool extensively used in the analysis of typical lattice simulations in order to obtain accurate estimates of the critical behaviour and identify the fixed points of the theory. Notice however, that the blocking procedure discussed in sec. 2.4 is made possible by the specific structure of the hypercubic lattice, but unfortunately, due to the structure of causal triangulations, no obvious definition of coarse-graining for CDT configurations exists yet.

### 2.5.3 Continuum limit and RG transformation in CDT

The definition of a proper set of observables, not only provide a way to describe physical effects, but is actually functional to the quest for the continuum limit. Indeed, the ultimate aim of CDT, as for any QG approach, is to show that the results consistently describe quantum gravitational physics at ultraviolet scales. As we argued previously, in numerical simulations this is possible only by performing a continuum limit in the form of a continuous critical point with diverging correlation lengths in the phase space. However, correlation lengths are always associated to local observables; in particular, they quantify the rate of change (in lattice units) for microscopical observables defined at lattice sites. But no such local observables has been proposed yet, so, even if continuous transitions (like  $B|C_{dS}$  and  $C_b|C_{dS}$ ) are detected by using global order parameters, it is left to verify that a continuum limit is actually reached or not.

We should mention though, that some progress has been obtained by a modification of the RG analysis specifically formulated to overcome this difficulty [14]. The essential idea is to reconstruct the RG flow by following the so called *lines of constant physics*, that are lines in the phase diagram for which the relevant observables, describing large scale features of the configurations, keep constant values. In particular, it has been applied to the  $C$  phases by using as observables the spread of the blobs  $\omega$  in slice time and the size of fluctuations for the spatial volume of slices  $\gamma$ . By mapping both values in the  $C$  region of the phase diagram, one can then try to identify the lines for which the two quantities are simultaneously constant, for example by inspecting the contour lines of the product  $\omega\gamma$ . This procedure clearly follows the philosophy underlying the theory of the Renormalization Group, but it is not clear if some of the assumptions onto which it relies are valid or not [15].

# Chapter 3

## Numerical Implementation

We have already argued (see sec. 2.1.1) that expectation values of observables in CDT can be computed using the definition of mean over the probability distribution the discretized and Wick-rotated path-integral partition function  $Z = \sum_{\mathcal{T} \in \mathcal{S}} e^{-S_E[\mathcal{T}]}$ :

$$\langle \mathcal{O}(\mathcal{T}) \rangle \equiv \frac{1}{Z} \sum_{\mathcal{T} \in \mathcal{S}} \mathcal{O}(\mathcal{T}) e^{-S_E[\mathcal{T}]}, \quad (3.1)$$

where  $\mathcal{S}$  is the configuration space whose elements are the causal triangulations, whereas  $S_E$  is the Wick-rotated Regge action discussed in sec. 2.3. A difficulty is immediately recognized using this formula literally: even for discretized space-time geometries, the configuration space of causal simplicial manifolds  $\mathcal{S}$  is so big that we do not have the resources for doing this sum exactly (it is actually countably infinite!). Hopefully, in practical situations, we do not need to use all the configuration space.

The idea behind numerical simulations of statistical systems is to build a finite sample of the probability distribution over the configuration space of the system and measure observables as averages over this sample. It is understood that this sampling must cover somewhat densely the region of  $\mathcal{S}$  for which the probability is non zero; this requirement must be fulfilled by our simulations, and is called *ergodicity*. There are various approaches we can use to implement this sampling; one of the most used to study statistical and quantum systems is the Markov Chain Monte Carlo (MCMC) method. The idea behind MCMC simulations is to sample the probability distribution describing the system by dynamically evolving (in simulation time, not physical time) a stochastic process over the configuration space using the Markov property: at each step, the new state in the chain is determined only by the actual state of the system.

Usually, the new state is realized by a local modification of the old state<sup>1</sup>: we call one of these elementary transformations between triangulations a *move*, and impose that the set of moves must be ergodic in the sense given above.

In this way we get a sequence  $\{\mathcal{T}_i\}_{i=1}^m$  of configurations occurring with their respective probabilities, from which we can measure observables. Expectation values are then computed using these sequences of measures  $\{\mathcal{O}(\mathcal{T}_i)\}_{i=1}^m$  as a finite sample upon

---

<sup>1</sup>Using some definition of distance between triangulations

which we evaluate the average<sup>2</sup>

$$\langle \mathcal{O}(\mathcal{T}) \rangle \simeq \frac{1}{m} \sum_{i=1}^m \mathcal{O}(\mathcal{T}_i). \quad (3.2)$$

There is a lot of freedom left in implementing the MCMC approach, so it is important to search for the best algorithm in this class<sup>3</sup>.

In the following section we will introduce detailed balance, a further condition on the algorithm, which guarantees a correct sampling of the probability distribution; then we will describe the set of moves and the standard algorithm adopted by Ambjorn et. al. and we will analyze some of its features. Finally we will propose a modification to this algorithm that may cure, in principle, the long autocorrelation times of some observable due to critical slowing down.

## 3.1 Detailed Balance

In complete generality, let  $p : \mathcal{S} \rightarrow \mathbb{R}$  be the probability distribution we want to sample.

In each step of a MCMC simulations, an elementary move transform the starting configuration  $i \in \mathcal{S}$  to a new one  $j \in \mathcal{S}$  (possibly equal to  $i$ ) with a certain *transition probability*  $w_{ji}$  (possibly zero). However, the transition probabilities cannot be arbitrarily chosen, since the configurations sampled by the Markov chain must be distributed, on the long run<sup>4</sup>, like the probability distribution  $p$ . So we must impose that the probability to be in a state  $i$  is correctly reproduced by the sum of the probabilities that a transition from any state  $i$  to  $j$  has occurred, namely

$$p_i = \sum_{j \in \mathcal{S}} w_{ij} p_j, \text{ for each } i. \quad (3.3)$$

Furthermore, by the same definition of transition probability, we have the identity

$$\sum_{j \in \mathcal{S}} w_{ji} = 1, \text{ for each } i. \quad (3.4)$$

Combining the expressions (3.4) and (3.3) we get:

$$\sum_{j \in \mathcal{S}} w_{ji} p_i = \sum_{j \in \mathcal{S}} w_{ij} p_j, \text{ for each } i. \quad (3.5)$$

This condition is leads certainly to a correct sampling of the probability, but it is difficult to check if an algorithm satisfies it. To have simply verifiable guarantees, in

---

<sup>2</sup>We need also to take into account correlations between data, e.g. by using standard resampling methods like Jackknife and Bootstrap [16].

<sup>3</sup>We can measure the efficiency of an algorithm, for example, as the simulation time needed to obtain estimates of observables to a fixed accuracy.

<sup>4</sup>Simulations could start from any initial configuration, the triangulation with slices of minimal size for example (made by 5 tetrahedrons), but on the first steps the configurations sampled would not describe the probability distribution, and one must wait a certain relaxation time before the Markov chain becomes stationary. This process is called *thermalization*, since it is analogous to the attainment of thermodynamical equilibrium between a system and a heat-bath with different temperatures, where the role of temperature is played by the action parameters.

MCMC simulations it is useful to impose a stronger condition for the process, called *detailed balance*<sup>5</sup>; this corresponds simply to dropping the sum over  $j$  in equation (3.5), obtaining:

$$w_{ji} p_i \stackrel{DB}{=} w_{ij} p_j, \text{ for each } i, j \in \mathcal{C}, \quad (3.6)$$

or, in the notation used for causal dynamical triangulations:

$$\mathcal{W}[\mathcal{T}_j \leftarrow \mathcal{T}_i] \mathcal{P}[\mathcal{T}_i] \stackrel{DB}{=} \mathcal{W}[\mathcal{T}_i \leftarrow \mathcal{T}_j] \mathcal{P}[\mathcal{T}_j]. \quad (3.7)$$

In general, the constraint (3.7) do no exhaust the freedom on the specific form of the transition probabilities  $\mathcal{W}$ , which therefore depend upon the algorithm used. In a particular class of Monte-Carlo algorithms, called after *Metropolis*, the transition probabilities can be factorized into two (independent) contributions:

$$\mathcal{W}[\mathcal{T}_j \leftarrow \mathcal{T}_i] = G[\mathcal{T}_j \leftarrow \mathcal{T}_i] \times A[\mathcal{T}_j \leftarrow \mathcal{T}_i], \quad (3.8)$$

where  $G$  denotes the *selection probability*, and  $A$  is also called *acceptance probability*; as the names suggest, the first one can be computed as the probability to *select* the specific transition  $\mathcal{T}_j \leftarrow \mathcal{T}_i$  among all the possible choices, the latter one is fixed by imposing detailed balance, and is used to perform the Metropolis acceptance test. To be more specific, we make an example using the familiar Ising system on a finite lattice with  $N$  sites, configurations  $\sigma = (\sigma(n))_{n=0}^{N-1} \in \Sigma \equiv \{-1, 1\}^N$  and generic distribution probability  $\mathcal{P}[\sigma]$ .

A standard Ising MCMC algorithm can be implemented by uniformly randomly selecting a site in which to attempt a spin-flip by using a yet-to-be-computed acceptance probability. To enforce the detailed balance condition we need to compare a generic pair of configurations  $\sigma_i$  and  $\sigma_j$ ; as defined above, it is clear that configurations differing by more than a single spin-flip (Hamming distance above 1) cannot possibly be joined by a single MC step. This means that the selection probabilities  $G[\sigma_j \leftarrow \sigma_i]$  and  $G[\sigma_i \leftarrow \sigma_j]$  are zero and then detailed balance is trivial for these pairs (the majority).

Less trivial is comparing configurations  $\sigma_i$  and  $\sigma_j$  differing by a single spin-flip: selection probabilities are due only to the choice of a site among all  $N$ , and because of uniform selection it reads  $G[\sigma_j \leftarrow \sigma_i] = G[\sigma_i \leftarrow \sigma_j] = \frac{1}{N}$ . The detailed balance condition now reads:

$$\frac{1}{N} \times A[\sigma_j \leftarrow \sigma_i] \mathcal{P}[\sigma_i] \stackrel{DB}{=} \frac{1}{N} \times A[\sigma_i \leftarrow \sigma_j] \mathcal{P}[\sigma_j] \quad (3.9)$$

Observe that here the selection probabilities  $G = \frac{1}{N}$  can be simplified away; for the Ising system this remains true even adopting a non-uniform site selection, but for CDT the form of selection probabilities becomes relevant, as shown soon.

Acceptance probabilities  $A$ , in the range  $[0, 1]$ , can be computed by maximization of the total acceptance probability (Metropolis algorithm), so finally we obtain the expressions:

$$A[\sigma_j \leftarrow \sigma_i] = \min \left( 1, \frac{\mathcal{P}[\sigma_j]}{\mathcal{P}[\sigma_i]} \right), \quad A[\sigma_i \leftarrow \sigma_j] = \min \left( 1, \frac{\mathcal{P}[\sigma_i]}{\mathcal{P}[\sigma_j]} \right). \quad (3.10)$$

---

<sup>5</sup>This is similar, for example, to the microscopic reversibility of chemical reactions at equilibrium. Here the reversibility is intended in simulation time, not physical time.

In a more general setting, like the one of CDT, selection probabilities cannot be simplified away, and then we get:

$$A[\mathcal{T}_j \leftarrow \mathcal{T}_i] = \min \left( 1, \frac{G[\mathcal{T}_i \leftarrow \mathcal{T}_j] \mathcal{P}[\mathcal{T}_j]}{G[\mathcal{T}_j \leftarrow \mathcal{T}_i] \mathcal{P}[\mathcal{T}_i]} \right), A[\mathcal{T}_i \leftarrow \mathcal{T}_j] = \min \left( 1, \frac{G[\mathcal{T}_j \leftarrow \mathcal{T}_i] \mathcal{P}[\mathcal{T}_i]}{G[\mathcal{T}_i \leftarrow \mathcal{T}_j] \mathcal{P}[\mathcal{T}_j]} \right). \quad (3.11)$$

Choosing moves and rules for the updating, we still need to determine explicit formulas for selection probabilities  $G[\mathcal{T}' \leftarrow \mathcal{T}]$ , in order to compute from eq. (3.11) the probability with which moves should be accepted or rejected.

### The configuration space

An ingredient we must specify yet, is the exact form of the configuration space adopted for CDT simulations; from General Relativity, each spacetime is identified by its metric properties up to diffeomorphisms; from this point of view, triangulations with the same *relations* between simplices (i.e. defining the same abstract simplicial complex) are considered to be equivalent (Regge Calculus).

Recall that triangulations are made by abstract simplices, that is, they are not explicitly embedded in any space. In practice, if we are implementing the Markov Chain evolution of a dynamical triangulation, we need to mark different simplices by labels, so that we can make a random selection of simplices in order to attempt some move; but we are *moving* in a configuration space different from the one said before, because we are considering now labeled triangulations, differing not only by the simplicial complex structure but also by different labeling of simplices. This results in an overcounting of the configurations, since two abstract triangulations would have multiple representations in terms of labeled triangulations.

This difference must be taken into account in the actual implementation of CDT code, since it affects the expressions for selection probabilities. Recalling that we are approximating discretely a sum over metrics modulo diffeomorphisms, another source of overcounting is caused by possible symmetries in an abstract triangulation. In general, if the automorphism group of a triangulation  $\mathcal{T}$  has cardinality  $C(\mathcal{T}) > 1$ , we should consider the two realizations of the triangulation as representing the same geometry, so the correct forms for the partition function and probability would be

$$Z = \sum_{\mathcal{T}} \frac{1}{C(\mathcal{T})} e^{-S[\mathcal{T}]}, \quad (3.12)$$

$$\mathcal{P}[\mathcal{T}] = \frac{1}{C(\mathcal{T})} e^{-S[\mathcal{T}]}.$$

Notice that, in the continuous version of the path-integral (eq. (2.9)), the term  $\frac{1}{C(\mathcal{T})}$  corresponds to the operation of taking the *modulo* over diffeomorphisms when integrating over the space of metrics. But, like in the continuum case, configurations with these symmetries form a set of measure zero with respect to typical configurations, so this term can be safely omitted in the implementation.

It is noteworthy to mention that admissible triangulations must satisfy the so called *simplicial manifold constraint*: multiple simplices with the same set of vertices (for example two links sharing the same endpoints) are not allowed. This means that updates leading the configuration towards a new one violating this property

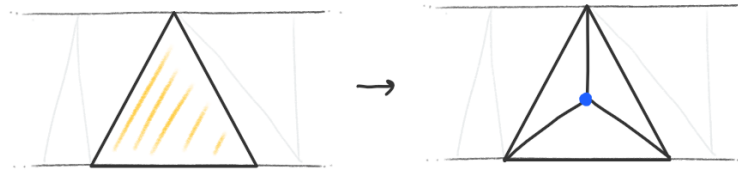


Figure 3.1: Attempt to perform a Pachner move, flipping a 2-simplex into a 0-simplex, in a 2-dimensional causal triangulation. The new vertex will not belong to any slice.

must be accepted with probability 0, and therefore checks to verify if a given simplex does not exist yet must be performed in the actual code<sup>6</sup>.

In the following section we will describe the standard algorithm used for 4-dimensional CDT; to the author knowledge, this is the only one present at the time of this writing.

## 3.2 Alexander moves

The set of local ergodic moves used in Euclidean DT simulations (Pachner moves) consists of *flipping* (read exchange) a  $k$ -dimensional simplex by its  $(d-k)$ -dimensional dual, for  $k \in \{0, 1, \dots, d\}$ . The main feature of CDT, that distinguishes it from DT, is the causal (foliated) structure of the triangulation; Pachner moves do not certainly preserve this property (e.g., see figure 3.1), so cannot be used for CDT simulations. The set of moves currently adopted in CDT simulations is given by the *Alexander moves*<sup>7</sup>, that can be seen as a suitable modification of the Pachner moves, adapted to the foliated structure of CDT triangulations. In the following we will refer to the abstract set of moves using the notation  $\mathcal{M}$ .

For the detailed balance condition to make sense, every move must have an inverse move in the set; while the inverse of the  $k$ -th Pachner move is simply the  $(d-k)$ -th Pachner move, this symmetry is absent in Alexander moves, resulting in a more convoluted implementation.

Another feature of these moves is *locality*: the new triangulation in the MCMC evolution is generated by the transformation of a subcomplex of simplices, leaving the rest of the triangulation unaltered. Each move  $m$  in the set  $\mathcal{M}$  can be performed only on local subcomplexes having a structure specific for the move; for conciseness we will informally call these subcomplexes *cells*<sup>8</sup>, and we will say that  $m$  is *associated* to the set of cells  $\mathcal{C}_{\mathcal{T},m}$ , where  $\mathcal{T}$  is the underlying triangulation. It is essential, for efficiency of the implementation, to use data structures that keep track of all the cells of a triangulation for each move, so to guarantee fast access (appendix A). We denote by  $(n \rightarrow m)$  the move that transforms a cell with  $n$  maximal simplices

<sup>6</sup>This is efficiently implemented by the use of *hash sets*, particular data structures that guarantee (in most cases) a constant time access.

<sup>7</sup>Actually, ergodicity of the Alexander moves has not yet been proved for 4D CDT.

<sup>8</sup>This term is non-standard terminology, and should not be confused with the name given to the elementary building blocks of CW complexes.

to a cell with  $m$  maximal simplices, preserving the triangulation outside the cell.

In the following subsections we will describe in detail the implementation of the moves currently adopted for CDT simulations in 2D, 3D and 4D. We warn that the next figures have the only purpose to represent the changes in the adjacency relations between simplices in the triangulation, but, in fact, each spacelike link is tacitly understood to have a fixed length  $a$ .

### 3.2.1 Alexander moves in 2D

In 2-dimensional CDT, vertices and triangles form a dual pair, while links are self-dual. To guarantee ergodicity, we need a set of 3 moves: the self-dual ( $2 \rightarrow 2$ ), and the pair of dual<sup>9</sup> moves ( $2 \rightarrow 4$ ) and ( $4 \rightarrow 2$ ).

For convenience, we recall the action parametrization in 2D simulations eq. (2.21)

$$S_{EH}^{(2D)}[\mathcal{T}] = \lambda N_2[\mathcal{T}], \quad (3.14)$$

where  $N_2[\mathcal{T}]$  is the total number of triangles in the triangulation  $\mathcal{T}$  and  $\lambda$  is related to the cosmological constant.

#### move ( $2 \rightarrow 2$ )

The structure of a cell for this move is a pair of oppositely oriented triangles sharing a timelike link. We must check that the link does not exist already, in order to not violate the simplicial manifold property of the triangulation (sec. 3.1).

Labeling vertices as in figure 3.2, the ( $2 \rightarrow 2$ ) move can be represented by the ‘vertex formula’

$$123 + 234 \leftrightarrow 124 + 134, \quad (3.15)$$

while the types of triangles in a cell are opposite, and by self-duality unchanged, as represented by the ‘type formula’

$$(1, 2) + (2, 1) \leftrightarrow (1, 2) + (2, 1), \quad (3.16)$$

counting the number of maximal simplexes of given kinds (this would be more useful for higher dimensions).

The global number of triangles does not change, so as for the value of the action:

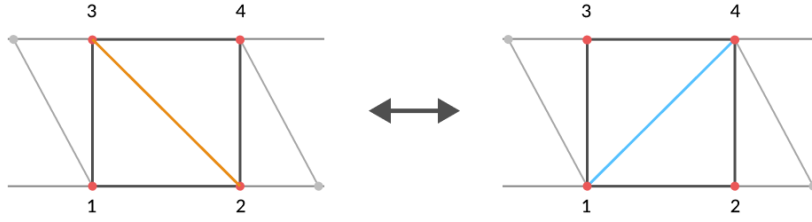
$$\Delta S_{(2 \rightarrow 2)} = 0. \quad (3.17)$$

#### moves ( $2 \rightarrow 4$ ) and ( $4 \rightarrow 2$ )

The structure of a cell for the ( $2 \rightarrow 4$ ) move is a pair of triangles sharing a spacelike link, while the inverse move, ( $4 \rightarrow 2$ ), can be performed only on cells containing a vertex shared by exactly 4 triangles; in the following we will call *coordination number* of a simplex, the number of maximal simplexes to which it belongs. It is easy to see that these requirements completely characterize the structure of the cells

---

<sup>9</sup>Here we will call two moves *dual* if they are one the inverse of the other

Figure 3.2: Move  $(2 \rightarrow 2)$ .

as depicted in figure 3.3.

The ‘vertex formula’ for these moves, following the labeling in figure, is

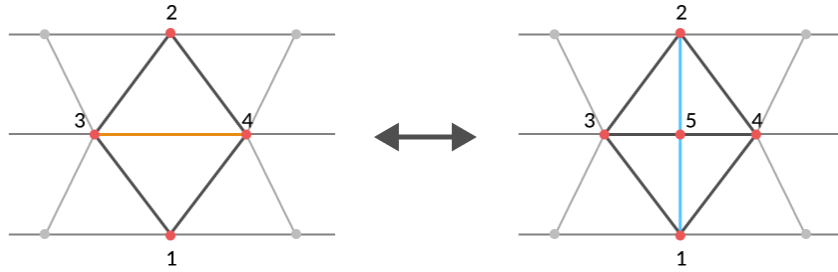
$$134 + 234 \leftrightarrow 135 + 145 + 235 + 245, \quad (3.18)$$

while the ‘type formula’ reads

$$(1, 2) + (2, 1) \leftrightarrow 2 \times (1, 2) + 2 \times (2, 1). \quad (3.19)$$

The net change in the number of triangles is  $+2$  for the  $(2 \rightarrow 4)$  move and  $-2$  for the  $(4 \rightarrow 2)$  move, then

$$\Delta S_{(2 \rightarrow 4)} = -\Delta S_{(4 \rightarrow 2)} = 2\lambda. \quad (3.20)$$

Figure 3.3: Move  $(2 \rightarrow 4)$  and its inverse  $(4 \rightarrow 2)$ .

### 3.2.2 Alexander moves in 3D

In 3-dimensional CDT, vertices are dual to tetrahedra, and links are dual to triangles. There are 5 Alexander moves:  $(4 \rightarrow 4)$  is self-dual, while  $(2 \rightarrow 3)/(3 \rightarrow 2)$  and  $(2 \rightarrow 6)/(6 \rightarrow 2)$  are pairs of dual moves. For convenience, we recall the action parametrization used in 3-dimensional CDT simulations with  $\tilde{\alpha} = 1$ :

$$S_{EH}^{(3D)}[\mathcal{T}] = -k_1 N_1[\mathcal{T}] + k_3 N_3[\mathcal{T}], \quad (3.21)$$

where  $N_1[\mathcal{T}]$  is the total number of links, and  $N_3[\mathcal{T}]$  is the total number of tetrahedra (of arbitrary type) in the triangulation  $\mathcal{T}$ .

### move $(4 \rightarrow 4)$

The cell structure associated to this move is depicted in figure 3.4 and is completely specified by the presence of an internal spacelike link with coordination number 4 to be spatially flipped. This happens because a spacelike link is shared by exactly two spacelike triangles, and both the latter are shared by exactly two oppositely oriented  $(3, 1)$ -tetrahedra; it follows that each spacelike link is shared by *at least* 4 tetrahedra, two of  $(3, 1)$  and two of  $(1, 3)$  type. The importance of specifying completely the cell structure of a move by using some simple feature will be discussed in the subsection about data structures A. Notice that these moves, projected on the spatial slice containing the flipped link, is analogous to the  $(2 \rightarrow 2)$  Pachner move in 2D.

As explained in the 2D case, we must check that the new link does not exist already to not violate the simplicial manifold property.

Referring to figure 3.4, the  $(4 \rightarrow 4)$  move can be represented by the ‘vertex formula’

$$1235 + 1345 + 2356 + 3456 \leftrightarrow 1234 + 1245 + 2346 + 2456, \quad (3.22)$$

while the types of tetrahedra in a cell are unchanged due to self-duality, as represented by the ‘type formula’

$$2 \times (1, 3) + 2 \times (3, 1) \leftrightarrow 2 \times (1, 3) + 2 \times (3, 1). \quad (3.23)$$

The number of simplexes of given kind do not change, so as the value of the action:

$$\Delta S_{(4 \rightarrow 4)} = 0. \quad (3.24)$$

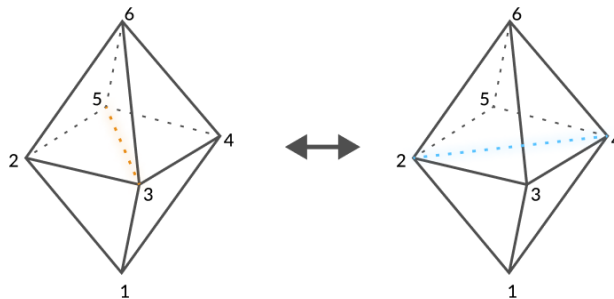


Figure 3.4: Move  $(4 \rightarrow 4)$ .

### moves $(2 \rightarrow 3)$ and $(3 \rightarrow 2)$

The move  $(2 \rightarrow 3)$  consists in flipping a timelike triangle to a timelike link; this can be done only if the triangle forms the interface between a  $(2, 2)$  and a  $(3, 1)$  or  $(1, 3)$

tetrahedron as depicted in figure 3.5. Notice that the cell structures associated to the moves  $(2 \rightarrow 3)$  and  $(3 \rightarrow 2)$  cannot be uniquely characterized by simple features of a simplex; drawbacks of this fact will be discussed in the section about data structures A.

The ‘vertex formula’ for these moves, following the labeling in figure 3.5, is

$$1354 + 2345 \leftrightarrow 1234 + 1235 + 1245, \quad (3.25)$$

while the ‘type formula’, modulo time-reversal, reads

$$(3, 1) + (2, 2) \leftrightarrow (3, 1) + 2 \times (2, 2). \quad (3.26)$$

A link is added in move  $(2 \rightarrow 3)$  and removed in move  $(3 \rightarrow 2)$ , while the net change in the number of tetrahedra is  $+1$  for the  $(2 \rightarrow 3)$  move and  $-1$  for the  $(3 \rightarrow 2)$  move, then

$$\Delta S_{(2 \rightarrow 3)} = -\Delta S_{(3 \rightarrow 2)} = -k_1 + k_3. \quad (3.27)$$

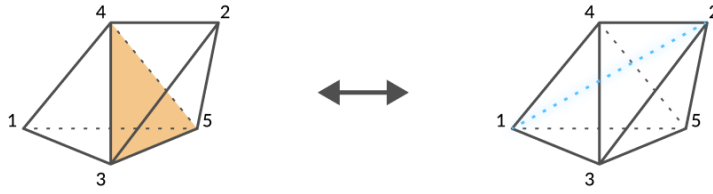


Figure 3.5: Move  $(2 \rightarrow 3)$  and its inverse  $(3 \rightarrow 2)$ .

### moves $(2 \rightarrow 6)$ and $(6 \rightarrow 2)$

For the  $(2 \rightarrow 6)$  move, a spacelike triangle is replaced by three spacelike triangles sharing a newly created vertex; in the inverse move  $(6 \rightarrow 2)$ , a vertex with coordination number 6 is removed and replaced by a triangle. Notice the similarity of these moves and the  $(2 \rightarrow 4)/(4 \rightarrow 2)$  moves already described in the 2D case. Figure 3.6 shows the cell transformations.

The ‘vertex formula’ for these moves, following the labeling in figure 3.6, is

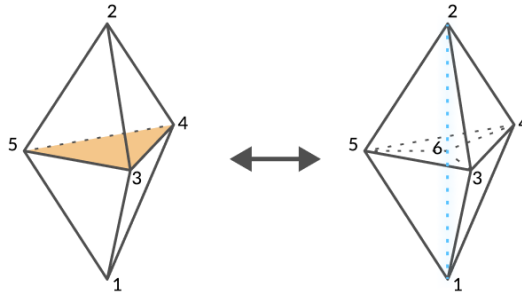
$$\begin{aligned} & 1345 + 3452 \\ & \Downarrow \\ & 1346 + 1356 + 1456 + 2346 + 2356 + 2456, \end{aligned} \quad (3.28)$$

while the ‘type formula’ reads

$$(3, 1) + (1, 3) \leftrightarrow 3 \times (3, 1) + 3 \times (1, 3). \quad (3.29)$$

Five links (three spacelike and two timelike) are added in the  $(2 \rightarrow 6)$  and removed in the  $(6 \rightarrow 2)$  move, while the net change in the number of tetrahedra is  $+4$  for the  $(2 \rightarrow 6)$  and  $-4$  for the  $(6 \rightarrow 2)$  move, from which follows that

$$\Delta S_{(2 \rightarrow 6)} = -\Delta S_{(6 \rightarrow 2)} = -5k_1 + 4k_3. \quad (3.30)$$

Figure 3.6: Move  $(2 \rightarrow 6)$  and its inverse  $(6 \rightarrow 2)$ .

### 3.2.3 Alexander moves in 4D

In 4-dimensional CDT simulations, vertices are dual to pentachorons, links to tetrahedra, and triangles are self-dual. There are 7 Alexander moves:  $(3 \rightarrow 3)$  is self-dual, while  $(2 \rightarrow 4)/(4 \rightarrow 2)$ ,  $(4 \rightarrow 6)/(6 \rightarrow 4)$  and  $(2 \rightarrow 6)/(6 \rightarrow 2)$  are pairs of dual moves. For convenience, we recall the action parametrization (2.27) used in 4-dimensional CDT simulations:

$$S_{EH}^{(4D)}[\mathcal{T}] = -k_0 N_0[\mathcal{T}] + k_4 N_4[\mathcal{T}] + \Delta(N_4[\mathcal{T}] + N_4^{(4,1)}[\mathcal{T}] - 6N_0[\mathcal{T}]), \quad (3.31)$$

where  $N_0[\mathcal{T}]$  is the total number of vertices,  $N_4[\mathcal{T}]$  is the total number of pentachorons of any kind, i.e. a measure of the total space-temporal volume, and  $N_4^{(4,1)}[\mathcal{T}]$  is the total number of pentachorons types  $(4, 1)$  or  $(1, 4)$  in the triangulation  $\mathcal{T}$ . Conversely to the 2D and 3D case, here we left a term parametrized by  $\Delta$ , encoding the asymmetry between timelike and spacelike link lengths due to the freedom in choosing the  $\tilde{\alpha}$  parameter of the Wick rotation.  $\Delta$  is defined in such a way that in absence of asymmetry ( $\tilde{\alpha} = 1$ ) this term vanishes ( $\Delta = 0$ ).

#### move $(3 \rightarrow 3)$

This self-dual move consists in flipping a timelike triangle shared by 3 pentachorons to another timelike triangle.

There are two different cell types that can occur, depending on the relative time-orientation of the initial and final timelike triangles: if they are equal we call it a  $(3 \rightarrow 3)$  move of *I kind* (figure 3.7), it is a  $(3 \rightarrow 3)$  move of *II kind* (figure 3.8).

A cell of this kinds can be accessed by looking to the set of timelike triangles shared by exactly 3 pentachorons. However, not all initial triangles of this type are valid, since we must still check that the final triangle is not spatial, rejecting the move in the eventuality.

Referring to the vertex labeling shown in figure 3.7 and figure 3.8, the ‘vertex formulas’ for the two kinds of moves are the same, and are given by

$$12456 + 13456 + 23456 \leftrightarrow 12345 + 12346 + 12356. \quad (3.32)$$

while the ‘type formula’ is different for the two kinds:

- I kind:

$$(4, 1) + 2 \times (3, 2) \leftrightarrow (4, 1) + 2 \times (3, 2) \quad (3.33)$$

- II kind:

$$(2, 3) + 2 \times (3, 2) \leftrightarrow (2, 3) + 2 \times (3, 2) \quad (3.34)$$

The number of simplexes of given kind do not change, and therefore also the value of the action:

$$\Delta S_{(3 \rightarrow 3)} = 0. \quad (3.35)$$

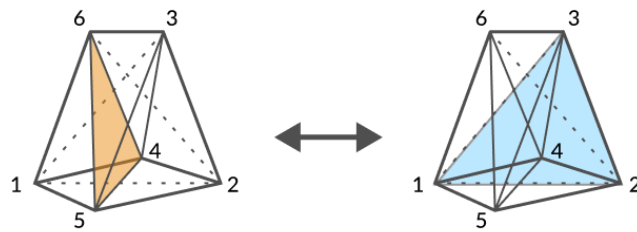


Figure 3.7: Move  $(3 \rightarrow 3)$  I kind.

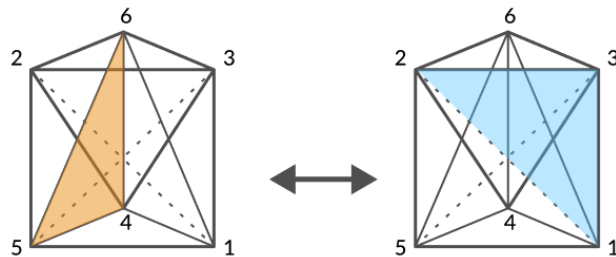


Figure 3.8: Move  $(3 \rightarrow 3)$  II kind.

### moves $(2 \rightarrow 4)$ and $(4 \rightarrow 2)$

The move  $(2 \rightarrow 4)$  consists in flipping a non-spatial tetrahedron to a timelike link. There are two types of associated cells that could occur, depending on the type of the tetrahedron to be flipped: we call of *I kind* the  $(2 \rightarrow 4)/(4 \rightarrow 2)$ -move involving a  $(3, 1)/(1, 3)$  tetrahedron, and of *II kind* the  $(2 \rightarrow 4)/(4 \rightarrow 2)$ -move involving a  $(2, 2)$  tetrahedron. The cell structure associated to the inverse move  $(4 \rightarrow 2)$  can be

characterized by the presence of a timelike link shared by exactly 4 pentachorons, and such that can be flipped to a non-spatial tetrahedron.

Referring to the vertex labeling shown in figure 3.9 and figure 3.10, the ‘vertex formulas’ for the two kinds of moves (and anti-moves) are the same, and are given by

$$13456 + 23456 \rightarrow 12345 + 12346 + 12456 + 12356, \quad (3.36)$$

while the ‘type formula’, modulo time reversal, is different for the two kinds of moves:

- I kind:

$$(4, 1) + (3, 2) \leftrightarrow (4, 1) + 3 \times (3, 2) \quad (3.37)$$

- II kind:

$$(2, 3) + (3, 2) \leftrightarrow 2 \times (2, 3) + 2 \times (3, 2) \quad (3.38)$$

No vertex is added or removed, and for both kinds of  $(2 \rightarrow 4)$  moves the net change in the number of  $(3, 2)/(2, 3)$  pentachorons is  $+2$  (the opposite for the inverse move), then, the action increment is

$$\Delta S_{(2 \rightarrow 4)} = -\Delta S_{(4 \rightarrow 2)} = +2k_4 + 2\Delta. \quad (3.39)$$

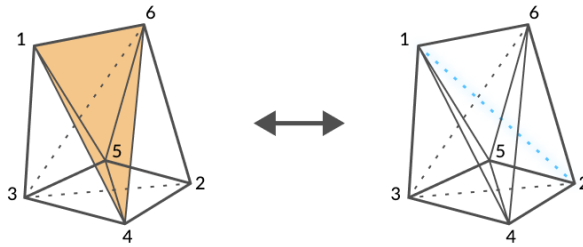


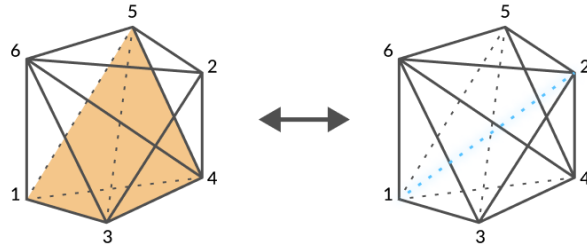
Figure 3.9: Move  $(2 \rightarrow 4)$  and its inverse  $(4 \rightarrow 2)$ , I kind.

### moves $(4 \rightarrow 6)$ and $(6 \rightarrow 4)$

In the  $(4 \rightarrow 6)$  move, a spacelike triangle with coordination number 4 is replaced by a spatial link with coordination number 6; conversely for the  $(6 \rightarrow 4)$  move. Furthermore all pentachorons in the cell must be of types  $(4, 1)$  or  $(1, 4)$  as shown in figure 3.11. Notice that, restricted to the spatial slice involved, these are Pachner moves of the euclidean slice sub-triangulation.

The ‘vertex formula’ for these moves, following the labeling in figure 3.11, is

$$\begin{aligned} & 12345 + 23457 + 13456 + 34567 \\ & \Downarrow \\ & 12346 + 23467 + 12356 + 23567 + 12456 + 24567, \end{aligned} \quad (3.40)$$

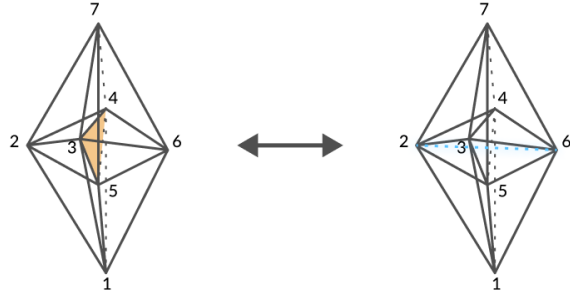
Figure 3.10: Move  $(2 \rightarrow 4)$  and its inverse  $(4 \rightarrow 2)$ , II kind.

while the 'type formula' reads

$$2 \times (4, 1) + 2 \times (1, 4) \leftrightarrow 3 \times (4, 1) + 3 \times (1, 4). \quad (3.41)$$

No vertex is added or removed, while the net change in the number of  $(4, 1)/(1, 4)$  pentachorons is  $+2$  for the  $(4 \rightarrow 6)$  move and  $-2$  for the inverse, then

$$\Delta S_{(4 \rightarrow 6)} = -\Delta S_{(6 \rightarrow 4)} = +2k_4 + 4\Delta. \quad (3.42)$$

Figure 3.11: Move  $(4 \rightarrow 6)$  and its inverse  $(6 \rightarrow 4)$ .

### moves $(2 \rightarrow 8)$ and $(8 \rightarrow 2)$

In the  $(2 \rightarrow 8)$  move, shown in figure 3.11, a spacelike tetrahedron, is replaced by 4 spacelike tetrahedra sharing a newly created vertex; in the inverse move a vertex with coordination 4 is removed. Recall that spatial tetrahedra are shared exactly by two pentachorons, one of type  $(4, 1)$  and one of type  $(1, 4)$ . These moves are the four dimensional analogues of moves  $(2 \rightarrow 4)/(4 \rightarrow 2)$  in two and  $(2 \rightarrow 6)/(6 \rightarrow 2)$  in three dimensional CDT, and the only ones responsible for creation/destruction of vertices.

The 'vertex formula' for these moves, following the labeling in figure 3.12, is

$$\begin{aligned}
 & 13456 + 23456 \\
 & \Downarrow \\
 & 13457 + 23457 + 13467 + 23467 \\
 & + 13567 + 23567 + 14567 + 24567,
 \end{aligned} \quad (3.43)$$

while the 'type formula' reads

$$(4, 1) + (1, 4) \leftrightarrow 4 \times (4, 1) + 4 \times (1, 4). \quad (3.44)$$

One vertex is added in the  $(2 \rightarrow 8)$  move, and removed in the  $(8 \rightarrow 2)$  move, while the net change in the number of  $(4, 1)/(1, 4)$  pentachorons is  $+6$  for the  $(2 \rightarrow 8)$  move and  $-6$  for the inverse, then

$$\Delta S_{(2 \rightarrow 8)} = -\Delta S_{(8 \rightarrow 2)} = -k_0 + 6k_4 + 6\Delta. \quad (3.45)$$

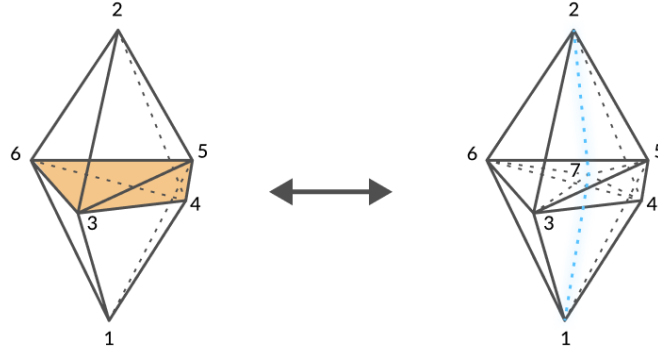


Figure 3.12: Move  $(2 \rightarrow 8)$  and its inverse  $(8 \rightarrow 2)$ .

### 3.3 Description and analysis of the standard algorithm

Having identified a set of moves  $\mathcal{M}$ , each with associated subcomplex structure  $\mathcal{C}$ , we can describe the standard algorithm by AJL [4].

We now adopt a constructive approach, that will be useful later for generalizations of the algorithm.

A single Monte Carlo step can be summarized by the following procedure:

- Start from a triangulation  $\mathcal{T}_i$ .
- Choose to try making a move  $m \in \mathcal{M}_{\mathcal{T}_i}$ , with p.d.f.  $g_{\mathcal{M}}^{(\mathcal{T}_i)}(m)$  (the set  $\mathcal{M}_{\mathcal{T}_i}$  does not depend really on the triangulation, but is just the set of Alexander moves discussed above).
- Select a cell  $c \in \mathcal{C}_{\mathcal{T}_i, m}$  on which try making the move  $m$ , with p.d.f.  $g_{\mathcal{C}}^{(\mathcal{T}_i)}(c; m)$ .
- Compute<sup>10</sup> the (attempted) new configuration  $\mathcal{T}_j = \mathcal{F}_{m, c}(\mathcal{T}_i)$ , where  $\mathcal{F}_{m, c}$  represents the unique map from  $\mathcal{T}_i$  to  $\mathcal{T}_j$  that can be performed having chosen the move  $m \in \mathcal{M}$  and an associated cell  $c \in \mathcal{C}_{\mathcal{T}_i, m}$ .

<sup>10</sup>This step is actually unnecessary in CDT, because the move can be rejected without modifying the triangulation. Indeed, the acceptance probabilities can always be computed in the initial configuration  $\mathcal{T}_i$  (see example 3.3.1), and the action differences have been precomputed in the previous section for each move.

- Impose DB and compute the acceptance probability  $A[\mathcal{T}_j \leftarrow \mathcal{T}_i]$  to be used for the Metropolis test; if the test is passed, accept  $\mathcal{T}_j$  as the starting configuration for the next Monte Carlo step, else do not transform the triangulation.

From the steps above we can read the selection probability to go from  $\mathcal{T}_i$  to  $\mathcal{T}_j$ :

$$G[\mathcal{T}_j \leftarrow \mathcal{T}_i] = \sum_{\{(m,c) | \mathcal{F}_{m,c}(\mathcal{T}_i) = \mathcal{T}_j\}} g_{\mathcal{M}}^{(\mathcal{T}_i)}(m) g_{\mathcal{C}}^{(\mathcal{T}_i)}(c; m), \quad (3.46)$$

then the detailed balance condition reads

$$\sum_{\{(m,c) | \mathcal{F}_{m,c}(\mathcal{T}_i) = \mathcal{T}_j\}} g_{\mathcal{M}}^{(\mathcal{T}_i)}(m) g_{\mathcal{C}}^{(\mathcal{T}_i)}(c; m) A[\mathcal{T}_j \leftarrow \mathcal{T}_i] \mathcal{P}[\mathcal{T}_i] \quad (3.47)$$

$$\stackrel{DB}{=} \quad (3.48)$$

$$\sum_{\{(\bar{m}, \bar{c}) | \mathcal{F}_{\bar{m}, \bar{c}}(\mathcal{T}_j) = \mathcal{T}_i\}} g_{\mathcal{M}}^{(\mathcal{T}_j)}(\bar{m}) g_{\mathcal{C}}^{(\mathcal{T}_j)}(\bar{c}; \bar{m}) A[\mathcal{T}_i \leftarrow \mathcal{T}_j] \mathcal{P}[\mathcal{T}_j], \quad (3.49)$$

where we denoted by  $\bar{m}$  the move inverse of  $m$ , and by  $\bar{c}$  the cell  $c$  after transformation by  $m$ .

We have still the freedom to choose the selection probabilities  $g_{\mathcal{M}}$ . In the standard implementation the simplest choice is given by selecting moves and associated anti-moves with equal probabilities:

$$g_{\mathcal{M}}^{(\mathcal{T})}(m) = g_{\mathcal{M}}^{(\bar{\mathcal{T}})}(\bar{m}), \text{ for each } \bar{\mathcal{T}} \in \{\mathcal{F}_{m,c}(\mathcal{T}) | c \in \mathcal{C}_{\mathcal{T},m}\}. \quad (3.50)$$

In this way non-dual moves are decoupled in the detailed balance equation; by definition of probability, we need only to satisfy the constraint  $\sum_{m \in \mathcal{M}} g_{\mathcal{M}}^{(\mathcal{T})}(m) = 1$ <sup>11</sup>.

Then, the detailed balance condition for an arbitrary move  $m \in \mathcal{M}$  reads:

$$g_{\mathcal{C}}^{(\mathcal{T}_i)}(c; m) A[\mathcal{T}_j \leftarrow \mathcal{T}_i] \mathcal{P}[\mathcal{T}_i] \stackrel{DB}{=} g_{\mathcal{C}}^{(\mathcal{T}_j)}(\bar{c}; \bar{m}) A[\mathcal{T}_i \leftarrow \mathcal{T}_j] \mathcal{P}[\mathcal{T}_j], \quad (3.51)$$

where  $c$  is the unique cell in  $\mathcal{T}_i$  that transformed by  $m$  gives  $\mathcal{T}_j$ , while  $\bar{c}$  is the unique cell in  $\mathcal{T}_j$  that transformed by  $\bar{m}$  gives  $\mathcal{T}_i$  (observe that  $c$  and  $\bar{c}$  have the same boundary).

Finally, as explained in sec. 3.1, we get:

$$A[\mathcal{T}_j \leftarrow \mathcal{T}_i] = \min \left( 1, \frac{g_{\mathcal{C}}^{(\mathcal{T}_j)}(\bar{c}; \bar{m}) \mathcal{P}[\mathcal{T}_j]}{g_{\mathcal{C}}^{(\mathcal{T}_i)}(c; m) \mathcal{P}[\mathcal{T}_i]} \right), \quad A[\mathcal{T}_i \leftarrow \mathcal{T}_j] = \min \left( 1, \frac{g_{\mathcal{C}}^{(\mathcal{T}_i)}(c; m) \mathcal{P}[\mathcal{T}_i]}{g_{\mathcal{C}}^{(\mathcal{T}_j)}(\bar{c}; \bar{m}) \mathcal{P}[\mathcal{T}_j]} \right), \quad (3.52)$$

where it is understood that  $m$  and  $c$  are the unique move and associated cell for which  $\mathcal{F}_{m,c}(\mathcal{T}_i) = \mathcal{T}_j$ .

Cell selection probabilities depend on the move and on the implementation; now we will give an example of this computation applying the detailed balance condition to the dual pair of moves  $(2 \rightarrow 6)/(6 \rightarrow 2)$  in 3-dimensional CDT, and discussing the philosophy about the particular choice of data structures.

<sup>11</sup>A simplistic criterion for choosing the specific values for  $g_{\mathcal{M}}$  could be to make the number of accepted moves of each kind identical (uniform prior). A posteriori, after having gathered sufficient date, the freedom on the algorithmic parameters should be always devoted to get the most possibly uncorrelated configuration in the least possible time (*decorrelation*).

### 3.3.1 Example: acceptance probability computation in 3D

Let us consider the pair of dual moves  $(2 \rightarrow 6)/(6 \rightarrow 2)$  described in 3.2.2. Before applying the detailed balance condition to this moves we need to compute the cell selection probabilities. The latter are not universal, but depend on the way we choose different cells in the code and then, ultimately, on the data structures we employ.

In a triangulation  $\mathcal{T}_i$ , every cell  $c \in \mathcal{C}_{\mathcal{T}_i, (2 \rightarrow 6)}$  associated to the  $(2 \rightarrow 6)$  move can be uniquely identified by the spatial triangle shared by two  $(1, 3)/(3, 1)$  tetrahedra. We could maintain a data structure containing all the spatial triangles, but this is not really necessary. In general  $d$  dimensions, it can be shown that it is sufficient to maintain information about all  $k$ -simplexes except the  $k = d - 1$  ones (e.g. triangles in  $d = 3$ ); this information is needed only in rare cases and its update would be computationally expensive<sup>12</sup>. It is easy to identify every cell in  $\mathcal{C}_{\mathcal{T}_i, (2 \rightarrow 6)}$  simply by maintaining the set of all  $(3, 1)$  and  $(1, 3)$  tetrahedra, because for each space triangle there are exactly two elements from this set. Then, for the  $(2 \rightarrow 6)$  move, we select uniformly at random a  $(1, 3)$  or  $(3, 1)$  tetrahedron and access the corresponding cell; there are  $|\mathcal{C}_{\mathcal{T}_i, (2 \rightarrow 6)}| = N_2^{SL}[\mathcal{T}_i] = \frac{N_3^{(3,1)}[\mathcal{T}_i]}{2}$  distinct initial cells, so the cell selection probability for the  $(2 \rightarrow 6)$  move in the configuration  $\mathcal{T}_i$  is

$$g_c^{(\mathcal{T}_i)}(c; (2 \rightarrow 6)) = \frac{1}{|\mathcal{C}_{\mathcal{T}_i, (2 \rightarrow 6)}|} = \frac{2}{N_3^{(3,1)}[\mathcal{T}_i]}, \text{ for each } c \in \mathcal{C}_{\mathcal{T}_i, (2 \rightarrow 6)}. \quad (3.53)$$

Regarding the inverse move  $(6 \rightarrow 2)$ , we have to remove a vertex with coordination number 6 from the triangulation  $\mathcal{T}_j$ . It can be verified easily that a vertex of such kind must necessarily be shared by 3 tetrahedra of  $(3, 1)$  type and 3 of  $(1, 3)$  type, so that its neighbourhood has precisely the form of a cell  $\bar{c} \in \mathcal{C}_{\mathcal{T}_j, (6 \rightarrow 2)}$ . Therefore, the number of cells of this kind is simply the number of vertices with coordination number 6, denoted by the variable  $N_{60}$ . In the data structure we can maintain a list of vertices of such kind and select randomly one of them in order to perform the move  $(6 \rightarrow 2)$ <sup>13</sup>. So, the selection probability for a  $(6 \rightarrow 2)$  move starting from the configuration  $\mathcal{T}_j$  is

$$g_c^{(\mathcal{T}_j)}(\bar{c}; (6 \rightarrow 2)) = \frac{1}{|\mathcal{C}_{\mathcal{T}_j, (6 \rightarrow 2)}|} = \frac{1}{N_{60}[\mathcal{T}_j]}, \text{ for each } \bar{c} \in \mathcal{C}_{\mathcal{T}_j, (6 \rightarrow 2)}. \quad (3.54)$$

Substituting the expressions for selection probabilities (3.53) and (3.54) in eq. (3.52) we obtain the acceptance probabilities for the moves  $(2 \rightarrow 6)/(6 \rightarrow 2)$  and for the

---

<sup>12</sup>When we need to check violations of the simplicial manifold constraints (discussed in 3.1), we should still be able to reconstruct the information on  $(d - 1)$ -simplexes from the data structures of 0-simplexes and  $d$ -simplexes.

<sup>13</sup>The vertex data structure must contain at least a reference to a neighbouring tetrahedra in order to retrieve all the cell information.

selection scheme discussed above:

$$A_{(2 \rightarrow 6)}[\mathcal{T}_j \leftarrow \mathcal{T}_i] = \min \left( 1, \frac{N_3^{(3,1)}[\mathcal{T}_i]}{2N_{60}[\mathcal{T}_j]} e^{-\Delta S_{(2 \rightarrow 6)}} \right) = \min \left( 1, \frac{N_3^{(3,1)}[\mathcal{T}_i]}{2(N_{60}[\mathcal{T}_i] + 1)} e^{5k_1 - 4k_3} \right), \quad (3.55)$$

$$A_{(6 \rightarrow 2)}[\mathcal{T}_j \leftarrow \mathcal{T}_i] = \min \left( 1, \frac{2N_{60}[\mathcal{T}_j]}{N_3^{(3,1)}[\mathcal{T}_i]} e^{-\Delta S_{(6 \rightarrow 2)}} \right) = \min \left( 1, \frac{2N_{60}[\mathcal{T}_j]}{(N_3^{(3,1)}[\mathcal{T}_j] - 4)} e^{-5k_1 + 4k_3} \right), \quad (3.56)$$

where in the second equalities we used the expressions (3.30) for the action increment, and rewrote all quantities as functions of the initial configurations ( $\mathcal{T}_i$  for the first and  $\mathcal{T}_j$  for the second), knowing that  $N_{60}[\mathcal{T}_j] = N_{60}[\mathcal{T}_i] + 1$  and  $N_3^{(3,1)}[\mathcal{T}_j] = N_3^{(3,1)}[\mathcal{T}_i] + 4$ , since in going from  $\mathcal{T}_i$  to  $\mathcal{T}_j$  we add one vertex with coordination number 6 and four tetrahedra of types (3,1)/(1,3).

## 3.4 A modification to the standard algorithm: the TBlocked algorithms

By inspecting the evolution of configurations generated by the standard algorithm in the de Sitter phase  $C_{dS}$  (see section 4.2), we observed slow modes associated to the motion of the center of volume and tails of the blob as shown in figure 3.13.

One could think, at a first look, to ignore these degrees of freedom, relegating them as mere gauge (time translations indeed), but from an algorithmic point of view we cannot tell *a priori* if these slow modes have some effect on autocorrelation times for some observables. In particular, the fluctuation in the dimension of the blob, that is the distance between tails, cannot be gauged away, and its slow evolution certainly couples with that of other blob observables.

The reason of this slowness is apparent: as described in the previous section, every move in the standard algorithm begins with the selection of some simplex from the whole set of simplices of the given kind; but, in the C phase, typical configurations present a blob-stalk structure, with the blob containing the majority of simplices, while slices in the stalk are near the minimal configuration (5 spatial pentachorons). In this way, selection of simplices is focused mainly on the bulk of the blob, making the evolution of tails and stalk much slower. We deemed it wise to not ignore this behavior.

In this section, to overcome problems related to the slow modes identified above, we will present a new family of algorithms, that differs from the standard one by the simplex selection procedure. In the following we will refer to them as the *TBlocked* algorithms.

The idea behind a TBlocked algorithm is simple: for the sake of being more ‘democratic’ on the evolution of spatial slices, we can cover the spacetime by *blocks* containing a set of adjacent slabs, in order to make first a random selection of the block and then proceed like the standard algorithm but now restricting the simplex selection to within the chosen block. This covering can be implemented in multiple ways, so we have a whole family of TBlocked algorithms, where the standard algorithm is

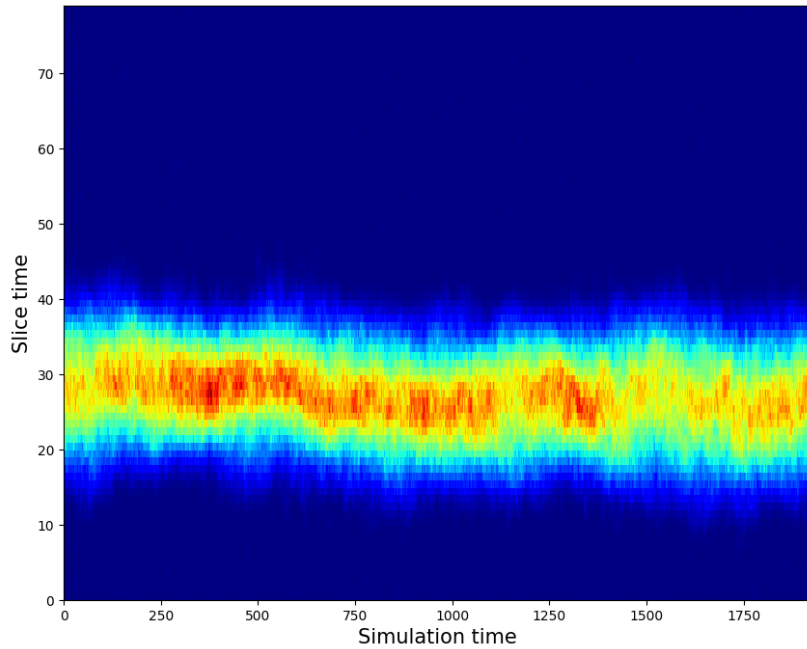


Figure 3.13: Density plot of the evolution of the distribution of spatial volume amongst slices. In the vertical axis represents the slice time, whereas the horizontal axis the simulation time.

given by the ‘single block’ cover.

Moreover, in our implementation, we imposed that nearby pairs of blocks in a cover must be overlapping for at least one slab; this because some move involves two slabs, and we require each move to be done ‘within’ at least one block.

Note that, from the point of view of spacetime volumes, this type of sampling is non-uniform, since different regions of the spacetime, namely tails and blob, are evolved with different rates. For practical reasons, we have chosen to work with blocks of fixed size and overlapping in single slabs, but the algorithm is described in the following subsection in complete generality; this restricted family of coverings can be parametrized by two integers:  $k$ , the block size, and  $\Delta t_k$ , in the range  $[0, k - 1]$ , the time shift of blocks with respect to the slice labeled 0. For a given number of spatial slices  $T$ , not every block size can be chosen for coverings of this kind; by simple algebra one can show that the block size  $k$  must satisfy the requirement  $(k - 1) \mid T$  (‘|’ reads *divide*), and the resulting number of blocks is easily computed as  $T/(k - 1)$ . A variant of the TBlocked algorithm consists to periodically in select a random shift  $\Delta t_k \in [0, k - 1]$ . This guarantees a more democratic sampling in slice-time, since slab shared by two blocks evolve faster than the other. This variant is actually the one we employ to perform numerical simulation.

### 3.4.1 Steps and detailed balance for a general TBlocked algorithm

- Start from a triangulation  $\mathcal{T}_i$  as initial configuration.

- Select a subset of simplices  $\sigma$ , from a family of subsets  $\Sigma_{\mathcal{T}_i}$  covering  $\mathcal{T}_i$ , with p.d.f.  $g_{\Sigma}^{(\mathcal{T}_i)}(\sigma)$ . (here resides the ‘local’ feature of the algorithm)
- Select a move  $m \in \mathcal{M}_{\mathcal{T}_i, \sigma}$  to try on the subset  $\sigma$  with p.d.f.  $g_{\mathcal{M}}^{(\mathcal{T}_i)}(m; \sigma)$ . ( $\mathcal{M}_{\mathcal{T}_i, \sigma}$  is really the usual set of moves  $\mathcal{M}$ )
- Select a cell  $c \in \mathcal{C}_{\mathcal{T}_i, \sigma, m} \subset \mathcal{C}(\sigma)$  with p.d.f.  $g_{\mathcal{C}}^{(\mathcal{T}_i)}(c; m, \sigma)$ .
- Compute the (tentative) new configuration  $\bar{\mathcal{T}}_j \equiv \mathcal{F}_{\sigma, m, c}(\mathcal{T}_i)$
- Proceed imposing DB as before.

Following the above steps, the full detailed balance condition reads:

$$\sum_{\{(\sigma, m, c) | \mathcal{F}_{\sigma, m, c}(\mathcal{T}_i) = \mathcal{T}_j\}} g_{\Sigma}^{(\mathcal{T}_i)}(\sigma) g_{\mathcal{M}}^{(\mathcal{T}_i)}(m; \sigma) g_{\mathcal{C}}^{(\mathcal{T}_i)}(c; m, \sigma) A[\mathcal{T}_j \leftarrow \mathcal{T}_i] \mathcal{P}[\mathcal{T}_i] \quad (3.57)$$

$$\stackrel{DB}{=} \quad (3.58)$$

$$\sum_{\{(\bar{\sigma}, \bar{m}, \bar{c}) | \mathcal{F}_{\bar{\sigma}, \bar{m}, \bar{c}}(\mathcal{T}_i) = \mathcal{T}_j\}} g_{\Sigma}^{(\mathcal{T}_j)}(\bar{\sigma}) g_{\mathcal{M}}^{(\mathcal{T}_j)}(\bar{m}; \bar{\sigma}) g_{\mathcal{C}}^{(\mathcal{T}_j)}(\bar{c}; \bar{m}, \bar{\sigma}) A[\mathcal{T}_i \leftarrow \mathcal{T}_j] \mathcal{P}[\mathcal{T}_j], \quad (3.59)$$

where  $\mathcal{F}$  is the map that transform a triangulation into another for a given choice of  $(\sigma, m, c)$ , while overlined quantities are the corresponding ‘inverse’ of non-overlined ones (for example  $\bar{c}$  is the cell associated to the move  $\bar{m}$ , inverse of  $m$ ).

As before we have some freedom in the choice of selection probabilities, but there is a crucial difference with the previous case: the transition between  $\mathcal{T}_i$  and  $\mathcal{T}_j$  is identical for a move  $m$  with associated cell  $c$  shared by two overlapping blocks  $\sigma_1$  and  $\sigma_2$  (i.e.  $\mathcal{T}_j = \mathcal{F}_{\sigma_1, m, c}(\mathcal{T}_i) = \mathcal{F}_{\sigma_2, m, c}(\mathcal{T}_i)$ ).

Then, for moves  $m$  involving a single slab cell  $c$  (like  $(3 \rightarrow 3)$ ,  $(2 \rightarrow 4)$  and inverse), and in the overlapping region between two blocks  $\sigma_1$  and  $\sigma_2$ , the contribution to the total selection probability  $G[\mathcal{T}_j \xleftarrow{m, c} \mathcal{T}_i]$  is given by the sum of two terms:

$$G_{\text{overlap}}[\mathcal{T}_j \xleftarrow{m, c} \mathcal{T}_i] = g_{\Sigma}^{(\mathcal{T}_i)}(\sigma_1) g_{\mathcal{M}}^{(\mathcal{T}_i)}(m; \sigma_1) g_{\mathcal{C}}^{(\mathcal{T}_i)}(c; m, \sigma_1) + g_{\Sigma}^{(\mathcal{T}_i)}(\sigma_2) g_{\mathcal{M}}^{(\mathcal{T}_i)}(m; \sigma_2) g_{\mathcal{C}}^{(\mathcal{T}_i)}(c; m, \sigma_2), \quad (3.60)$$

where  $\sigma_1$  and  $\sigma_2$  are the blocks satisfying  $\mathcal{T}_j = \mathcal{F}_{\sigma_1, m, c}(\mathcal{T}_i) = \mathcal{F}_{\sigma_2, m, c}(\mathcal{T}_i)$ , and  $c \in \mathcal{C}_{\mathcal{T}_i, \sigma_1, m} \equiv \mathcal{C}_{\mathcal{T}_i, \sigma_2, m}$ ; the same results apply to  $\bar{m}$  and  $\bar{c}$ , because we put  $\bar{\sigma} = \sigma$  for each  $\sigma$ .

For moves  $m$  and associated cells  $c$  in a block  $\sigma$ , non-overlapping with any other block, the selection probability has a single term, like the standard case:

$$G_{\text{non-overlap}}[\mathcal{T}_j \xleftarrow{m, c} \mathcal{T}_i] = g_{\Sigma}^{(\mathcal{T}_i)}(\sigma) g_{\mathcal{M}}^{(\mathcal{T}_i)}(m; \sigma) g_{\mathcal{C}}^{(\mathcal{T}_i)}(c; m, \sigma), \quad (3.61)$$

because there exists only a triple  $(\sigma, m, c)$  satisfying  $\mathcal{T}_j = \mathcal{F}_{\sigma, m, c}(\mathcal{T}_i)$ .

We can simplify further the detailed balance condition by making the move selection independent of the block chosen, and equal for dual moves:

$$g_{\mathcal{M}}^{(\mathcal{T})}(m; \sigma) = g_{\mathcal{M}}^{(\bar{\mathcal{T}})}(\bar{m}; \sigma), \text{ for each } \bar{\mathcal{T}} \in \{\mathcal{F}_{\sigma, m, c}(\mathcal{T}) | \sigma \in \Sigma_{\mathcal{T}}, c \in \mathcal{C}_{\mathcal{T}, \sigma, m}\}. \quad (3.62)$$

Block selection probabilities  $g_\Sigma$  can be made constant (uniform extraction of the block), so to not enter the detailed balance condition.

In this way, as for the standard algorithm, we have the simplified detailed balance condition for each move type; for a move  $m$  and cell  $c \in \sigma$  without overlaps one must use the form:

$$A[\mathcal{T}_j \leftarrow \mathcal{T}_i] = \min \left( 1, \frac{g_c^{(\mathcal{T}_j)}(\bar{c}; \bar{m}, \sigma) \mathcal{P}[\mathcal{T}_j]}{g_c^{(\mathcal{T}_i)}(c; m, \sigma) \mathcal{P}[\mathcal{T}_i]} \right), \quad (3.63)$$

$$A[\mathcal{T}_i \leftarrow \mathcal{T}_j] = \min \left( 1, \frac{g_c^{(\mathcal{T}_i)}(c; m, \sigma) \mathcal{P}[\mathcal{T}_i]}{g_c^{(\mathcal{T}_j)}(\bar{c}; \bar{m}, \sigma) \mathcal{P}[\mathcal{T}_j]} \right), \quad (3.64)$$

For a move  $m$  and cell  $c \in \sigma_1 \cap \sigma_2$  between overlapping blocks must use:

$$A[\mathcal{T}_j \leftarrow \mathcal{T}_i] = \min \left( 1, \frac{g_c^{(\mathcal{T}_j)}(\bar{c}; \bar{m}, \sigma_1) + g_c^{(\mathcal{T}_j)}(\bar{c}; \bar{m}, \sigma_2) \mathcal{P}[\mathcal{T}_j]}{g_c^{(\mathcal{T}_i)}(c; m, \sigma_1) + g_c^{(\mathcal{T}_i)}(c; m, \sigma_2) \mathcal{P}[\mathcal{T}_i]} \right), \quad (3.65)$$

$$A[\mathcal{T}_i \leftarrow \mathcal{T}_j] = \min \left( 1, \frac{g_c^{(\mathcal{T}_i)}(c; m, \sigma_1) + g_c^{(\mathcal{T}_i)}(c; m, \sigma_2) \mathcal{P}[\mathcal{T}_i]}{g_c^{(\mathcal{T}_j)}(\bar{c}; \bar{m}, \sigma_1) + g_c^{(\mathcal{T}_j)}(\bar{c}; \bar{m}, \sigma_2) \mathcal{P}[\mathcal{T}_j]} \right). \quad (3.66)$$

Cell selection probabilities  $g_c$  must be computed as explained before in the standard case, but counting only cells contained in the block (or blocks) of interest.

### 3.4.2 Further generalizations and applications

In section 4.3 we tested our implementation of the TBlocked algorithm against the standard one. We anticipate that the results from simulations did not show significant differences between the two algorithms. This fact should not be discouraging though, since, with further implementative effort, our TBlocked algorithm could be easily parallelized by allocating the data structures of different blocks to different processors, and therefore evolving different regions of the triangulation faster. Note however, that the updating of the blocks boundaries affects the adjacent blocks, and information between processors should therefore be properly transmitted whenever one of this edge cases occurs. In particular, it is not convenient to distribute the *workload* to many small blocks, since in that case each processor would wait more frequently the data transmitted from other processors, instead of effectively doing work. In general, one tries to find the best compromise between work and transmissions, so there will be an optimal size for the blocks, that perform overall better on updating configurations.

Parallel programming is used nowadays for many purposes, from scientific to non-scientific. Many Monte-Carlo simulations of physical systems (like QCD) are today implemented in a parallel fashion, in order to exploit the distribution of workload between processors or even graphical processing units (GPUs). In the case of CDT, the task of parallelizing the standard code is difficult, since the information about neighbouring simplices is extremely delocalized in the data structures employed (see appendix A), and many parallel programming paradigms and hardwares<sup>14</sup> exploit instead the simultaneous access to contiguous data. A parallelized TBlocked algorithm would suffer anyway from the delocalization of local information inside blocks, but it could allow to make a step forward towards efficient simulations in CDT.

---

<sup>14</sup>In particular GPUs, that were originally designed to access data about pixels.

# Chapter 4

## Simulation results

In every branch of science it is a good practice to *reproduce* and *verify* standard results before embarking in further development.

In this chapter we will perform various tests for our implementations of the standard and TBlocked algorithms. First of all we will check if our implementation of the standard algorithm does reproduce correctly the phase diagram presented by Ambjorn et al. [4], then we will analyze in detail the most interesting phase (called after De Sitter), and discuss some observable one can define for it and its physical interpretation. Finally we show that TBlocked algorithms give results compatible with the standard one, and discuss its efficiency and implications.

All simulations have been conducted in the computing farm of the INFN-Pisa section.

### 4.1 Phase diagram

As anticipated in section 2.5.1, from numerical simulations of 4-dimensional CDT with topology  $S^1 \times S^3$ , four distinct phases have been observed, called  $A$ ,  $B$ ,  $C_{ds}$  and  $C_b$ . However, since it has been only recently discovered, we will not go into details about the last phase  $C_b$ , called the *bifurcation* phase, and will discuss only the  $B|C_b$  and  $A|C_{ds}$  phase transitions. The phases  $C_{ds}$  and  $C_b$  differ by the presence of singular vertices of very high coordination number at microscopic level, but the large scale distribution of spatial volumes over the slices appears to be very similar, so we will occasionally refer to any of them as  $C$  phase.

The phase diagram of CDT is represented in figure 4.1. In the following we will present a brief overview of the phases and transitions lines; for more information about standard results see ref. [4].

#### 4.1.1 Spatial volume distribution in the different phases

The simplest observable that can be used to characterize the large scale structure of universes is the spatial volume per slice. For a slice with time label  $t \in \{0, \dots, T-1\}$  the spatial volume is equal to the number of spatial tetrahedra on that slice and will be denoted by  $N_{3s}(t)$ . We recall that *time* here is not the usual time we are familiar with, but is the result of a Wick-rotation to an Euclidean space.

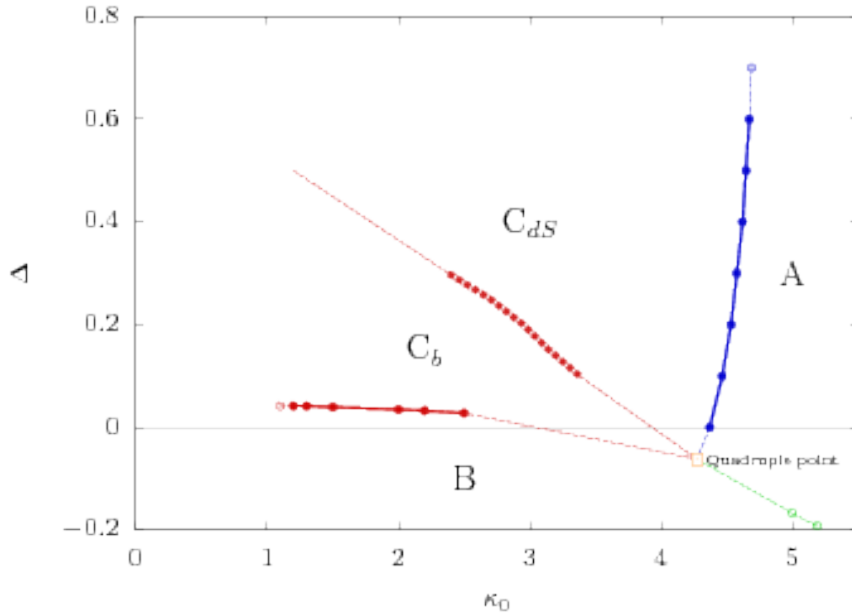


Figure 4.1: Current state of the phase diagram of CDT. Taken from [9].

The spatial volume distribution, however, does not encode information about the underlying geometry of slices and slabs, so must be understood merely as a “profile” of the universe.

More geometrically descriptive observables will be discussed in chapter 5.

### A phase

The *A* phase is characterized by an apparently random distribution of spatial volumes over slices, as the one depicted in figure 4.2.

It does not seem particularly interesting from the physical point of view , since it corresponds to multiple uncorrelated and short-living universes, not the one we observe in nature.

### B phase

The spatial volume of typical configurations in the *B* phase is mostly concentrated on a single slice as shown in figure 4.3:  $N_{3s}(t) = N_{3s}[\mathcal{T}] \delta_{t,t_c}$ . The universe in this phase then exists only for an instant, during which it is purely spatial; the time translation symmetry breaks completely, and the universe becomes effectively Euclidean with topology  $S^3$ .

The few vertices in the slices neighbouring to the one at  $t_c$  have a large coordination number, and the majority of pentachorons are of types (4, 1) and (1, 4), so that one expects that the most accepted move in the Monte-Carlo updating are  $(2 \rightarrow 8)$  and  $(8 \rightarrow 2)$ .

### C phases

Both the  $C_{dS}$  and  $C_b$  phases have very similar spatial volume distributions, and that is probably the main reason why the differences between them were not detected until recently.

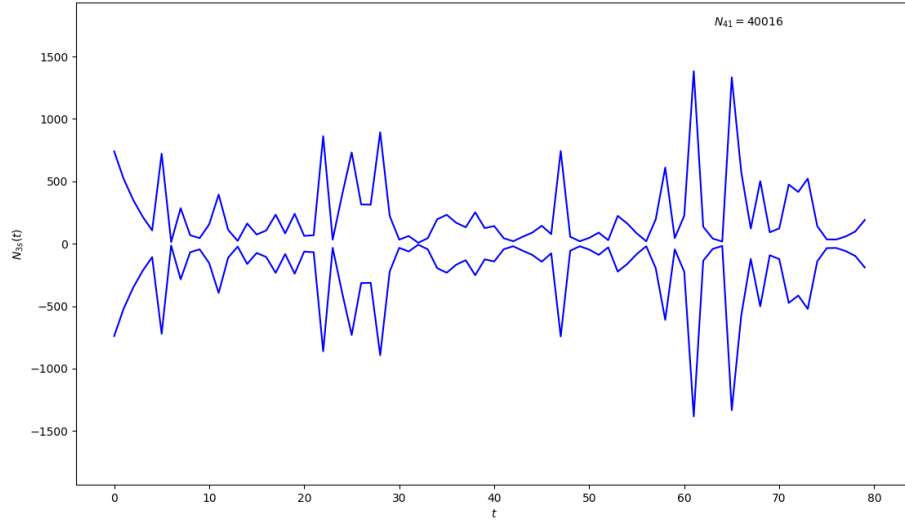


Figure 4.2: Screenshot of the spatial volume profile of a universe with spatial volume fluctuating around  $V = \frac{N_4^{(4,1)}}{2} = 20k$ , and fully inside the  $A$  phase:  $(k_0 = 5.2, \Delta = 0.6)$ . The line below has been introduced only for visualization purposes.

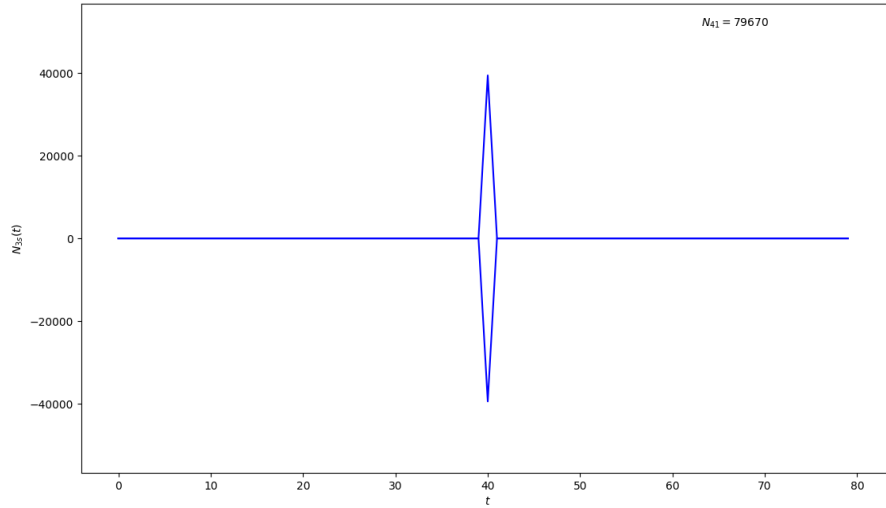


Figure 4.3: Screenshot of the spatial volume profile of a universe with spatial volume fluctuating around  $V = \frac{N_4^{(4,1)}}{2} = 40k$  and fully inside the  $B$  phase:  $(k_0 = 2.2, \Delta = 0.2)$ . The line below has been introduced only for visualization purposes.

Universes in the  $C$  phases are the most interesting physically, since their spatial volume distribution is extended in time, and in particular it has a characteristic structure made of a “blob”, where most of the spatial and spacetime volumes are localized, two “tails” where the volume rapidly decrease, and a “stalk” where the minimal spatial volume is attained except for sparse fluctuations (see figure 4.4). The emergent structure seems that of a ball on a thin ring; indeed, in section 4.2, we will discuss the remarkable result that the spatial volume distribution per slice of the blob fits well with the one of a de Sitter universe.

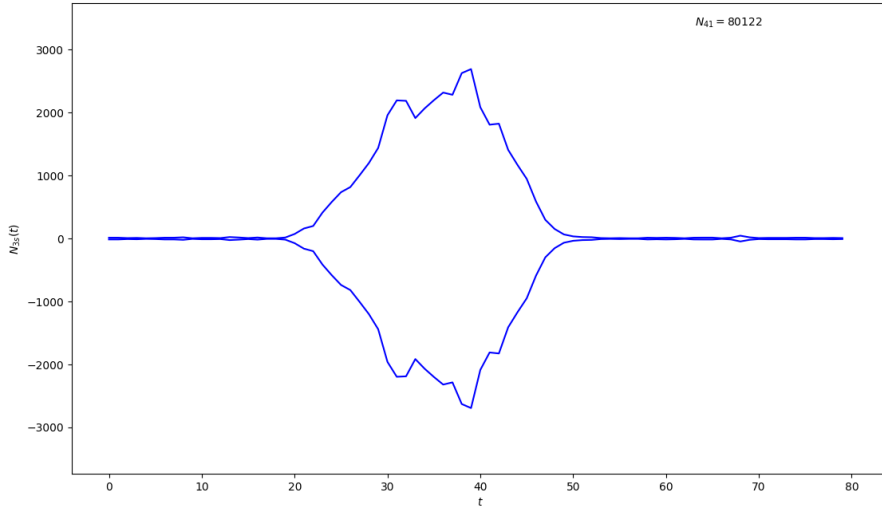


Figure 4.4: Screenshot of the spatial volume profile of a universe with spatial volume fluctuating around  $V = \frac{N_4^{(4,1)}}{2} = 40k$  and fully inside the  $C_{dS}$  phase: ( $k_0 = 2.2$ ,  $\Delta = 0.6$ ). The line below has been introduced only for visualization purposes.

### 4.1.2 Validation of the phase diagram

To verify that the phase diagram obtained from our implementation is consistent with the one found in the literature it is sufficient to investigate the behavior of the order parameters (defined soon) across and near few critical points on the  $A|C_{dS}$  and  $B|C_b$  phases, since the position of critical points is very sensitive, and could be drastically different if some error in the code implementation occurs. In particular, we want to verify that simulations with parameters  $(k_{0c}, \Delta_c)$ , corresponding to some critical point well known in literature, does exhibit the characteristic behaviour for the order parameter, that is a double peak distribution. Indeed any transition at finite volume is signalled by a fluctuation in the order parameter between the different values it takes on the two sides of the transition line.

#### AC transition

The  $A|C_{dS}$  transition line occurs for values of  $k_0$  approximately constant with respect to changes in  $\Delta$ , so it is reasonable to employ the free tunable parameter  $k_0$  itself (analogue to the temperature or magnetic field for ferromagnetic transitions), keeping  $\Delta$  constant.

In practice, one performs many independent simulations at different values of  $k_0$  and at a fixed value of  $\Delta$  so to create a “line of simulations” crossing the  $A|C_{dS}$  transition line.

The order parameter used to signal the  $A|C_{dS}$  transition is

$$\text{conj}(k_0) \equiv \frac{N_0}{N_4}, \quad (4.1)$$

where the dependence on the triangulation  $\mathcal{T}$  is understood. The observable  $\text{conj}(k_0)$  is *conjugate*<sup>1</sup> to  $k_0$ , that is the term multiplying the parameter  $k_0$  in the action (2.27),

---

<sup>1</sup>It is a common practice in the analysis of critical system to employ conjugate observables

normalized by the spacetime volume  $N_4$ .

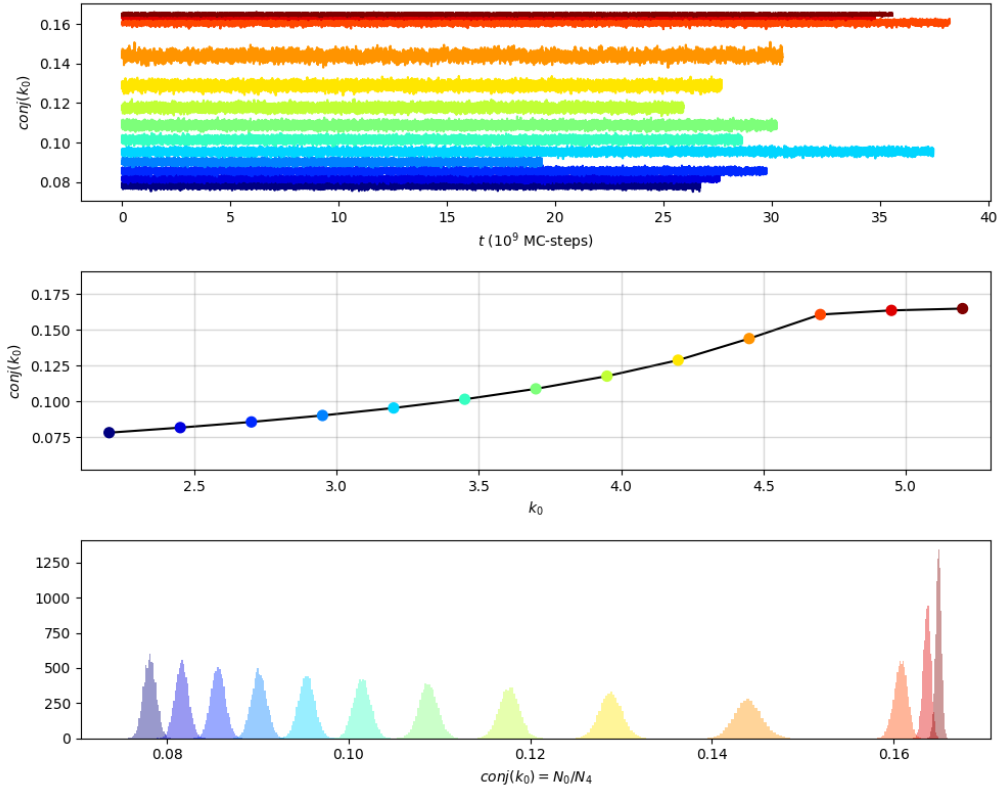


Figure 4.5: Plots of the order parameter  $\text{conj}(k_0)$  along the “line of simulations”:  $k_0 \in [2.2, 5.2]$ ,  $\Delta = 0.6$ . All simulations are independent and with fixed total spacetime volume  $N_4 = 40k$ , and  $T = 80$  slices.

[top panel]: histories of the order parameter in simulation time.

[intermediate panel]: averages of the order parameter for different values of  $k_0$ ; the errors on the averages are thinner than the black line.

[bottom panel]: histograms of the order parameter for different values of  $k_0$ .

In figure 4.5 is depicted the behaviour of  $\langle \text{conj}(k_0) \rangle$  along a line of simulations at  $\Delta = 0.6$  and with  $k_0$  ranging in the interval  $[2.2, 5.2]$ .

The order parameter  $\text{conj}(k_0)$  seems to be distributed unimodally<sup>2</sup> with average continuously increasing for increasing values of  $k_0$ , until it reaches a plateau for values above  $k_0 \simeq 4.7$ .

However, this continuity and unimodality is no more valid near the crossing point of the transition line. To see this behaviour the free parameter  $k_0$  must be fine-tuned to a specific value, for which the order parameter shows a bimodal distribution; for  $\Delta = 0.6$  and a fixed spacetime volume  $N_4 = 120k$ , the value sought corresponds to the standard result  $k_0 \simeq 0.4711$ , as shown in figure 4.6.

The two peaks indicate that the configurations oscillate, in Monte Carlo time, between metastable states resembling alternatively phase  $C_{ds}$  (left peak) or phase

---

as order parameters. In ferromagnetic systems, for example, the magnetization is the observable conjugate to the magnetic field, and is used as order parameter.

<sup>2</sup>Unimodality of a distribution means the presence of a single local maximum; conversely the term bimodal usually indicates a distribution with two local maxima.

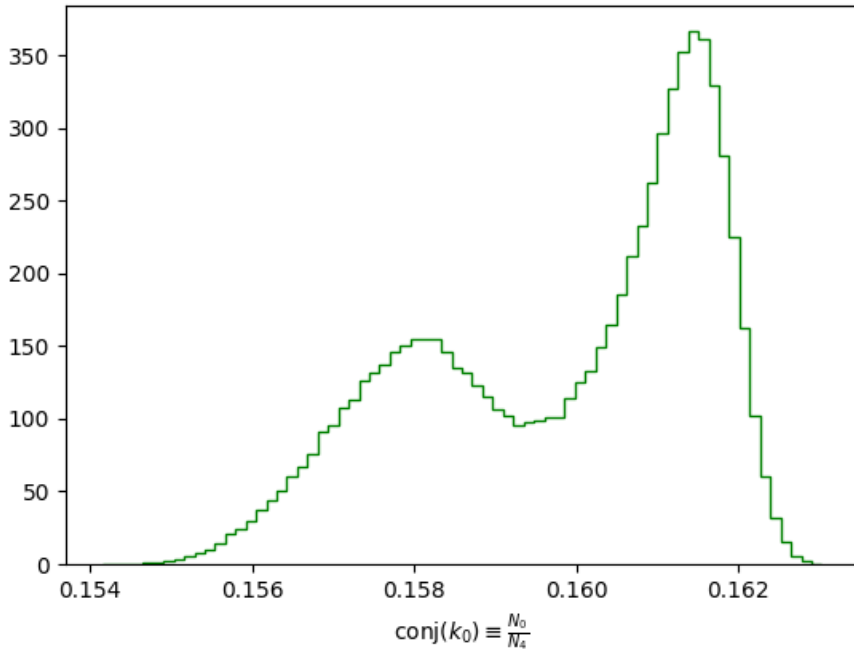


Figure 4.6: Histogram of the order parameter for a simulation at the critical point ( $k_0 \simeq 0.4711, \Delta = 0.6$ ) and spacetime volume  $N_4 = 120k$ .

$A$  (right peak).

We must remember, however, that these results are obtained for a single finite volume, and to infer the order of the transition one should perform many simulations for increasing volumes and extrapolate the behaviour: if the peaks come closer and the throat between them tends to disappear for diverging volumes, we can talk of a continuous transition<sup>3</sup>; on the converse, if the peaks become distinctly separated the order parameter will “jump” over a discontinuity while crossing the transition line, and the transition will be called discontinuous or first order.

The analyses performed by the group of Ambjörn et al. [4] for many volumes and at different values of  $\Delta$ , points toward an AC transition of discontinuous order.

## BC transition

Observing that the  $B|C_b$  transition line seems to occur for an almost constant value of the parameter  $\Delta$ , one can proceed in analogy with the  $A|C_{dS}$  line case by performing a “line of simulations” crossing the  $B|C_b$  line varying  $\Delta$  and keeping constant  $k_0$ .

Like for the  $A|C_{dS}$  transition it is useful to employ as order parameter the observable conjugate (up to a constant) to the action parameter  $\Delta$ , that is varied in

---

<sup>3</sup>To be precise, the merging of the peaks for increasing volumes is not sufficient to claim that a transition is continuous, since no transition could occur at all. The divergence of correlation lengths or susceptibilities should also be observed.

order to cross the transition line:

$$\text{conj}(\Delta) \equiv \frac{N_4^{(4,1)} - 6N_0}{N_4}, \quad (4.2)$$

where the dependence on the triangulation  $\mathcal{T}$  is understood. Here the behaviour

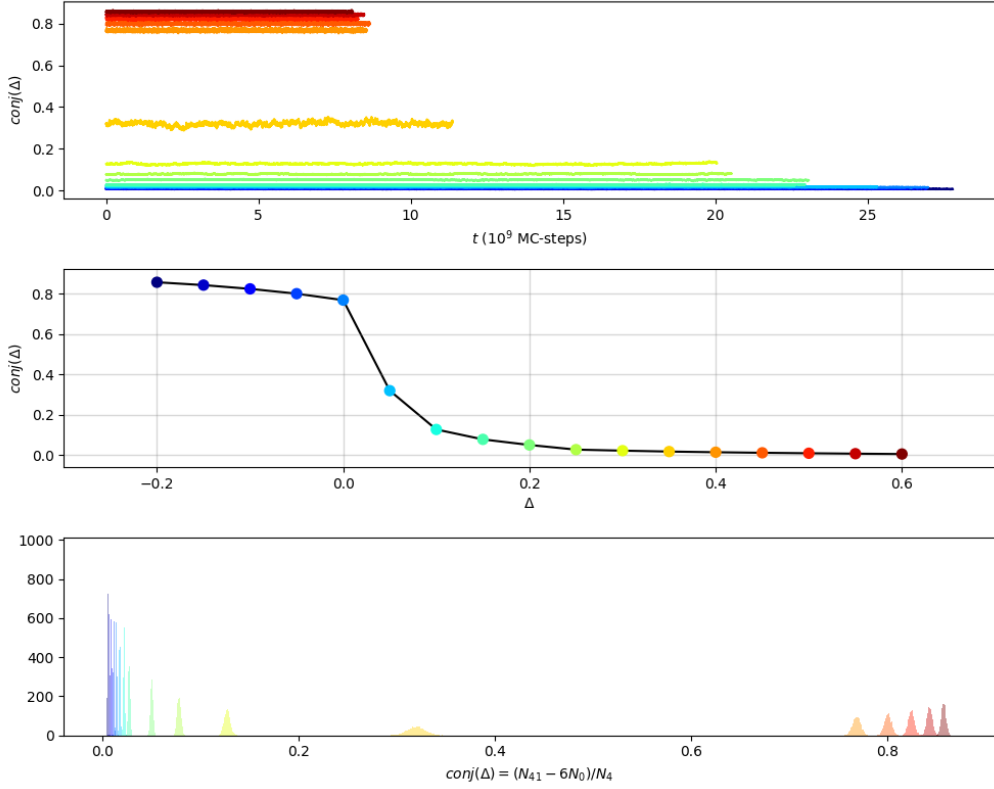


Figure 4.7: Plots of the order parameter  $\text{conj}(\Delta)$  along the “line of simulations”:  $k_0 = 2.2$ ,  $\Delta \in [-0.2, 0.6]$ . All simulations are independent and with fixed total spatial volume  $\frac{N_4^{(4,1)}}{2} = \frac{80k}{2}$ , and  $T = 80$  slices.

[top panel]: histories of the order parameter in simulation time.

[intermediate panel]: averages of the order parameter for different values of  $\Delta$ ; the errors on the averages are thinner than the black line.

[bottom panel]: histograms of the order parameter for different values of  $\Delta$ .

of the order parameter suggests that in the  $C$  phases, there are on average slightly more than 6 pentachorons of types  $(4, 1)$  or  $(1, 4)$  per vertex ( $N_4^{(4,1)} \simeq 6N_0$ ), whereas going towards the  $B$  phase keeping fixed the spatial volume ( $N_{3s} = \frac{N_4^{(4,1)}}{2}$ ) the number of vertices drops to a few vertices with high coordination number.

This behaviour has to be expected, since the whole spatial volume of typical configurations in the  $B$  phase is distributed on a single slice, and the few vertices on the adjacent slices must be owned by the large number of  $(4, 1)$  or  $(1, 4)$  tetrahedra contained in the slabs between them.

Here the order parameter  $\text{conj}(\Delta)$  signals a phase transition for  $\Delta \simeq 0$ , but in fact there is a hidden transition between phases  $C_b$  and  $C_{dS}$  at  $\Delta \simeq 0.4$ , where a suitable order parameter will be defined in eq. (4.3).

Figure 4.8 shows the histogram of the order parameter  $\text{conj}(\Delta)$  for a simulation

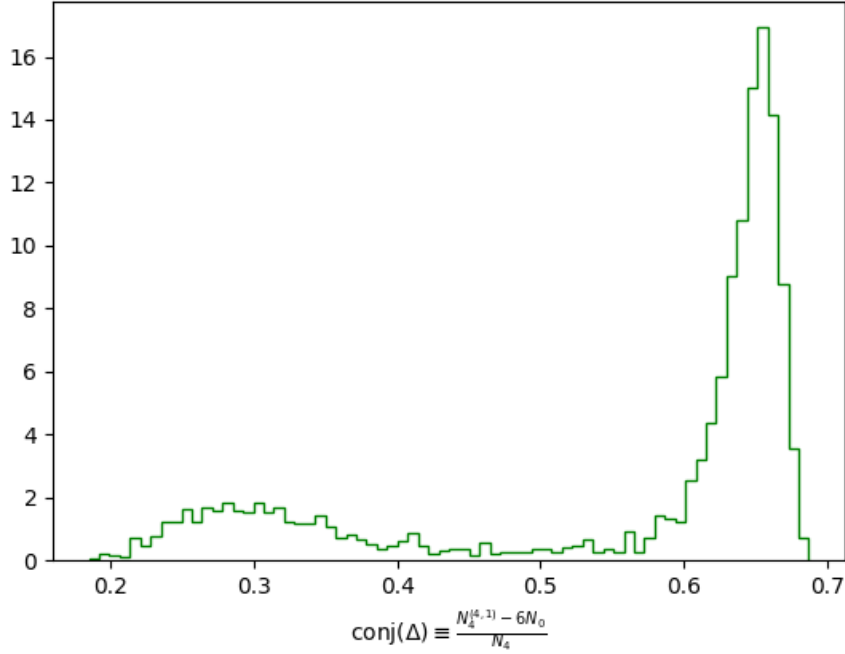


Figure 4.8: Histogram of the order parameter  $\text{conj}(\Delta)$  for a simulation at ( $k_0 = 2.2$  and  $\Delta = 0.022$ ) and  $N_4 = 40k$ . Although small, the throat indicates that the order parameters can oscillate between two values, signalling the transition.

with  $k_0 = 2.2$ , and  $\Delta \simeq 0.022$  fine-tuned in order to get the characteristic bimodal distribution.

While the two peaks seems far and the throat tiny at the chosen spatial volume, a careful extrapolation of the behaviour for increasing volumes ([4]) shows that the peaks come closer and the throat wider, so the transition is probably second order.

### CC transition

In this thesis we have not performed an analysis of the  $C_{dS}|C_b$  transition. For completeness, however, we will describe briefly the definition of the ordered parameter, and the breaking of the symmetry involved.

The blob of a typical triangulation in the  $C_b$  phase contains slices which, for alternating time labels (all even or all odd), are characterized by the presence of isolated vertices with high coordination number. The volume clusters forming a slab near one of these vertices seems to have a structure similar to half of the structure of a typical configuration in the  $B$  phase<sup>4</sup>.

The definition of the order parameter employed in literature [9], even if in a somewhat ad-hoc manner, does encode this alternated property of slices:

$$\text{OP}_2 = \frac{1}{2} \left[ \left| O_{\max}(t_0) - O_{\max}(t_0 + 1) \right| + \left| O_{\max}(t_0) - O_{\max}(t_0 - 1) \right| \right], \quad (4.3)$$

<sup>4</sup>This fact is reasonable, since  $B$  and  $C_b$  phases are adjacent in the phase diagram, and the transition is believed to be of continuous order.

where  $O_{max}(t)$  is the highest coordination number for vertices in the slice  $t$ , and  $t_0$  is the slice label maximizing  $O_{max}$  amongst slices, that is  $O_{max}(t_0) = \max_t O_{max}(t)$ . So, eq. (4.3) is, in words, an average of the differences between the highest coordination number amongst vertices in the triangulation and the next-to-highest coordination numbers for vertices in the neighbouring slices<sup>5</sup>.

The distribution of spatial volume per time slice  $N_{3s}(t)$  is very much similar between the  $C_{ds}$  and  $C_b$  phases, but the internal structure of the latter shows a breaking of the translational time symmetry in the form of the even/odd slice structure discussed above.

At the time of writing, the  $C_b|C_{ds}$  transition is being currently investigated, but preliminary results [9] seems to point toward a continuous transition. If that is the case, a critical point on this line could actually be the one allowing the continuum limit to a non-perturbative theory of quantum gravity.

## 4.2 De Sitter phase

Probably, the most interesting result of CDT is the emergence of a dynamical background geometry with extended time distribution of volume (phase  $C$ ), from a background independent approach. Furthermore, this geometry seems to fit well with the one predicted by the current best model of the universe dominated by the cosmological constant (dark-energy), namely the *de Sitter universe*.

Here we will discuss more about the  $C_{ds}$  phase and some of the analysis one could perform specifically for it.

### 4.2.1 Profile of the universe

First of all notice that, during the simulation time, the blob structure of the triangulations in the  $C_{ds}$  phase perform a slow random-walk in slice time; so, having in mind to statistically “merge” information about different configurations in the sample, we need first to define the concept of *center of volume* and *align* their profiles  $\{N_{3s}[\mathcal{T}_i](t)\}$  with respect to it. This procedure is legitimate, since the theory is invariant with respect to time translations.

Since, in the configurations studied, the time direction has the topology of an  $S^1$ , there are many ways to define the center of volume<sup>6</sup>, each differing by no much than a slice-time step.

---

<sup>5</sup>Unlike the other order parameters, it is not a global quantity.

<sup>6</sup>In our analysis we chose the following definition:

$$t_{CV} = \left[ T \cdot \frac{1}{2\pi} \arg \left( \sum_{t=0}^{T-1} N_{3s}(t) e^{2\pi i t/T} \right) \right], \quad (4.4)$$

where  $[ \cdot ]$  is the nearest integer function,  $T$  is the number of slices, and  $\arg(\cdot)$  is the phase of the complex number inside parenthesis (in the range  $[0, 2\pi]$ ). Since a circle  $S^1$  can be represented by complex numbers with unit absolute value, we found natural to employ this definition, which represents a weighted average of the phases. We warn, however, that this is not the standard definition used in [4].

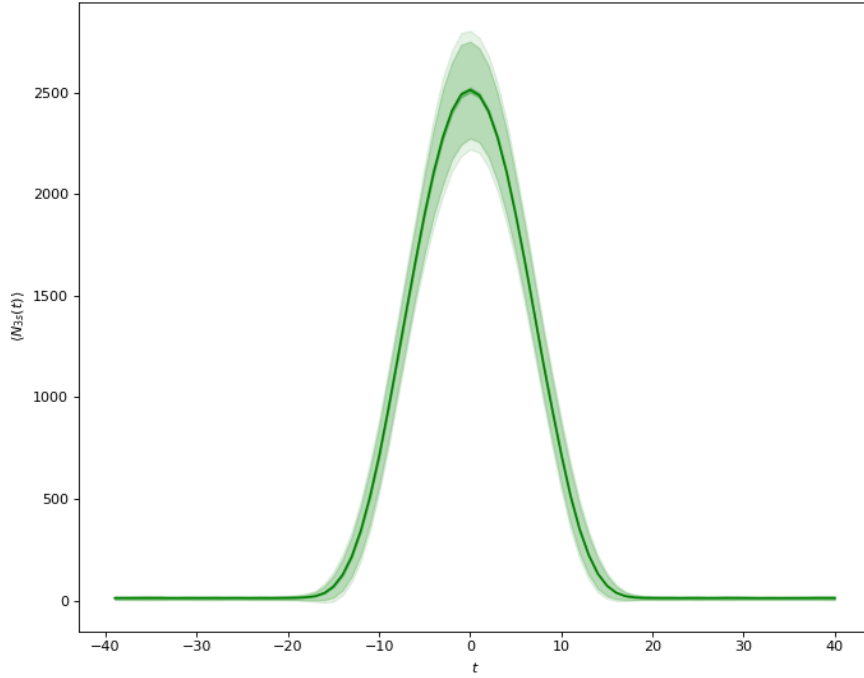


Figure 4.9: Average and fluctuations for a simulation in the de Sitter phase (details in the text).

Denoting by  $t_{0,i}$  the center of volume of the  $i$ -th configuration  $\mathcal{T}_i$ , whatever definition has been used, the spatial volume distribution must be aligned by the formula

$$N_{3s}^{\text{al}}[\mathcal{T}_i](t) \equiv N_{3s}^{\text{new}}[\mathcal{T}_i]((t - t_{0,i}) \bmod T), \quad (4.5)$$

where  $T$  is the number of slices.

We can then make an average of these aligned spatial volume distributions to obtain the average volume:

$$V_s(t) \equiv \langle N_{3s}^{\text{al}}(t) \rangle = \frac{1}{M} \sum_{i=1}^M N_{3s}^{\text{al}}[\mathcal{T}_i](t), \quad (4.6)$$

where  $M$  is the number of configurations in the sample  $\{\mathcal{T}_i\}$ .

Similarly, fluctuations  $\Delta V_s(t)$  of the spatial volume at a time  $t$  can be computed as the square root of the variance estimated from the sample  $\{N_{3s}^{\text{al}}[\mathcal{T}_i](t)\}_{i=1}^M$ :

$$(\Delta V_s)^2(t) \equiv \langle [N_{3s}^{\text{al}}(t) - V_s(t)]^2 \rangle = \frac{1}{M-1} \sum_{i=1}^M (N_{3s}^{\text{al}}[\mathcal{T}_i](t) - V_s(t))^2. \quad (4.7)$$

Figure 4.9 shows the result of a simulation with total spatial volume fixed by  $N_4^{(4,1)} = 80k$ , and well inside the de Sitter phase. The dark green line represents the average volumes  $V_s(t)$  per (aligned) slice time  $t$ , while the innermost light green halo represents the size of fluctuations  $\Delta V_s(t)$ ; the outermost halo represents the errors<sup>7</sup>

<sup>7</sup>Errors on the average and standard deviation are estimated by using the Bootstrap resampling method.

in the fluctuation computation, while the errors on the average volume are hidden by the dark green curve.

Even if the profile of typical configurations in the de Sitter phase appears to be disordered and show no particular symmetry (recall figure 4.4), the averaged spatial volume of the blobs results to be smoothly distributed in the extended time range, and clearly symmetric with respect to the center of volume. Indeed, the emergence of a background geometry must be intended in an *averaged* sense, since the theory is quantum mechanical. If a critical point allowing the continuum limit can be found in the de Sitter phase, we would expect that for increasing volumes the average volume tends toward a classical solution of the Einstein's equations, whereas fluctuations, probably at the Planckian scale, encode the quantum nature of spacetimes.

The continuum limit has not been found yet (even if one hopes on the  $C_b|C_{ds}$  transition), but the averaged volume  $V_s(t)$  obtained can be fitted with a well-known solution of the Einstein's equations, namely the de Sitter universe [17].

A 4-dimensional de Sitter universe in Lorentzian spacetime can be parametrized by variables  $\{x_0, x_1, x_2, x_3, x_4\}$  satisfying the constraint

$$-x_0^2 + x_1^2 + x_2^2 + x_3^2 + x_4^2 = R^2, \quad (4.8)$$

where  $R$  is called the *de Sitter radius*.

However, in a Wick-rotated (euclidean) space the de Sitter universe has the geometry of a sphere  $S^4$ , since the minus sign in eq. (4.8) is flipped.

To compare our average volume with the de Sitter model, it is sufficient to get the expected distribution of spatial volumes for slices with constant  $x_0$  (in the Euclidean setting).

Our data represents reasonably well the distribution from this model, where the total spatial volume of a triangulation is  $N_{3s} = \frac{N_4^{(4,1)}}{2}$ , and neglecting contributions from the stalk, elementary calculus shows that using the  $S^4$  model, the correct expression for the distribution of spatial volume on the blob is (see [14])

$$V_s^{(dS)}(t) = \frac{N_4^{(4,1)}}{2} \frac{3}{4} \frac{1}{\omega(N_4^{(4,1)})^{\frac{1}{4}}} \cos^3 \left( \frac{t}{\omega(N_4^{(4,1)})^{\frac{1}{4}}} \right), \quad (4.9)$$

where  $\omega$  is an appropriate constant encoding the spread, in slice-time, of the volume distribution.

## 4.2.2 Spectral dimension

The spatial volume distribution is only an effective variable, and is certainly not sufficient to characterize the geometry of triangulations. For this reason, one needs other observables. Useful information for the geometry in the de Sitter phase is given by the *fractal dimensions*.

Here we will define and discuss the *spectral dimension*; results about another definition of dimension employed in literature, called the *Hausdorff dimension*, can be found in [4, 18].

Let us consider a diffusion process on the triangulation, where an ensemble of random walkers can jump from one pentachoron to anyone of the adjacent pentachorons with uniform probability.

In a smooth manifold this process can be described by the fundamental solution to the heat equation:

$$\begin{cases} \frac{\partial K}{\partial \tau}(\vec{x}, \vec{x}_0; \tau) = \nabla_{\vec{x}}^2 K(\vec{x}, \vec{x}_0, \tau), \\ K(\vec{x}, \vec{x}_0; 0) = \delta(\vec{x} - \vec{x}_0), \end{cases} \quad (4.10)$$

where  $K(\vec{x}, \vec{x}_0; \tau)d\vec{x}$  is the probability that a random walker starting at  $\vec{x}_0$  is found in the volume element  $(\vec{x}, d\vec{x})$  at time  $\tau$ , and  $\nabla_x^2$  is the Laplace-Beltrami operator acting on the  $\vec{x}$  variable only.

Discretizing eq. (4.10), we obtain the expression that has to be used for causal triangulations<sup>8</sup>

$$K(p, p_0; \tau + 1) = (1 - \eta)K(p, p_0; \tau) + \eta \cdot \frac{1}{5} \sum_{p' \in \mathcal{N}(p)} K(p', p_0; \tau), \quad (4.11)$$

where  $p_0$  is the label of the pentachoron from which random walks starts,  $\mathcal{N}(p)$  indicates the set of labels of pentachorons adjacent to  $p$ , whereas  $\eta$  is an arbitrary parameter that depends on the way we discretize the time and space directions, and will be referred to as *rate factor*<sup>9</sup>. Unlike the continuous case in eq. (4.10), where  $K(\vec{x}, \vec{x}_0; \tau)$  was a probability density and  $\tau$  was continuous, here  $K(p, p_0; \tau)$  is a probability and  $\tau$  is an integer which indicates the number of steps of the discrete random walk.

The *return probability* at  $p_0$  for the diffusion process in eq. 4.11 is defined as the probability that a random walker comes back to the starting point  $p_0$  at a diffusion time  $\tau$ , that is

$$Z(\tau; p_0, \mathcal{T}) \equiv K(p_0, p_0, \mathcal{T}; \tau), \quad (4.12)$$

where we made explicit the dependence on the triangulation  $\mathcal{T}$  in which the diffusion processes take place.

Averaging over the starting points we obtain an estimate of the mean return probability on a configuration, and averaging again through sampled configurations  $\{\mathcal{T}_i\}_{i=1}^n$  we get the quantum averaged return probability<sup>10</sup>

$$Z(\tau) = \frac{1}{n} \sum_{i=1}^n \frac{1}{N_4[\mathcal{T}_i]} \sum_{p_0 \in \mathcal{T}_i} Z(\tau; p_0, \mathcal{T}_i). \quad (4.13)$$

A standard result from diffusion processes on fractal structures is that the return probability typically follows a law of the type

$$Z(\tau) = \tau^{-\frac{D_S}{2}} \Phi(\tau), \quad (4.14)$$

---

<sup>8</sup>Here random walkers are allowed to not follow causal laws, since are used merely to probe the fractal structure of triangulations and have no physical meaning.

<sup>9</sup>The smaller the rate factor the slower is, the longer the diffusion process takes to evolve at each iteration, then resulting in a smoother diffusion.

<sup>10</sup>In practice only a finite number of starting pentachorons, proportional to the total volume, are randomly selected to get sufficiently accurate estimates. Furthermore, to prevent the diffusion processes from starting occasionally on the stalk or tails, the starting pentachorons are randomly selected in the two slabs adjacent the slice with maximum spatial volume.

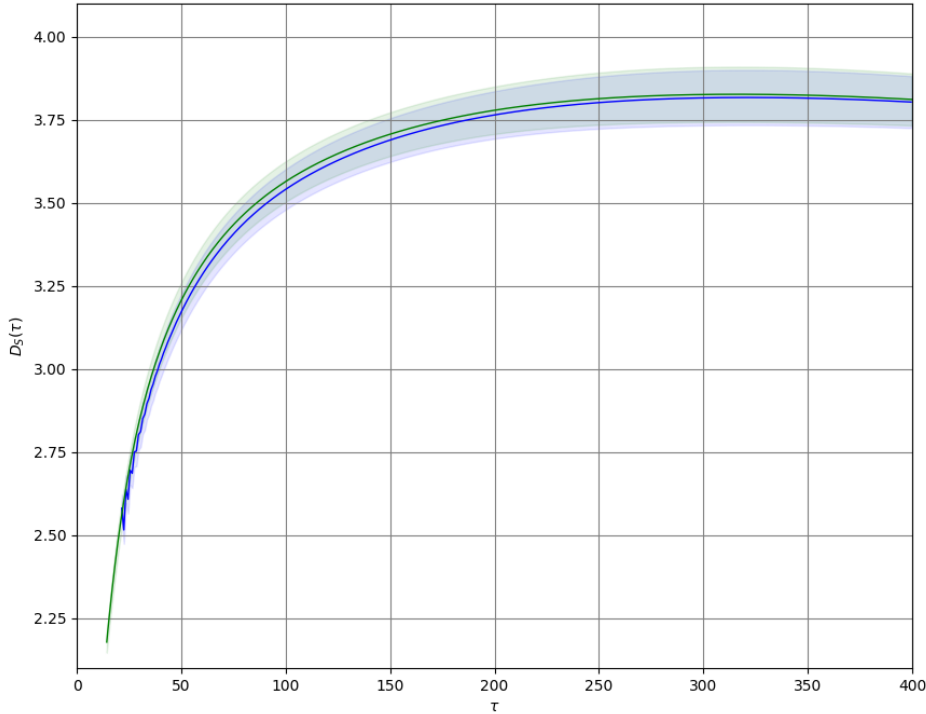


Figure 4.10: Spectral dimension computed from diffusion processes on de Sitter configurations with spatial volume fixing  $N_4^{(4,1)} = 80k$ , and for two different rate factors:  $\eta = 1$  (blue line),  $\eta = \frac{2}{3}$  (green line). Errors estimate with a jackknife resampling method.

where  $\Phi(\tau)$  is a function nearly constant in a certain diffusion-time range  $[\tau_1, \tau_2]$ , and  $D_S$  is called the *spectral dimension* of the fractal structure.

Using eq. (4.14), we can write the expression of the spectral dimension

$$D_S(\tau) = -2 \frac{d \log Z(\tau)}{d \log \tau} + \dots, \quad (4.15)$$

where the  $\tau$ -dependence of  $D_S$  has been made explicit, and “ $\dots$ ” indicates correction terms, negligible in the range  $[\tau_1, \tau_2]$ .

In standard CDT literature the diffusion process in eq. (4.11) is implemented with a rate factor  $\eta = 1$ , so that the probability  $K$  on each pentachoron  $p$  would simply be the average of the probabilities on adjacent pentachorons at the previous step:

$$K(p, p_0; \tau + 1) = \frac{1}{5} \sum_{p' \in \mathcal{N}(p)} K(p', p_0; \tau). \quad (4.16)$$

For an hypercubic lattice, it is easy to convince oneself that the return probability would alternate finite values with null values, and this is due to the marginal instability of the update<sup>11</sup>, which might or may not guarantee a good behaviour.

---

<sup>11</sup>For rate factors  $\eta > 1$  the numerical scheme in eq. (4.11) is unstable, whereas it is stable for

However, as claimed in [4], for CDT triangulations this problem does not arise for sufficiently high diffusion times, probably because of their random structure.

As a little experiment, we tried to verify this claim.

The blue and green lines in figure 4.10 show the spectral dimension resulting from choosing two different rate factors,  $\eta = 1$  (blue line) and  $\eta = \frac{2}{3}$  (green line), where for the latter the diffusion time has been rescaled accordingly:  $\tau \rightarrow \eta\tau$ , so that one needs to perform a fraction  $\frac{1}{\eta}$  of iterations to get the same range in diffusion-time. The halos, surrounding the two curves, represents the error<sup>12</sup> propagated from the average of return probabilities through different configurations.

Notice that, for small diffusion times (lower than 40 steps) the curve for  $\eta = 1$  (blue) is not reliable, since the corresponding return probability jumps wildly due to the marginal stability of the update, while the curve for  $\eta = \frac{2}{3}$  (green) seems well behaved everywhere.

However, there is not much difference between the blue and green curves for times  $\tau \gtrsim 40$ , so the claim is correct.

How the behaviour of the spectral dimension shown in figure 4.10 should be interpreted?

First of all, for small diffusion times the spectral dimension seems to fall to values near 2, meaning, informally, that a random walker “sees” (on average) an almost two dimensional space at small scales. This observation, called *dimensional reduction*, was first observed in CDT but subsequently rediscovered also in many other approaches of Quantum Gravity, all pointing toward the idea that spacetime effectively two dimensional on Planckian scales. There are various interpretations about the reason why this should happen. One of the most interesting is probably the possibility that a dynamical reduction from four to two dimensions must occur at short-scales/high-energies in order to make the Newton constant dimensionless (as it is in 2 dimensions) [19]. Recall from section 2.4 that if the asymptotic safety conjecture turns out to be true, a fixed point for finite values of Newton constant and cosmological constant exists, and the theory corresponding to that fixed point is scale-invariant. But a coupling with non-zero mass dimension like the Newton constant ( $[G] = 2 - d$ ) in a scale-invariant theory must be or zero or infinity, unless its anomalous dimension do not compensates exactly the difference at the fixed point, suggesting a mechanism that should lead the dimension observed at ultraviolet regimes to  $d = 2$ .

The spectral dimension indeed seems to be scale dependent, excluding the possibility that the spacetime is self-similar like a fractal.

For diffusion times sufficiently large the spectral dimension gets closer to the classical value  $d = 4$ . However, for diffusion times higher than the right limit of the plot in figure 4.10, the spectral dimension attain a negative slope due to finite-size effects, so the *asymptotic dimension*<sup>13</sup> can be estimated only for a certain range of diffusion times  $[\tau_{min}, \tau_{max}]$ . The best fit curve proposed by Ambjorn et al. [4] is

$\eta \leq 1$ .

<sup>12</sup>Here the use of a resampling method and blocking procedure is crucial to get a correct estimate of errors.

<sup>13</sup>What we call asymptotic dimension is, informally, the dimension that would be “felt” by a random walker if the structure would be infinitely extended.

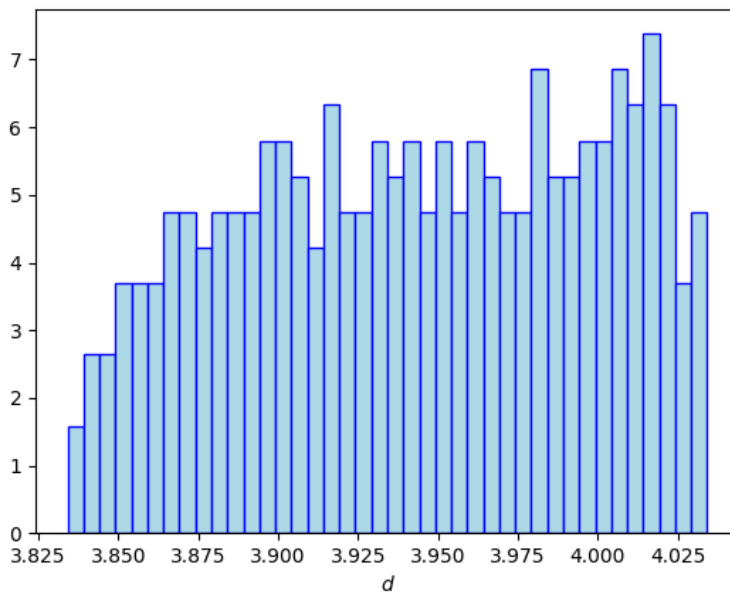


Figure 4.11: Histogram of the best fit estimates of the asymptotic dimension  $d$  by using eq. (4.17) for various ranges in diffusion times  $[\tau_1, \tau_2]$ .

given by the formula

$$D_S(\tau) = d - \frac{a}{b - \tau}, \quad (4.17)$$

where  $d$  should be interpreted as the asymptotic dimension of the system for large scales.

Using the functional form (4.17), a best estimate of the asymptotic dimension  $d$  can be obtained by means of a standard fit. However, to estimate the error on this estimate we need to resort to another approach, since the errors in the curve are strongly correlated in an unknown way, and therefore the errors from a standard fit procedure, which assumes independent errors, are meaningless. We then performed the following procedure: we made many fits of the functional form (4.17) for different ranges of diffusion times  $\{[\tau_1, \tau_2] \mid \tau_1 \geq \tau_{min} = 20, \tau_2 \leq \tau_{max} = 400\}$ , and for each of them we obtained the best estimate. From the histogram of the estimates  $\{d_i\}$  (see figure 4.11) one can establish how much the value fluctuates for different choices of the range, so its spread is an estimate of the error on  $d$ . Our result is  $d = 3.94 \pm 0.05$ .

In section 5.4 we will discuss about the spectral dimension of spatial slices and we will provide an alternative method to derive the spectral dimension.

### 4.2.3 Numerical resources

Before taking measures from any Markov chain Monte-Carlo simulation with arbitrary initial configuration, one should wait a certain time, called *thermalization time*, to guarantee the stationarity of the Markov chain, and therefore a correct sampling of the probability distribution. The thermalization time depends from the point in the phase diagram, the volume chosen, and is related to the autocorrelation

time of the slowest observables (higher near the transition lines).

To give an idea of the typical times, our simulations of the Standard and TBlocked algorithms needed about one week to thermalize, in the simulation line across the  $B|C$  transition with  $k_0 = 2.2$  and using a volume fixing  $N_4^{(4,1)} = 80k$ . The simulations were performed almost always using suboptimal implementations for testing purposes (partial debug mode).

## 4.3 Tests for the TBlocked algorithm

First of all, we need to verify that our implementation of the TBlocked algorithm does indeed reproduce results in agreement with our implementation of the standard algorithm; from the previous analyses, it would be consistent with the implementations used in literature by transitivity.

Secondly, we will benchmark the two algorithm, analyzing the autocorrelation times for relevant variables in order to evaluate their relative efficiency.

### 4.3.1 Average estimates compatibility

As test of correctness for the TBlocked algorithm, we chose to compare the lines of simulation along the  $A|C_{ds}$  transition. In particular, we have computed and compared the averages of the order parameter  $\text{conj}(k_0)$  obtained by performing numerical simulations with both algorithms put in the same conditions: volume  $N_4 = 40k$ ,  $\Delta = 0.6$  and  $k_0$  ranging in  $[2.2, 5.2]$ .

Notice that these are the same points and conditions of the plot in figure 4.5. The curves of the order parameter as function of  $k_0$  obtained from the two algorithms are hardly distinguishable, so it would be useless to show also the plot corresponding to the TBlocked algorithm.

We need a more informative representation of the averages of  $\text{conj}(k_0)$ , in order to compare them for each value of  $k_0$ . Figure 4.12 shows the result of such comparisons, where for each  $k_0$  we subtracted the mean of the two estimates in order to represent data around zero, since we are interested in their relative value and errors.

Regarding the error on the averages, it has been estimated by resampling<sup>14</sup>, and regrouping data from the histories into adjacent blocks, in order to lower the correlations between close configurations in Monte-Carlo time<sup>15</sup>.

The error bars indicate that the estimates are nearly compatible for almost all  $k_0$ .

### 4.3.2 Comparison of efficiency for the Standard and TBlocked algorithms

Estimating the performance of an algorithm is independent from testing its correctness, and requires particular care.

---

<sup>14</sup>Resampling consists in generating a certain number of dataset from the original one by extracting randomly its elements. The averages from each generated dataset are then combined to estimate the error on the average of the original dataset.

<sup>15</sup>This statistical technique is called *blocking*. This should not be confused with the term used in the Renormalization Group formalism.

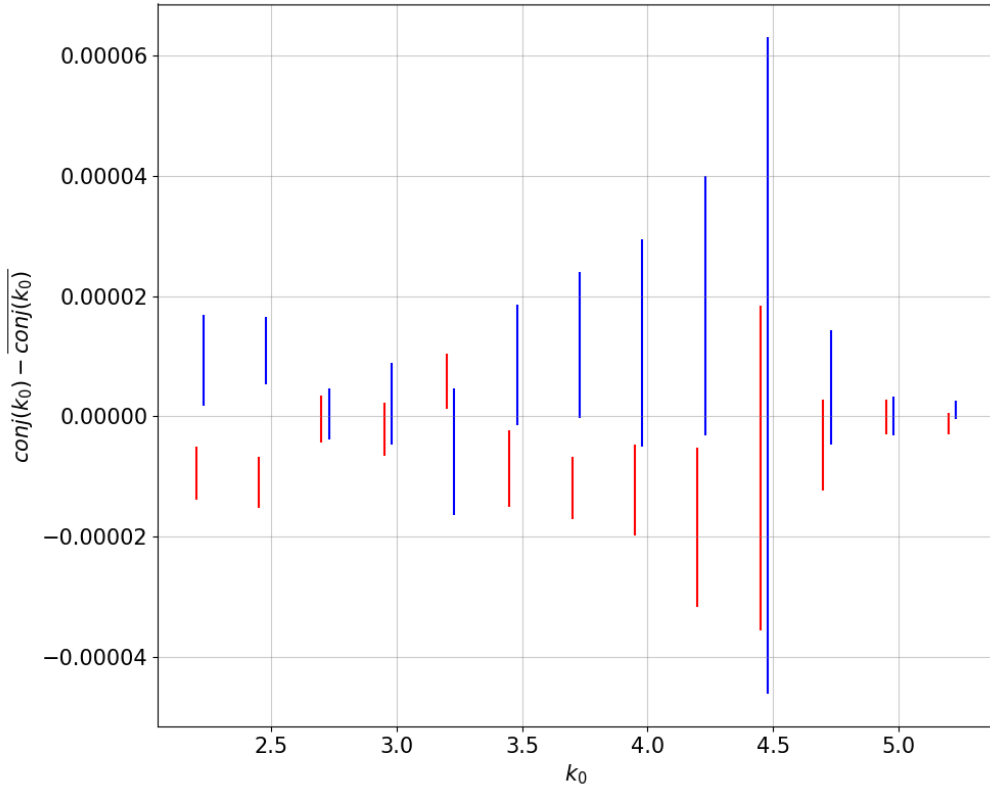


Figure 4.12: Comparison of the estimate of the relative average of  $\text{conj}(k_0)$  for different values of  $k_0$ , obtained from simulations implementing the standard (red bars) and TBlocked (blue bars) algorithms.

First of all, we need to define what we mean with *efficiency*. In Monte-Carlo simulations, algorithmic efficiency<sup>16</sup> is defined as the rate for which configurations in the Markov chain gets *decorrelated* with respect to some chosen set of observables. Here we made two types of tests: the first is an analysis of the autocorrelation times for the order parameter of the  $B|C$  transition, the second is an estimate of the rapidity with which the position (in slice time) of the center of volume and tails of configurations evolves in simulation time.

### Autocorrelation time for the order parameter $\text{conj}(\Delta)$

The autocorrelation time for a given observable is, in layman terms, the time that must pass before the values of that observable in an Monte-Carlo history could be considered independent.

It is usually represented in units of Monte-Carlo steps, but, when it comes to compare different algorithms, this is not the correct way to proceed, since they could take more or less *clock-wall time*<sup>17</sup> on average to perform a single step, and moreover each type of move could perform very differently.

Another complication for the comparison is that, in CDT, measures of observables

<sup>16</sup>In general settings, the efficiency of an algorithm depends also on the size of the maximum memory space which needs to be allocated in order to perform computations.

<sup>17</sup>That informally is the time we measure with a standard clock.

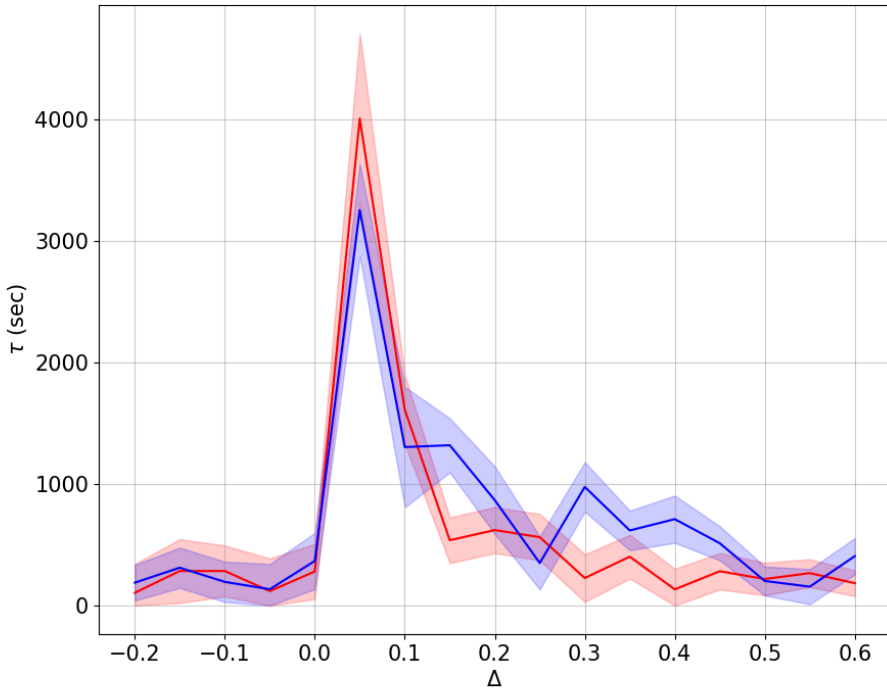


Figure 4.13: Autocorrelation time of  $\text{conj}(\Delta)$  in clock-wall units and along a simulation line across the  $B|C$  transition line ( $k_0 = 2.2$  and  $N_4 = 40k$ ).

are taken only whenever the volume is equal (with some strict tolerance) to the target volume given by the volume fixing term (see 2.3.1).

This means that the sample of measures is not equally spaced neither in simulation time, but occur on average only after a certain number of steps.

The observables are measured every only whenever the volume equals the target one, so any quantity computed in units of the data sampled will be estimated in what we will refer to as *measure time*.

An accurate analysis should take into account each of these complications.

First of all, we measure, for both algorithms, the average clock-wall time that it takes to perform a single step, let us call it  $\Delta t_s$ ; it will be computed as the asymptotic value of the ratio between the time of simulation  $t$  and the total number of steps performed until that time  $s(t)$ :  $\Delta t_s \equiv \lim_{t \rightarrow \infty} \frac{t}{s(t)}$ .

Then we estimate the average number of measures  $n_m(s)$  taken after  $s$  steps, and call its ratio  $\rho_m \equiv \lim_{s \rightarrow \infty} \frac{n_m(s)}{s}$  (a quantity strictly less than 1 by definition).

Finally, we estimate the autocorrelation time  $\tau_{\text{meas}}$  on the set of measures, that is in measure time, and multiply the result by the previous factors, so that our estimate of the clock-wall autocorrelation time would be

$$\tau_{\text{cw}} = \frac{\tau_{\text{meas}}}{\rho_m} \Delta t_s. \quad (4.18)$$

Figure 4.13 shows the estimates of the autocorrelation times  $\tau_{\text{cw}}$  for the points in a simulation line crossing the  $B|C$  transition line, where the contributions from

$\rho_m$  and  $\Delta t_s$  have been taken into account using eq. (4.18).

We need to add also, in this simulation, that the number of blocks used for the TBlocked algorithm in this analysis is 4. In the  $B$  phase ( $\Delta \lesssim 0$ ) the two algorithms seem to have comparable autocorrelation times; this is reasonable, since the volume will be localized in only one slice, and even if the TBlocked algorithm makes three empty step and one true step on average, they former will be rejected immediately, and the time of rejection is negligible.

Around the  $B|C$  transition ( $\Delta \simeq 0$ ) the TBlocked algorithm seems to perform marginally better than the standard one, while the situation in the  $C$  phases is somewhat unclear, but nevertheless sufficiently compatible within errors.

In short, regarding the autocorrelation time associated to the order parameter  $\text{conj}(\Delta)$  for the  $B|C$  transition, the results from the two algorithms do not show significant differences.

However, as we argued in section 3.4.2, unlike the Standard algorithm, the TBlocked algorithm is ready to be parallelized, resulting in an overall speed-up of simulations. For example, in the best case scenario, the autocorrelation time in clock-wall units for a TBlocked parallelized algorithm with 4 blocks would be about 4 times lower than the TBlocked serial algorithm<sup>18</sup>.

### Rapidity of evolution for the slow modes

The ideas of the TBlocked algorithm came from the observation of slow modes in the simulations. Here we want to analyze the motion of the position (in slice time) of the center of volume and tails<sup>19</sup> (see figure 4.14), to verify if the TBlocked algorithm evolve faster these variables than the Standard one.

We cannot perform a standard autocorrelation analysis though, since these quantities behave, in simulation time, like *random walks*<sup>20</sup>.

From the theory of stochastic processes there is a profound connection between random-walks and their continuous counterparts, namely Wiener processes; for practical reasons, we will employ the notation used for the latter, so we will denote a possible realization of a random walk as a function  $x(t)$ .

A 1-dimensional random walker starting from  $x(0) = 0$  would be expected at any time  $t$  to be located, on average, at  $\langle x(t) \rangle = 0$ .

The proper quantity that we should use to describe how fast a random walker moves on a line, is the diffusion coefficient, defined as follows:

$$D = \frac{\langle x^2(t) \rangle}{t}. \quad (4.19)$$

For our purposes, we considered the slice time axis as infinitely extended in both directions, without bothering about periodicity and treating the position of the center of volume and tails as integer numbers ( $\mathbb{Z}$ ). In our setting, the role of the

<sup>18</sup>The only one that, at present, we have actually implemented.

<sup>19</sup>We defined the position of the tails in slice time as the first

<sup>20</sup>We are assuming that each step is independent from the other. This is motivated by the observation that the algorithm is a Markov process in simulation time, and detailed balance, combined with time-translation symmetry, makes equals the probabilities to move forward or backward (on stationary distributions). There could be, however, some correlation hidden in the definition of center of volume, and the fact that the volume distribution is only an effective representation of triangulation.

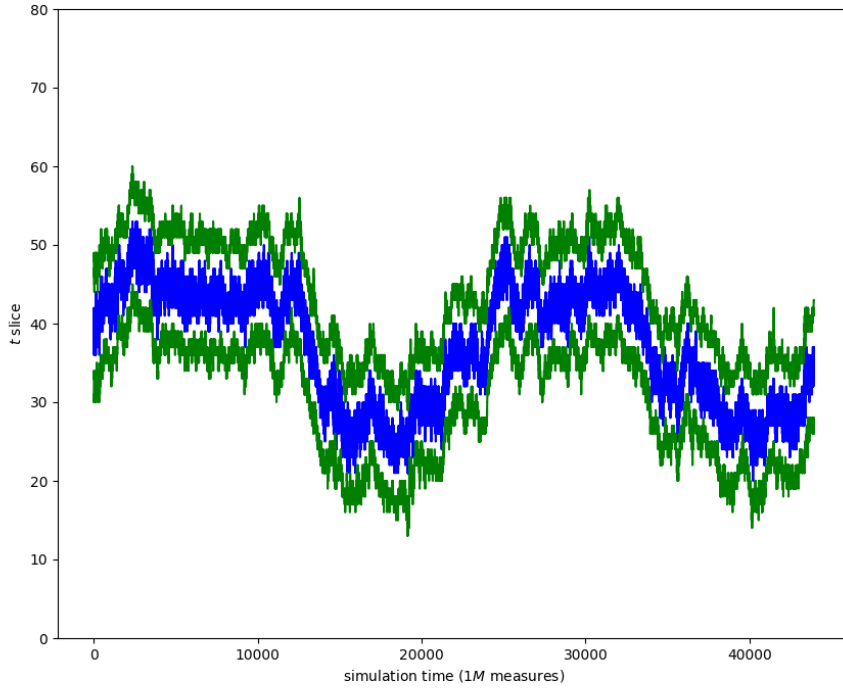


Figure 4.14: Random motion, in simulation time, of the center of volume (blue line) and tails (green lines) of a blog along the slices obtained with the standard algorithm in the de Sitter phase. Notice that the increments are integer values, and the  $y$  axis is actually closed in a circle.

position  $x$  is taken by one of the following variables:  $\tau_{cv}(t)$  is the distance traveled by the center of volume as defined in 4.2.1, whereas  $\tau_1$  and  $\tau_2$  are respectively the positions of the tails, defined as the slice times for the two slices nearest to the center of volume and with a spatial volume lower than an arbitrary factor  $\varepsilon$  of the total spatial volume; here we fixed  $\varepsilon = 0.005$ .

To get more data, the variance in the position  $x(t)$  of any of the slice times introduced above, can be estimated as the average of all random walks starting from a time  $\bar{t}$ :

$$\langle x^2(t) \rangle \equiv \langle (x(\bar{t} + t) - x(\bar{t}))^2 \rangle \quad (4.20)$$

Figure 4.15 shows the results of the estimates of the variance  $\langle x^2(t) \rangle$  at the simulation time  $t$ , given by eq. (4.20) and for two simulations performed with the Standard and TBlocked algorithms in the de Sitter phase.

The slope of the curves gives an estimate of the diffusion coefficient in eq. (4.19), and as expected, the random walk seems somewhat faster in the case of the TBlocked algorithm.

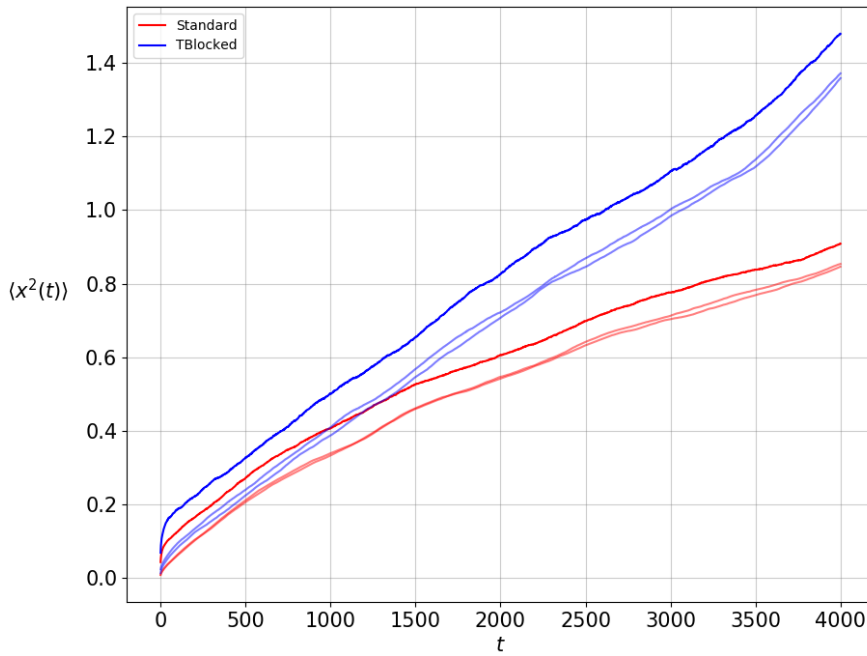


Figure 4.15: Comparison between the relative spreads as functions of simulation time for the random walks of the center of volumes and tails for the Standard and TBlocked algorithm at the de Sitter phase. The slope gives an estimate of the diffusion coefficient  $D$ .

# Chapter 5

## Laplace-Beltrami spectral analysis

As anticipated in chapter 2, one of the main open problems in pure-gauge Quantum Gravity is the paucity of useful observables.

One can come up with definitions like the fractal dimensions or order parameters, or even phase-specific observables like spread and fluctuations of the blob in the  $C_{dS}$  phase. However, such definitions form by no mean a complete set of observables characterizing the geometries of triangulations.

For example, it would be interesting to study how the curvature is distributed on configurations, or what is the shape of spatial slices. However, as usual in Quantum Mechanical Monte-Carlo simulations, most of the configurations in the path-integral are fractal-like at microscopic scale, so it is not obvious, at least for random lattices, how to implement a coarse graining which captures the large scale shape of these geometries. No concept of “average of geometry” appears to be meaningful. This observation could discourage analysis of large scale properties, because it seems overly complicated to do define “smeared” observables. We would verify, for example, that the geometry of spatial slices in the de Sitter phase can be actually approximated by the one of the sphere  $S^3$  on large scales.

In this chapter we propose a novel method, to which we will refer to as *Laplace-Beltrami spectral analysis*, to solve these issues in CDT. Here we will restrict the analysis to individual spatial slices, since the implementation is simpler than the one needed to describe the full spacetime geometry. Nevertheless, in section 5.8 we will describe how the approach can be generalized, although with some implementative effort.

### 5.1 Motivations

As shown in 4.2.2, the return probability for diffusion processes on the triangulation gives us information about the spectral dimension. It seems that, if we want to capture more detailed geometric features, we need to resort to other methods, but we will show that the diffusion equation (4.10) does indeed contain the germ of the idea to extract much more information.

To see why, let us consider the diffusion equation on the circle,

$$\partial_t u(x, t) = \nabla^2 u(x, t) \quad \forall x \in [0, 2\pi], \quad (5.1)$$

where in this case the Laplacian is simply  $\nabla^2 \equiv \partial_x^2$  and the solution  $u$  is a periodic function in  $L^2([0, 2\pi])$ .

The canonical approach to analytically solve this differential equation for any initial condition is to rewrite the spatial part of the function  $u$  in Fourier series

$$u(x, t) = \sum_{k=-\infty}^{+\infty} u_k(t) e^{ikx} \quad (5.2)$$

so that eq. (5.1) becomes a set of *decoupled* equations

$$\partial_t u_k(t) = -k^2 u_k(t) \quad \forall k \in \mathbb{Z}. \quad (5.3)$$

These are easily integrated, giving

$$u_k(t) = u_k(0) e^{-k^2 t} \quad \forall k \in \mathbb{Z}, \quad (5.4)$$

so that the general solution to the problem is

$$u(x, t) = \sum_{k=-\infty}^{+\infty} u_k(0) e^{ikx - k^2 t}, \quad (5.5)$$

where the numbers  $u_k(0)$  are determined by fixing initial conditions.

Notice how the Fourier series simplifies the Laplacian term of the differential equation (5.1). This happens precisely because the set of functions  $\{e_k(x) \equiv e^{ikx}\}_{k \in \mathbb{Z}}$  is an orthonormal<sup>1</sup> basis of eigenstates of the Laplacian operator on the circle, with eigenvalues  $\{\lambda_{|k|} \equiv -k^2\}$  since  $\nabla^2 e^{ikx} = -k^2 e^{ikx}$ . Here  $|k|$  can be interpreted as a “spatial frequency”, because the larger  $|k|$  the faster the function  $e_k(x)$  oscillates with respect to  $x$ , with a spatial wavelength  $l_{|k|} \equiv \frac{2\pi}{|k|}$ ; in particular, the basis element at  $k = 0$  is a uniform function  $e_0(x) = 1$ .

This allows for a nice physical interpretation: by means of the Fourier series, each function  $f \in L^2([0, 2\pi])$  is decomposed, in components of different spatial resolution, so that the Fourier coefficients  $f_k$  and  $f_{-k}$  capture information about the behavior of  $f(x)$  at the spatial scale given by the wavelength  $l_{|k|}$ .

The decomposition is not actually unique, since eigenvalues  $\lambda_{|k|}$  are 2-degenerate (with the exception of  $\lambda_0 = 0$ ), and this makes possible e.g. to represent functions in  $L^2([0, 2\pi])$  by the familiar series in sines and cosines, that is using the base  $\{\cos(kx)\}_{k=0}^{\infty} \cup \{\sin(kx)\}_{k=1}^{\infty}$ .

This procedure can be extended to more general domains, like differentiable Riemannian manifolds  $(\mathcal{M}, g_{\mu\nu})$ , where the *Laplace-Beltrami operator* reads

$$\nabla^2 f = \frac{1}{\sqrt{|g|}} \partial_\mu (\sqrt{|g|} g^{\mu\nu} \partial_\nu f) \quad (5.6)$$

Restricting  $f$  to the Hilbert space of functions on  $\mathcal{M}$ , eigenvalues and eigenvectors are defined as solutions to the eigenvalue problem:

$$\nabla^2 u(x) = \lambda u(x). \quad (5.7)$$

---

<sup>1</sup>The norm is induced by the standard inner product of the Hilbert space  $L^2([0, 2\pi])$ , that can be defined by  $(f, g) = \int_0^{2\pi} \frac{dx}{2\pi} f^*(x) g(x)$ .

For example, the familiar *spherical harmonics*  $Y_{j,m}(\theta, \phi)$  are eigenfunctions of the Laplace-Beltrami operator on a sphere  $S^2$ , with eigenvalues  $\lambda_j = -j(j+1)$  and multiplicity  $\mu_j = 2j+1$ .

In general it can be shown ([20]) that, independently of the choice of eigenfunctions, the spectrum of the Laplace-Beltrami operator for a  $n$ -sphere  $S^n$  with  $n \geq 2$  is made of eigenvalues and respective multiplicities given by

$$\lambda_j^{(n)} = j(j+n-1), \quad (5.8)$$

$$\mu_j^{(n)} = \binom{n+j}{n} - \binom{n+j-2}{n}. \quad (5.9)$$

The benefit of representing any scalar function  $f : \mathcal{M} \mapsto \mathbb{C}$  in a base of eigenstates  $\{e_{\alpha,\nu}(x)\}$  of the Laplace-Beltrami operator on  $\mathcal{M}$  is that the coefficients

$$\left\{ f_{\alpha,\nu} \equiv \int_{\mathcal{M}} f(x) e_{\alpha,\nu}(x) \right\}_{\nu=0}^{\mu_{\alpha}-1}, \quad (5.10)$$

associated to a given eigenvalue  $\lambda_{\alpha}$  with multiplicity  $\mu_{\alpha}$ , encode the “strength” of the components at the wavelength scale  $l_{\alpha} = \frac{2\pi}{|\lambda_{\alpha}|^{\frac{1}{2}}}$ . So, truncating the series at some eigenvalue  $\lambda_{\bar{\alpha}}$  (where  $|\lambda_{\alpha}| < |\lambda_{\alpha+1}|$ ) yields a function

$$f_{\bar{\alpha}}(x) \equiv \sum_{\alpha=0}^{\bar{\alpha}} \sum_{\nu=0}^{\mu_{\alpha}-1} f_{\alpha,\nu} e_{\alpha,\nu}(x) \quad (5.11)$$

This is a coarse-grained version of the original function  $f(x)$ , where “microscopic” details at scales  $l < l_{\bar{\alpha}} \equiv \frac{2\pi}{|\lambda_{\bar{\alpha}}|^{\frac{1}{2}}}$  are neglected.

Another useful observation is that the same spectrum of the Laplace-Beltrami operator on a manifold gives geometric information of the manifold itself. One might wonder if the shape of a manifold can be completely inferred by the Laplace-Beltrami spectrum. This interesting problem can be informally depicted by the popular phrase “Can One Hear the Shape of a Drum?” by Mark Kac [21]. The answer is *almost*, since counterexamples of isospectral manifolds have been presented in literature. Some ambiguity in the manifold reconstruction is possible, but nevertheless, one can in principle extract almost all geometric features of the manifold at a given scale.

Similar considerations can be applied to discrete domains. For example in an unidimensional periodic lattice with size  $L$  and  $N$  sites there are many ways to discretize the Laplace-Beltrami operator. The simplest one can be built by Taylor expanding to second order an arbitrary periodic function defined in  $[0, L]$ ; using the lattice spacing  $a = L/N$ , and expanding around a point on the lattice  $x_n = na$  ( $n \in \{0, 1, \dots, N-1\}$ ) we have

$$f(x_{n+1}) = f(x_n) + \frac{df}{dx}(x_n) a + \frac{1}{2} \frac{d^2 f}{dx^2}(x_n) a^2 + \mathcal{O}(a^3), \quad (5.12)$$

$$f(x_{n-1}) = f(x_n) - \frac{df}{dx}(x_n) a + \frac{1}{2} \frac{d^2 f}{dx^2}(x_n) a^2 + \mathcal{O}(a^3), \quad (5.13)$$

where the indices of  $x_m$  are taken modulo  $N$ .

Summing the expressions (5.12) and (5.13), subtracting twice  $f(x_n)$ , and dividing by  $a^2$ , we obtain a first-order approximation to the Laplace-Beltrami operator (here  $\frac{d^2}{dx^2}$ )

$$\nabla^2 f(x_n) = \frac{d^2 f}{dx^2}(x_n) = \frac{f(x_{n+1}) + f(x_{n-1}) - 2f(x_n)}{a^2} + \mathcal{O}(a). \quad (5.14)$$

The  $f$ -dependence in expression (5.14) can be abstracted away by considering the values of the scalar function  $f$  as components of a vector<sup>2</sup>  $\vec{f} = \{f_n \equiv f(x_n)\}_{n=0}^{N-1} \in \mathbb{R}^N$ . In this way, the linearity of the Laplace-Beltrami operator makes possible to write eq. (5.14) in matrix form

$$-\nabla^2 f \rightarrow \frac{1}{a^2} L \vec{f} + \mathcal{O}(a) = \frac{1}{a^2} \begin{pmatrix} 2 & -1 & & 0 \\ -1 & \ddots & \ddots & \\ & \ddots & \ddots & -1 \\ 0 & & -1 & 2 \end{pmatrix} \vec{f} + \mathcal{O}(a), \quad (5.15)$$

where we have introduced the *Laplace-Beltrami matrix*  $L$  of the discrete lattice; the minus sign is conventional, and comes from the non-positiveness of the eigenvalues of the Laplace-Beltrami operator  $\nabla^2$ . The discrete case can be treated in analogy with eq. (5.7), and therefore eigenvalues and eigenvectors for the Laplace-Beltrami matrix  $L$  are defined by the eigenvalue problem:

$$L \vec{u} = \lambda \vec{u}. \quad (5.16)$$

However, the regular tiling of lattices is not capable of approximating non-trivial domains; square or triangular grids are extensively used to implement numerical simulations of quantum field theories like QCD, where the Wick-rotated Minkowski space has typically the geometry of a torus  $T^4 \cong S^1 \times S^1 \times S^1 \times S^1$ , but being interested in gravitational theories where the dynamical variable is the geometry itself, we need to represent discretely arbitrary manifolds  $(\mathcal{M}, g_{\mu\nu})$ .

Lattices can be replaced by the more general structures called *graphs*.

A graph  $G$  is formally a pair of (finite) sets  $(V, E)$ , where  $V$  contains *vertices*, which assume the role of the former lattice sites, whereas  $E \subset V \times V$  is a binary relation on  $V$  encoding the connectivity between vertices in the form of ordered pairs of vertices  $\{(v_a, v_b)\}$ .

An element  $(v_a, v_b)$  of  $E$  is commonly called *edge* since represent a connection from a vertex  $v_a$  to another one  $v_b$ . The simplest way to generalize the adjacency relation between sites of the lattices is considering *undirected* graphs, that is graphs  $G = (V, E)$  where the relation  $E$  is symmetric:  $(v_a, v_b) \in E \implies (v_b, v_a) \in E$  (each edge comes in both directions).

For a general undirected graph  $G = (V, E)$ , where  $V = \{v_i\}_{i=0}^N$  is an (ordered) set of vertices and  $E$  is the set of unordered pairs of connected vertices, we can define the associated *Laplace-Beltrami matrix* by the expression<sup>3</sup>

$$L = D - A, \quad (5.17)$$

---

<sup>2</sup>We are approximating then the space of real periodic functions  $\{f \in L^2([0, L]) | f(0) = f(L)\}$  by the linear space  $\mathbb{R}^N$

<sup>3</sup>Other possible definitions of the Laplace-Beltrami matrix can be employed.

where  $D$  is the diagonal *degree matrix* such that, for all  $i \in \{0, 1, \dots, N - 1\}$ , the element

$$D_{ii} \equiv |\{e \in E | v_i \in e\}| \quad (5.18)$$

is the number of vertices connected to the vertex  $v_i$  ( $D_{ij} = 0$  if  $i \neq j$ ), while  $A$  is the symmetric *adjacency matrix* such that the element

$$A_{ij} = \chi_E(\{i, j\}) \quad (5.19)$$

is 1 only if the vertices  $v_i$  and  $v_j$  are connected ( $\{i, j\} \in E$ ) otherwise it is zero<sup>4</sup>. It is obvious that in the previous example of the unidimensional periodic lattice we had

$$D = 2 \mathbb{1}_{N \times N}, \text{ and } A_{ij} = \delta_{i,(j+1) \bmod N} + \delta_{i,(j-1) \bmod N}. \quad (5.20)$$

The computation of eigenvalues and eigenvectors of the Laplace-Beltrami matrix  $L$  can be efficiently performed by standard algorithms, and the geometric interpretation of the eigenspectrum displayed above becomes available. In particular, the Laplace-Beltrami matrix  $L$  of an undirected graph  $G$  is real, symmetric and positive semi-definite (real and non-negative eigenvalues), so by the spectral theorem can be always diagonalized.

Let us consider the spectrum  $\sigma_G = \{\lambda_\alpha\}$  of distinct eigenvalues with increasing order  $0 = \lambda_0 < \lambda_1 < \dots < \lambda_{|\sigma_G|-1}$ , notice that the lowest eigenvalue  $\lambda_0$  of the Laplace-Beltrami matrix is always zero, since the uniform function is always an eigenvector. We denote by  $\mu_\alpha$  the multiplicity of the eigenvalue  $\lambda_\alpha$ , which corresponds, by diagonalizability, to the dimension of the space  $V_\alpha$  of eigenvectors associated to the eigenvalue  $\lambda_\alpha$ . As in the smooth-manifold case, for each  $\alpha$  we can choose any base  $\{\vec{e}_{\alpha,\nu}\}_{\nu=0}^{\mu_\alpha-1}$  for the eigenspace  $V_\alpha$ , where we introduced a new index  $\nu$  labelling its elements ( $\nu \in \{0, 1, \dots, \mu_\alpha - 1\}$ ). Then, one of many possible basis for the discretized function space  $\mathbb{R}^{|V|}$ , consisting of eigenvectors of the Laplace-Beltrami matrix associated to the graph  $G$ , can be written in the form

$$\mathcal{B}_G = \bigcup_{\lambda_\alpha \in \sigma_G} \{\vec{e}_{\alpha,\nu} \in \mathbb{R}^{|V|} | \nu = 0, 1, \dots, \mu_\alpha - 1\}, \quad (5.21)$$

which, from now on, we will consider always orthonormal.

Notice that different algorithms used to compute eigenvalues and eigenvectors must return the same spectrum (set of distinct eigenvalues  $\sigma_G$  with associated multiplicities), but can actually yield different bases  $\mathcal{B}_G$  of eigenvectors, if degeneracies are present ( $\mu_\alpha > 1$  for some  $\alpha$ ).

Both the spectrum of eigenvalues  $\sigma_G$  and the base of eigenvectors  $\mathcal{B}_G$  for a general undirected graph  $G$  can be obtained by numerical routines, and give interesting information about the geometry of the graph. Lowest eigenvalues are associated to topological or large-scale modes, such that the corresponding eigenvectors vary with a large wavelength, while eigenvectors associated to higher eigenvalues describe short-scale resolutions.

For example, if the graph has  $m$  connected components, the zeroth eigenvalue  $\lambda_0$  has multiplicity  $\mu_0 = m$ , since one can choose a base of eigenvectors  $\{\vec{e}_{0,\nu}\}_{\nu=0}^m$  for

---

<sup>4</sup>We denote the indicator function for the set  $S$  by  $\chi_S(x) = \begin{cases} 1 & \text{if } x \in S \\ 0, & \text{if } x \notin S \end{cases}$ .

$V_0$  such that  $\vec{e}_{0,\nu}$  is non-zero and uniform on the  $\nu$ -th component and zero on the others.

*Spectral graph theory* is the branch of mathematics studying spectral properties of the Laplace-Beltrami matrix and the adjacency matrix associated to graphs. Research on this field is acquiring growing interest in the late years due to its applications in the analysis of complex networks and in the context of shape analysis ([22]). From eigenvalues and eigenvectors of the LB matrix many interesting geometric properties of the graph can be inferred, and some of them will be discussed in the following section (sec. 5.2).

For example, the smallest non-null eigenvalue  $\lambda_1$  is called *Fiedler value*, and encodes how much a graph is connected: the further from zero the more compactly connected are points. The Fiedler value is also related to the *Cheeger constant* (see sec. 5.2), which is a measure of the “bottleneckedness” of the graph. Going to higher eigenvalues and associated eigenvectors, their topological interpretation fades and blends with more geometrical features.

### 5.1.1 Spectral analysis of local observables

As already discussed for the smooth-manifold case, any scalar function  $f : V \rightarrow \mathbb{C}$  defined on the vertices of the graph  $G$ , and here represented by a vector  $\vec{f} \in \mathbb{C}^{|V|}$ , can be “Fourier transformed” in components of the computed basis  $\mathcal{B}_G$  by taking scalar products

$$\hat{f}_{\alpha,\nu} \equiv \sum_{v \in V} f(v) e_{\alpha,\nu}(v) \equiv (\vec{f}, \vec{e}_{\alpha,\nu}) \quad \forall \vec{e}_{\alpha,\nu} \in \mathcal{B}_G. \quad (5.22)$$

Following the argument given above, for any  $\alpha > 0$  and function  $\vec{f}$ , we can isolate function contribution  $\tilde{f}_\alpha$  at wavelength  $l_\alpha \equiv \frac{2\pi}{|\lambda_\alpha|^{\frac{1}{2}}}$  by taking the norm of the function projection on the eigenspace  $V_\alpha$ :

$$\tilde{f}_\alpha \equiv \sqrt{\sum_{\nu=0}^{\mu_\alpha-1} |\hat{f}_{\alpha,\nu}|^2}. \quad (5.23)$$

The advantage of using  $\{\tilde{f}_\alpha\}$  over  $\{\hat{f}_{\alpha,\nu}\}$  is that they do not depend on the numerical routine employed to compute them, since do not suffer from possible ambiguities inherent on the base choice, but depend only on the spectral decomposition of the vertex space  $\mathbb{R}^{|V|}$ , which is in turn dictated uniquely by the geometric properties of the graph  $G$ . The pairs  $\{(l_\alpha, \tilde{f}_\alpha)\}_{\lambda_\alpha \in \sigma_G}$  encode the  $f$ -contribution per wavelength and are interesting to detect for example characteristic scales of the function  $f$ .

Furthermore, we can construct a coarse-grained version of the function  $f(v)$ , defined locally (that is on vertices), by truncating the inverse Fourier series for eigenvalues larger than a fixed eigenvalue  $\lambda_{\bar{\alpha}}$

$$f_{\bar{\alpha}}(v) \equiv \sum_{\alpha=0}^{\bar{\alpha}} \sum_{\nu=0}^{\mu_\alpha-1} f_{\alpha,\nu} e_{\alpha,\nu}(v) \quad \forall v \in V. \quad (5.24)$$

This coarse-graining procedure smears out effectively microscopic details at scales lower than  $l_{\bar{\alpha}} \equiv \frac{2\pi}{|\lambda_{\bar{\alpha}}|^{\frac{1}{2}}}$ , or equivalently imposes an high-momentum cut-off at  $\Lambda =$

$$|\lambda_{\alpha}|^{\frac{1}{2}}.$$

## 5.2 Properties of the eigenspectrum of the Laplace-Beltrami matrix

As already argued, the spectrum of eigenvalues  $\sigma_G$  and the computed orthonormal base of eigenvectors  $\mathcal{B}_G$  give useful geometric information. In this section we will describe some of the most relevant results from spectral graph theory that allows us to extract this information.

In the following we will consider only graphs with a single connected component<sup>5</sup>, like the ones occurring in CDT (see sec. 5.3).

Some general properties of eigenvalues and eigenvectors can be summarized by the following list, where it is convenient to keep in mind the analogy with the more familiar Fourier base made of cosines and sines:

- The base  $\mathcal{B}_G = \{\vec{e}_{\alpha,\nu}\}$  can (and will) always be taken real, since the spectral theorem for symmetric matrices applies.
- The eigenvector associated to the 0-th eigenvalue  $\lambda_0 = 0$  ( $\mu_0 = 1$ ) is uniform:  $\vec{e}_{0,0} = \frac{1}{\sqrt{|V|}} \vec{1}_{|V|}$ , where  $\vec{1}_{|V|}$  is the vector in  $\mathbb{R}^{|V|}$  with 1 on each entry.
- The sum of the components of every eigenvector  $\vec{e}_{\alpha,\nu}$ , with the exception of  $\vec{e}_{0,0}$ , is zero:  $\sum_{v \in V} e_{\alpha,\nu}(v) = (\vec{e}_{\alpha,\nu}, \sqrt{|V|} \vec{e}_{0,0}) = 0$  by orthogonality of  $\mathcal{B}_G$ .
- The components of every eigenvector are bounded between -1 and 1:  $\forall \alpha, \nu, v \quad -1 \leq e_{\alpha,\nu}(v) \leq 1$ .

Finer properties of the eigenquantities are discussed in the following subsection.

### 5.2.1 Interpretation of the first eigenvalues and eigenvectors

As discussed previously, the first eigenvalues encode information about large scales. The 0-th eigenvalue has topological character, and in the general case its multiplicity tells us how many connected components the graph is composed of, but for connected graphs its role is trivial and uninteresting.

Probably the most important geometric information at large scales comes from the first (non-null) eigenvalue  $\lambda_1$ , which is called *algebraic connectivity* or *Fiedler value*, and its associated eigenvectors  $\vec{e}_{1,\nu}$ , which are called *Fiedler vectors*.

The term “algebraic connectivity” comes from the observation that the larger  $\lambda_1$  is, the more connected is the graph. In particular, one could ask how to label vertices with distinct real numbers in such a way that close vertices corresponds as much

---

<sup>5</sup>The more general case of graphs with multiple connected components can be easily treated by studying its components individually: the Laplacian matrix is block-diagonal for each component, so its spectrum is the union of the individual spectra, and its eigenspaces are direct sums of the individual eigenspaces.

as possible to close labels (with  $l^2$  metric): this question can be rephrased by the constrained functional minimization problem

$$\min \left\{ \sum_{(v_1, v_2) \in E} (f(v_1) - f(v_2))^2 \mid \vec{f} \cdot \vec{f} = 1, \vec{f} \cdot \vec{1} = 0 \right\} \quad (5.25)$$

for a non-uniform “labeling function”  $f(v)$ , where the first constraint has been added to avoid solutions arbitrarily close to zero, whereas the second constraint selects a single representative among functions differing solely by a constant.

The optimal solutions to this problem are exactly linear (orthonormal) combinations of the Fiedler vectors  $\vec{f} \in \text{span}\{\vec{e}_{1,\nu}\}_{\nu=0}^{\mu_1-1}$ .

In the majority of the cases, especially in higher dimensions and when the graph do not possess particular symmetries,  $\mu_1 = 1$ , so there is only one Fiedler vector and then a unique optimal solution to the minimization problem (5.25).

Relabeling the vertices according to increasing values of Fiedler vector leads to the *Fiedler ordering*, a technique used in numerical linear algebra of sparse matrices to reduce the bandwidth (that is size of the band diagonal form), from which crucially depends the performance of many sparse solvers [23].

We need to mention also that the eigenvector associated to the second smallest eigenvalue of the (minus) adjacency matrix  $-A$ , identical to the Fiedler vector for regular graphs (since  $L = k\mathbb{1}_{N \times N} - A$  in that case), is the cornerstone of the famous *PageRank* algorithm [24], the main criterion of the Google Search engine which, with its effectiveness to order website pages by importance, determined largely the rise of success of the Google company.

To give an idea [25]: “a PageRank for 26 million web pages can be computed in a few hours on a medium size workstation”, already in the year 1998!

An important property of Fiedler vectors, which makes them extensively used in many fields, is *spectral bi-partitioning*, that is a subdivision of the graph vertices into two maximally connected clusters with nearly equal sizes (balanced). Think of the Fiedler vectors  $\{\sin(x - x_0)\}_{x_0 \in [0, 2\pi]}$  in the space of periodic functions  $L^2([0, 2\pi])$  and how the domain  $[0, 2\pi]$  is split by their positive and negative values (example in figure 5.1).

Maximal connection inside the two clusters implies also minimal connection through each other. Indeed, algorithms based upon the Fiedler vector are employed to find a so called *min-cut*<sup>6</sup> between balanced subgraphs, that is the smallest set of edges that needs to be “cut” (removed) to make the overall graph disconnected into two balanced clusters.

It turns out that the smaller the Fiedler value  $\lambda_1$  is, the less edges are in the balanced min-cut. Cutting (removing) progressively the edges of a balanced min-cut of a starting graph produces an increasingly smaller Fiedler value for the resulting graphs<sup>7</sup> until no more edges are left; since then the old Fiedler value becomes  $\lambda_0 = 0$

---

<sup>6</sup>Algorithms based on min-cut have many applications. For example, min-cuts help evaluating the robustness of transportation or communication networks identifying the most vulnerable connections. Other popular uses are in data clustering, like the detection of communities in social networks. The search for a min-cut, however, is a NP-complete problem because of the combinatorial nature of graph relations; therefore algorithms employing the Fiedler vector are actually only *heuristics* approximating the optimal solution.

<sup>7</sup>We are assuming that applying small changes to the graph, like removing an edge, do not change substantially the eigenspectrum. For large random graphs this is reasonable.

where now  $\mu_0 = 2$ , signalling the disconnection of the graph into two connected components.

The idea of min-cut is obviously related to the one of bottleneck. A measure of “bottleneckness” of a compact Riemannian manifold  $\mathcal{M}$  is given by the *Cheeger isoperimetric constant*  $h(\mathcal{M})$  defined as the minimal area of a hypersurface  $\partial A$  dividing  $\mathcal{M}$  into two disjoint pieces  $A$  and  $\mathcal{M} \setminus A$

$$h(\mathcal{M}) \equiv \inf \frac{\text{vol}(\partial A)}{\text{vol}(A)\text{vol}(\mathcal{M} \setminus A)}, \quad (5.26)$$

where the infimum is taken over all possible connected submanifolds  $A$ .

For a graph  $G = (V, E)$ , the Cheeger constant is usually defined by

$$h(G) \equiv \min \left\{ \frac{|\partial A|}{|A|} \mid A \subset V, |A| \leq \frac{|V|}{2} \right\}, \quad (5.27)$$

where  $\partial A$  is the set of edges connecting  $A$  with  $V \setminus A$ . The relation between bottleneckness and the Fiedler value for a graph  $G$  where all vertices have exactly  $d$  neighbours is encoded in the *Cheeger's inequalities*

$$\frac{1}{2}\lambda_1 \leq h(G) \leq \sqrt{2d\lambda_1}. \quad (5.28)$$

As we will show in 5.5.2, this property of the Fiedler value is interesting for the analysis of CDT geometries since it gives a quantitative measure of the presence of bottlenecks. Figure 5.1

### 5.2.2 Heat-kernel expansion and McKean-Singer coefficients

Higher eigenvalues possess also interesting geometrical content. To see how extract this information let us study again the random-walk/diffusion process on a connected graph  $G$

$$\begin{cases} \partial_t K_{v,v_0}(t) = -\frac{1}{a^2} \sum_{v' \in V} L_{v,v'} K_{v',v_0}(t) \\ K_{v,v_0}(0) = \delta_{v,v_0}, \end{cases} \quad (5.29)$$

where  $K_{v,v_0}(\tau)$  is the probability that a random walker starting from the vertex  $v_0$  at time  $t = 0$  is found at the vertex  $v$  at time  $t = \tau$ , and  $L$  is the Laplace-Beltrami matrix of  $G$ .

The solution of equation (5.29) is called the *heat-kernel*, and can be written in the Sturm-Liouville decomposed form

$$K_{v,w}(t) = \frac{1}{|V|} \sum_{\lambda_\alpha \in \sigma_G} \sum_{\nu=0}^{\mu_\alpha-1} e_{\alpha,\nu}(v) e_{\alpha,\nu}(w) e^{-\lambda_\alpha t}, \quad (5.30)$$

where all quantities are obtained from the Laplace-Beltrami matrix of the graph  $G$ . Notice that the terms in eq. (5.30) corresponding to larger eigenvalues are more suppressed for increasing times than terms corresponding to smaller ones. In particular, for times  $t \gg (\lambda_1)^{-1}$ , the only surviving term is given by the 0-th eigenvalue, and the probability distribution tends to be uniformly distributed amongst all vertices:  $\lim_{t \rightarrow +\infty} K_{v,v_0}(t) = \frac{1}{|V|} \forall v, v_0 \in V$ .

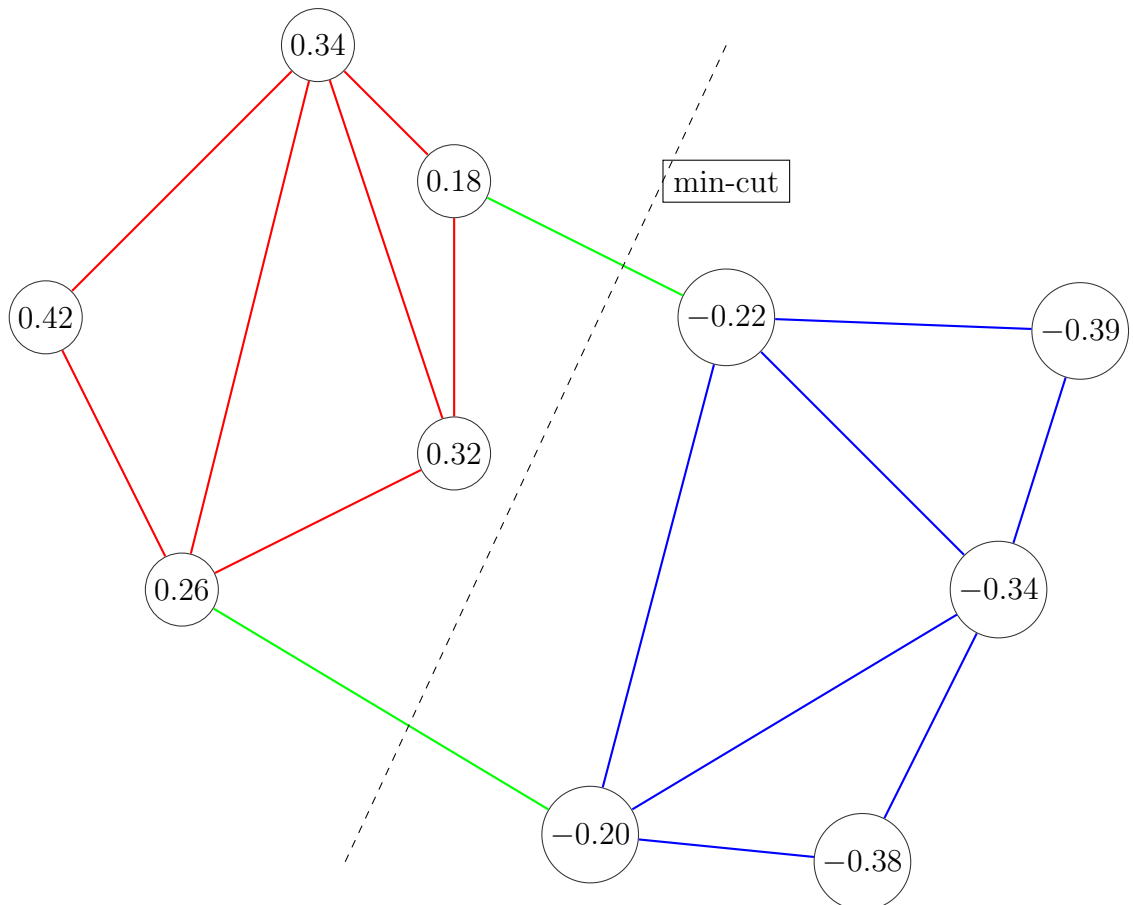


Figure 5.1: Min-cut of a graph, where the numbers on vertices are the (rounded) values of the Fiedler vector, with Fiedler value  $\lambda_1 \simeq 0.56$ . Notice that the sign of the Fiedler vector identify two clusters (red and blue), whereas the green edges, through which the sign flips, constitute the min-cut of the graph. Here each edge should be thought of the same length.

As already defined in 4.2.2, the *return probability*  $Z_{v_0}(t) = K_{v_0,v_0}(t)$  is the probability that a random walk comes back to the starting vertex  $v_0$  in a time  $t$ . Averaging over all starting vertices, the return probability reduces to  $Z(t)$ , the trace of the heat-kernel

$$Z(t) \equiv \text{Tr } K(t) = \sum_{v \in V} K_{v,v}(t) = \frac{1}{|V|} \sum_{\lambda_\alpha \in \sigma_G} \sum_{\nu=0}^{\mu_\alpha-1} \|\vec{e}_{\alpha,\nu}\|^2 e^{-\lambda_\alpha t} \quad (5.31)$$

$$\implies Z(t) = \frac{1}{|V|} \sum_{\lambda_\alpha \in \sigma_G} \mu_\alpha e^{-\lambda_\alpha t}, \quad (5.32)$$

where we used the decomposition in eq. (5.30) and the orthonormality of eigenvectors.

For later convenience we will denote by  $\sigma'_G \equiv \{\lambda'_n\}$  the set of eigenvalues where each eigenvalue  $\lambda_\alpha$  occurs exactly  $\mu_\alpha$  times, so that  $\lambda'_n \leq \lambda'_{n+1}$  and  $|\sigma'_G| = |V|$ .

Using the set  $\sigma'_G$  the return probability reads

$$Z(\tau) = \frac{1}{|V|} \sum_{n=0}^{|V|-1} e^{-\lambda'_n \tau}. \quad (5.33)$$

The return probability  $Z(\tau)$  can be nicely interpreted as a statistical *partition function*, for its formal analogy with the concept in statistical physics: the diffusion time takes here the role of the inverse temperature, while the eigenvectors and their associated eigenvalues take the role of microstates and their associated energies respectively.

In the case of a compact smooth manifold  $\mathcal{M}$ , for which the Laplace-Beltrami spectrum  $\{\lambda'_n\}_{n=0}^\infty$  is countable but unbounded, the averaged return probability density  $Z(\tau)$  can be asymptotically expanded in Laurent series for  $\tau \rightarrow 0^+$  in the following way ([26])

$$Z(\tau) = \frac{1}{\text{vol}(\mathcal{M})} \sum_{n=0}^\infty e^{-\lambda'_n \tau} = (4\pi\tau)^{-\frac{\dim(\mathcal{M})}{2}} \frac{1}{\text{vol}(\mathcal{M})} \left( \sum_{i=0}^{m-1} c_i \tau^{\frac{i}{2}} + O(\tau^{\frac{m}{2}}) \right). \quad (5.34)$$

First of all observe how the manifold dimension  $\dim(\mathcal{M})$  enters the expression. The return probability for unidimensional random-walks is  $\frac{1}{4\pi\sqrt{\tau}}$ , so it is reasonable for a smooth manifold to locally decompose the random motion along the  $\dim(\mathcal{M})$  directions and get the return probability as a product of independent unidimensional return probabilities. In the case of random walks on a torus  $T^d$  the return probability density equal to  $Z(\tau) = (4\pi\tau)^{-\frac{d}{2}}$  for small enough times, so one can infer the value of coefficients:  $c_0 = \text{vol}(\mathcal{M})$  and  $c_i = 0 \forall i \geq 1$ .

Corrections to the  $\tau^{-\frac{\dim(\mathcal{M})}{2}}$  behaviour must due to geometric properties characterizing the manifold under study.

For example, the first three coefficient have an intuitive interpretation, given by

McKean and Singer ([27])

$$c_0 = \text{vol}(\mathcal{M}), \quad (5.35)$$

$$c_1 = -\frac{\sqrt{\pi}}{2} \text{area}(\partial\mathcal{M}), \quad (5.36)$$

$$c_2 = \frac{1}{3} \int_{\mathcal{M}} R - \frac{1}{6} \int_{\partial\mathcal{M}} J, \quad (5.37)$$

where  $\partial\mathcal{M}$  is the (possibly empty) boundary of the manifold  $\mathcal{M}$ ,  $R$  is the scalar curvature of the manifold and  $J$  is the mean curvature of the boundary.

We expect that similar results hold for graphs approximating manifolds, but a first difficulty can be easily detected as shown by the following argument. At a time  $t$  only eigenvalues  $\lambda' \lesssim \frac{1}{\tau}$  contribute to the sum in eq.(5.34), but for  $t \rightarrow 0^+$  the full unbounded spectrum of the smooth manifold tends to contribute. The spectrum of a graph  $G$ , however, is bounded by the largest eigenvalue, so that here the expansion in eq. (5.34) is not numerically reliable for times  $\tau \lesssim (\lambda'_{|V|-1})^{-1}$ .

Nevertheless one can plot the return probability as a function of time and get an estimate of dimension  $d$  and coefficients  $\{c_i\}$  by extrapolation at  $\tau \rightarrow 0^+$ .

In the following sections we will explain how these ideas can be fruitfully applied to define the Laplacian-Beltrami spectral analysis on CDT.

### 5.3 Spectral graph analysis on Euclidean slices

First of all notice that, in CDT triangulations, every slice  $\Sigma$  is a 3-dimensional simplicial manifold where the maximal simplices are spatial tetrahedra with edges of equal size  $a$ . Each tetrahedron corresponds to a spatial volume element on the slice, and each of them is connected to exactly 4 other tetrahedra/volume elements. We consider the barycenter of a tetrahedron as a physical spatial point on the selected slice, and the straight path connecting the barycenters of two adjacent tetrahedra as a geodetic on the spatial manifold. In this way we can build an undirected graph  $G = (V, E)$  associated to a slice  $\Sigma$ , where  $V$  is the set of barycenters of tetrahedra, and  $E$  is the set of unordered pairs of vertices corresponding to the edges connecting them (see figure 5.2 for an example in 3-dimensional CDT). This construction is unique, and the resulting graph is dual to the simplicial manifold of the slice, since the geometric information given by adjacency relations between simplices is encoded on the edges.

Since each vertex has the same number of neighbours (the four adjacent tetrahedra), the resulting graph  $G$  is called *4-regular*.

From eq. (5.17) the Laplace-Beltrami matrix of the  $(d+1)$ -regular graph associated to a  $d$ -dimensional slice  $\Sigma$  is given by

$$L = (d+1)\mathbb{1}_{N \times N} - A, \quad (5.38)$$

where  $N$  is the total number of vertices, equal to the spatial volume or equivalently the number of tetrahedra of the slice  $\Sigma$ , and  $A$  is the adjacency matrix between

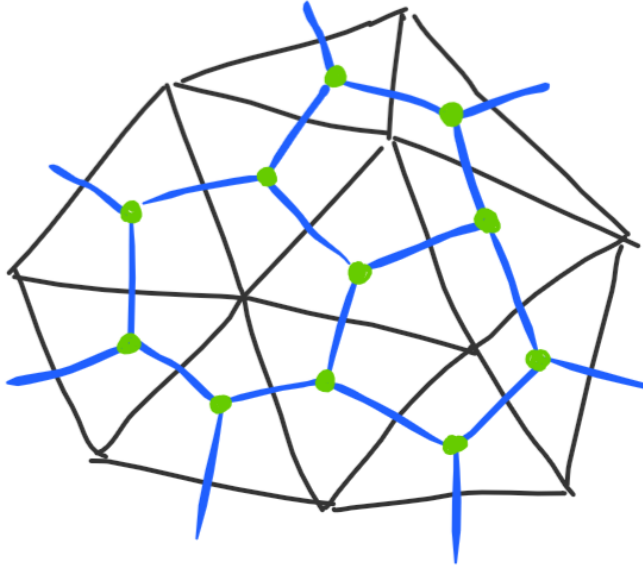


Figure 5.2: 2-dimensional triangulated spatial slice (black frame) and its dual graph. Vertices of the dual graph are represented by green dots on the triangle barycenters, whereas links are represented by blue lines. Since the geodesic distance between (adjacent) triangle barycenters is always the same ( $\frac{a}{\sqrt{3}}$ ), every link in the dual graph has the same length, and it is not required to assign weights to them.

vertices, representing adjacency relations between tetrahedra.

Notice that, since the degree matrix  $D$  is a multiple of the identity matrix,  $L$  and  $A$  have the same eigenvectors, and the eigenvalues of  $L$  are related to the ones of  $A$  by the simple identity

$$\lambda^{(L)} = d + 1 - \lambda^{(A)}. \quad (5.39)$$

So, in our case, it is convenient to compute eigenquantities of the adjacency matrix  $A$  and then apply eq. (5.39) to get the spectrum of  $L$ . Furthermore, the matrix  $A$  is *sparse* and therefore can be stored and manipulated efficiently by numerical routines: each row contains exactly  $(d+1)$  ones and  $N-(d+1)$  zeroes, so the total number of non-zero elements is  $N(d+1) \ll N^2$  (for typical CDT simulations in 4D, slices have  $d=3$  and  $N \in [5, 3000]$ ).

Furthermore, to study geometries at large scales it is sufficient to analyze truncated spectra, where only the first eigenvalues and eigenvectors are actually computed; this results in a further speed-up of the numerical routine.

In our analyses we firstly preprocessed the triangulation data structures (A) in order to obtain a new manageable data structure consisting of a set of graphs associated to the spatial slices in the form of adjacency lists<sup>8</sup>. In this process, information about how spatial tetrahedra are connected must be reconstructed, since the triangulation data structure employed during simulations do not contain explicitly any tetrahedral data.

---

<sup>8</sup>The *adjacency list* representation of a graph is a set of the form  $\{\mathcal{N}(v_i)\}_{i=0,\dots,|V|-1}$  where the  $i$ -th element is the set of vertices  $\mathcal{N}(v_i)$  adjacent to the vertex  $v_i$ . Adjacency lists and adjacency matrix are two different but equivalent ways to encode graph information, the first being significantly more space-efficient than the latter for sparse graphs.

Secondly, the C++ library ‘‘Armadillo’’ [28], with ARPACK and SuperLU support, has been used for the computation of the eigenvalues and an orthonormal base of eigenvectors  $\mathcal{B}_G$  for the (sparse) adjacency matrix associated to each slices<sup>9</sup>. The spectra of the Laplace-Beltrami matrices  $\sigma'_G$  are then simply obtained by using eq. (5.39).

## 5.4 An alternative derivation of the spectral dimension

In subsection 4.2.2 we discussed the computation of the spectral dimension as a diffusion process on the triangulations and on the slices.

Here we will propose an alternative derivation of the spectral dimension on spatial slices by using the spectrum of the associated Laplace-Beltrami matrix. The two methods must be consistent, since both are strictly related to the asymptotic behaviour of the heat equation (4.10).

Before considering CDT configurations, we made consistency tests of this computation for simple and well-known cases, namely graphs representations of  $n$ -dimensional torus  $T^n \cong \bigtimes_{i=1}^n S^1$ . This will also help to explain how the method can be applied in general cases.

### 5.4.1 Spectral dimension for simple cases

Let us start with the graph corresponding to an unidimensional torus  $LT^1 = LS^1$  with length  $L$ , a ring of  $N$  vertices spaced by a length  $a = \frac{L}{N}$ . The components of its Laplace-Beltrami matrix are given by (see eq. (5.20))

$$L_{i,j}^{(S^1)} = 2\delta_{i,j} - \delta_{i,(j+1) \bmod N} + \delta_{i,(j-1) \bmod N}. \quad (5.40)$$

The eigenproblem  $L^{(S^1)}\vec{e} = \lambda\vec{e}$  can be solved analytically in exact form or by the aforementioned numerical routine, both resulting in the spectrum

$$\sigma'_G = \{\lambda'_s = 4\sin^2\left(\frac{\pi s}{N}\right)\}_{s=0,\pm 1,\dots,\pm \frac{(N-1)}{2}}, \quad (5.41)$$

where, for simplicity, we assumed  $N$  odd.

The blue pluses in figure 5.3 shows a visualization of the spectrum of eigenvalues (with repetitions)  $\sigma'_G = \{\lambda'_m\}_{m=0}^{N-1}$ , obtained numerically from the Laplace-Beltrami matrix of the ring graph. Notice that spectra are merely sets: the labeling of the spectrum in eq. (5.41) is arbitrary, and it does not correspond necessarily to the one obtained by numerical means, since the routine always puts them in non-decreasing

---

<sup>9</sup>The time of computations to get the full spectrum of eigenvalues and associated eigenvectors of all the slices from a configuration in the de Sitter phase with spatial volume fixed by  $N_4^{(4,1)} = 80k$  is about 1 minute in a workstation with an AMD FX-6300 processor. If one is interested only in the first 20 smaller eigenvalues and associated eigenvectors, the time reduce considerably, going to about 0.2 seconds for configuration.

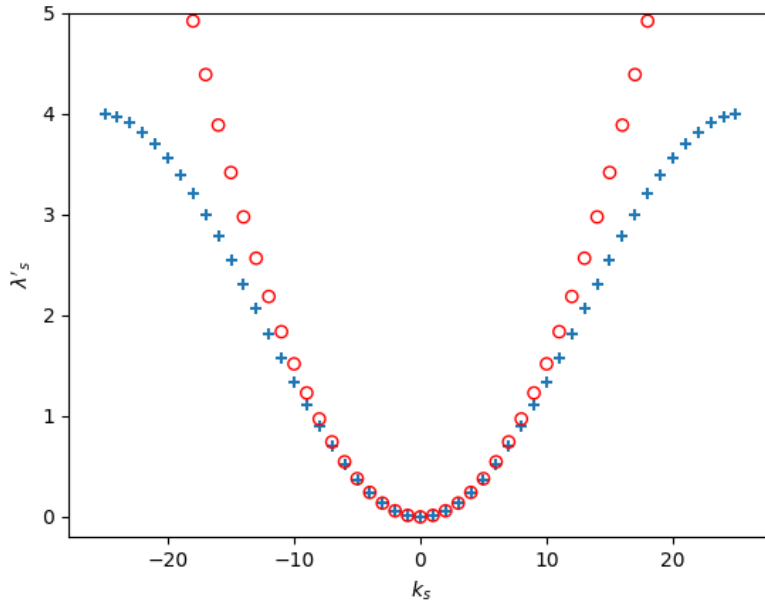


Figure 5.3: Comparison between the spectrum from the discrete ring with  $N = 51$ ,  $L = 2\pi$  and  $k_s = \frac{2\pi s}{L}$  (blue pluses) and the spectrum of the continuous ring (red circles), appropriately normalized with a factor  $-a^2 = -(\frac{L}{N})^2$  (see text).

order  $\lambda'_m \leq \lambda'_{m+1}$ . However, for the sake of comparison, we disposed the eigenvalues from both spectra following the labeling like in eq. (5.41), where for the abscissa we used the variable  $k_s \equiv \frac{2\pi s}{Na} = \frac{2\pi s}{L}$ .

The reason for this choice is that it makes manifest how to interpret the continuum limit  $N \rightarrow +\infty$  with  $Na = L$  fixed. Indeed, now the eigenvalues can be written as  $\lambda'_s = 4 \sin^2(\frac{k_s a}{2})$  where  $k_s \in \{0, \pm \frac{2\pi}{L}, \pm 2\frac{2\pi}{L}, \dots, \pm \frac{(N-1)}{2}\frac{2\pi}{L}\}$ . Taking the limit  $N \rightarrow +\infty \implies a \rightarrow 0$  we see that eigenvalues  $\lambda'_s$ , get closer and closer but are always bounded from above by 4.

From the relation eq. 5.15 between the matrix and continuous forms of the Laplace-Beltrami operator we know that the two types of eigenvalues differ by a factor  $-a^2$ , so that the eigenvalues associated to the continuous torus must be obtainable from the continuum limit

$$-\frac{\lambda'_s}{a^2} = \frac{4}{a^2} \sin^2\left(\frac{k_s a}{2}\right) = -\left[\frac{\sin(\frac{k_s a}{2})}{(\frac{k_s a}{2})} k_s\right]^2 \xrightarrow[a \rightarrow 0]{} -k_s^2, \quad (5.42)$$

since  $\frac{\sin(x)}{x} \xrightarrow[x \rightarrow 0]{} 1$ . For  $L = 2\pi$  we have  $k_s = s \in \mathbb{Z}$ , and the eigenvalues  $\lambda'_s = -s^2$  correctly reproduce the ones computed previously from the heat equation on the circle (5.1).

Notice that the parabolic behaviour  $k^2$  of eigenvalues in the continuum case (red circles in figure 5.3) is exactly the lowest order approximation of the discrete case one  $\frac{\sin^2(ka/2)}{a^2/4} = k^2 + O(k^6)$ , so we should consider the difference between the two cases merely as a finite-size effect; as a matter of fact, the biggest difference comes from higher-valued eigenvalues ( $k \gg a^{-1}$ ), since they capture indeed microscopic features of the lattice.

So only the first eigenvalues are reliable in the computation of large-scale features

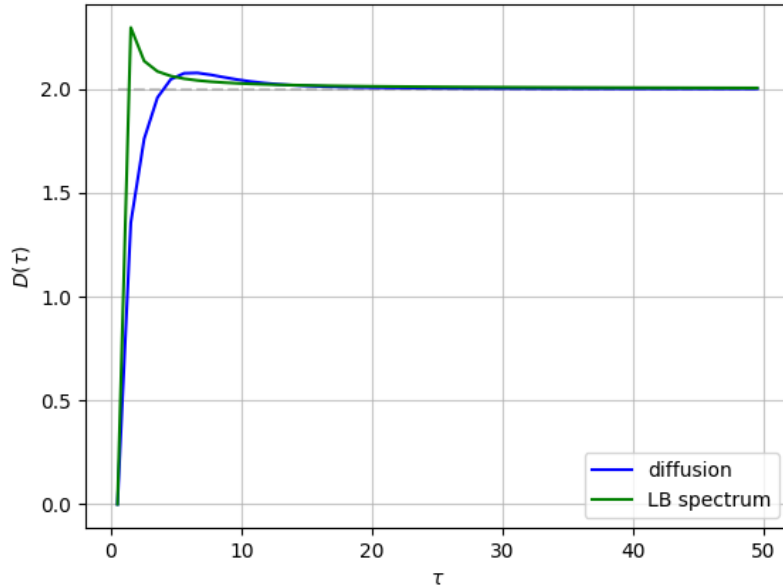


Figure 5.4: Plot of the spectral dimension function  $D(\tau)$  of a 2-torus graph with  $N = 2601 = 51 \times 51$  sites, using different definitions of return probability: by the sum (5.33) with Laplace-Beltrami eigenvalues (green line), or by a diffusion process with rate factor  $\eta = 0.6$  (blue line). The asymptotic dimension is represented by the grey dashed line.

in the continuum limit.

Similar considerations apply for graphs representing  $n$ -tori ; obtained their associated spectra, we want to show now how to compute their spectral dimension.

From the expansion in eq. (5.34) we can get an estimate the dimension of the manifold approximated by the graph:

$$D(\tau) = -2 \frac{d \log Z(\tau)}{d \log \tau}, \quad (5.43)$$

where the return probability  $Z(\tau)$  is computed from eigenvalues, by employing the definition given in eq. (5.33).

Notice that this expression is the same of the one used in subsection 4.2.2, with the difference that there the return probability came from an average of explicit diffusion processes on the graph.

Figure 5.4 compares the behaviors in time  $\tau$  of spectral dimensions obtained by using the two methods for a torus graphs in 2 dimensions. We see that both methods give a consistent answer, that is the actual dimension of the smooth manifold they are approximating, only for times sufficiently away from zero, signaling that the lower values of  $D$  for small diffusion times  $\tau$  is due to finite-size effects. From this observation we wonder if the dimensional reduction effect, observed in CDT and discussed in subsection 4.2.2, continues to hold in a hypothetical continuum limit. Since for large times  $\tau$  only lowest eigenvalues ( $\lambda \lesssim \tau^{-1}$ ) contribute to the return probability, it is sufficient to compute only the first eigenvalues of the Laplace-Beltrami matrix and sum over this truncated spectrum: this speeds up numerical computations, and do not affect the reliability of the spectral dimension estimate for

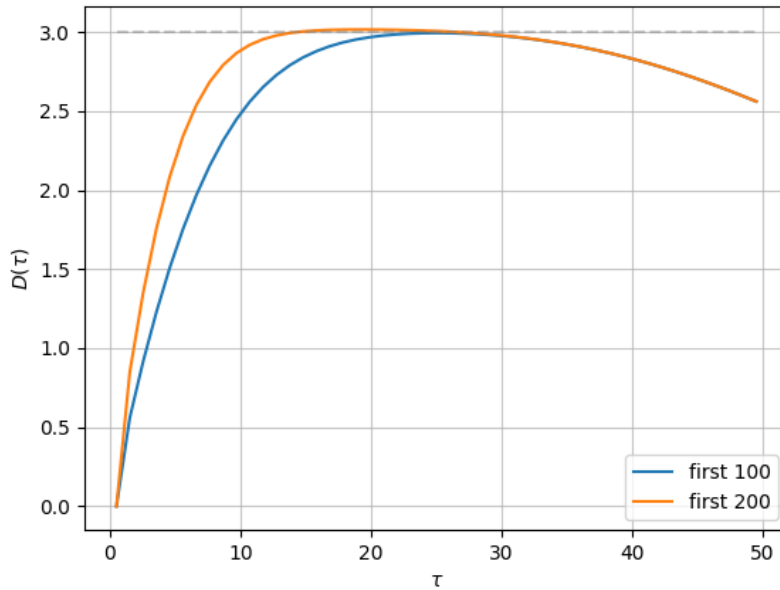


Figure 5.5: Plot of the spectral dimension function  $D(\tau)$  of a 3-torus graph with  $N = 29791 = 31 \times 31 \times 31$  sites, using eq. (5.33) truncated to the first 100 eigenvalues (blue line) and to the first 200 eigenvalues (orange line) of the Laplace-Beltrami matrix. The asymptotic dimension is represented by the grey dashed line.

times  $\tau$  sufficiently far from zero, as shown in figure 5.5 for two different truncations of the 3-torus graph spectrum.

Of course, for too large times the expansion (5.34) fails and the spectral dimension must tend to zero, since the return probability tends to a constant. Therefore, exactly as it happened in subsection 4.2.2, the asymptotic continuous spectral dimension must be extrapolated as the value taken by the function  $D(\tau)$  in a plateau, for a certain reliable time range  $[\tau_{\min}, \tau_{\max}]$ .

### 5.4.2 Spectral dimension of spatial slices in CDT

Having explained the methods of spectral dimension extraction for simple cases, and given some insight on the interplay between continuum structures and their discrete counterparts, we can finally move to the spectral analysis of slice geometries in CDT. The statistical sample of slices  $\{\Sigma_i\}$  employed for this check are slices near the center of volume of independent configurations in the de Sitter phase ( $k_0 = 2.2$ ,  $\Delta = 0.6$ ). For each slice  $i$  in the sample we repeat the same procedure applied above for the tori, that is we compute the truncated spectrum of eigenvalues of the Laplace-Beltrami matrix of its associated graph  $G_i$ . Subsequently we compute the return probabilities using eq. (5.33) and take the average over the slice sample (by means of resampling methods to estimate errors). Concurrently we compute the return probabilities from diffusion processes (with rate factor  $\eta < 1$ ) on the slices and averaged for different starting points.

The results of the two methods are compared in figure 5.6. For both there is good agreement (even if for different time ranges) with the value of the asymptotic dimension  $d$ , but this value seems unexpected at first sight. From a graph approximating

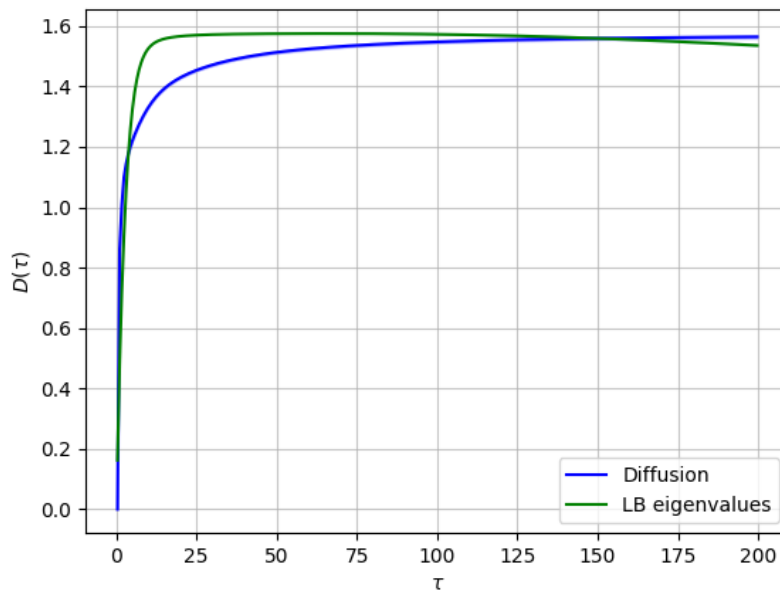


Figure 5.6: Plot of the spectral dimension function  $D(\tau)$  of slices near the center of volume from 400 independent configurations in the de Sitter phase and for spatial volumes  $N_4^{(4,1)} = 80k$ , using the two methods discussed in the text: by truncating to the first 200 Laplace-Beltrami eigenvalues (green line), or by a diffusion process with rate factor  $\eta = \frac{2}{3}$  (blue line).

the smooth 3-dimensional sphere we would expect obviously an asymptotic dimension  $d = 3$ . Instead we get almost half of the expected value  $1.5 \lesssim d \lesssim 1.6$ .

This result seems discouraging at first, but the reason of this effect seems related probably to the fractal structure of slices.

For example, the position of random walkers for  $m$ -dimensional diffusion processes in porous media is typically distributed with a variance  $\sigma^2$  not proportional to the diffusion time  $t$ , but to some fractional power  $t^\gamma$  with  $0 < \gamma < 1$ , so that the asymptotic dimension would be  $d = \gamma m$ .

Furthermore, compared to the spectral dimension for full spacetimes (figure 4.10), the behaviour of the spectral dimension of slices, shown in figure 5.6, seems to reach a plateau already for small diffusion times, indicating a small scale dependence, and therefore suggesting a fractal structure of spatial slices.

Unlike smooth manifolds, for disordered systems there are no meaningful concepts of tangent space and basis of directions which can be counted, not even at large scales. For the  $d$ -torus graphs discussed previously this phenomenon did not arise, since they are ordered and highly symmetric with respect to the group of translations, isomorphic to  $(\mathbb{Z}_l)^d$  (where  $d$  is the number of generators and  $N = l^d$  is the number of sites), so the concept of directions and tangent space can be defined and is meaningful in the continuum limit.

For spatial slices the anomalous diffusion cannot be due to lacunarity as in porous media, since their topology is always constrained to be the same of  $S^3$ . The only explanation to behaviour is the emergence of an effective porous structure in the form of bottlenecks.

The presence of bottlenecks in spatial slices was already pointed out by Görlich in [18], where the qualitative geometrical structure of slices is questioned.

Here we want to employ spectral graph methods to make a quantitative analysis of these structures.

As discussed in 5.2.1, information about the “bottleneckness” of a graph is contained in the Fiedler value and vector. In the following sections we will discuss further the geometrical structure of slices by studying eigenvectors and the distributions of eigenvalues.

## 5.5 Visualizing large-scale structures: Laplacian eigenmaps

While eigenvalues are useful to identify characteristic scales of the manifold or graph, eigenvectors contain information about the relative location of vertices, and can actually be employed to “visualize” the large scale structure by means of the technique of *Laplacian embedding* [29], which we will introduce here.

Laplacian embedding is a way of representing graphs in a  $k$ -dimensional (Euclidean) space, and consists in the solution to the following optimization problem:

$$\min_{\vec{f}^1, \dots, \vec{f}^k} \left\{ \sum_{(v,w) \in E} \sum_{s=1}^k [f^s(v) - f^s(w)]^2 \quad | \quad \vec{f}^s \cdot \vec{f}^p = \delta_{s,p}, \vec{f}^s \cdot \vec{1} = 1 \quad \forall s, p = 1, \dots, k \right\}, \quad (5.44)$$

where for each vertex  $v \in V$  the value  $f^s(v)$  is its  $s$ -th coordinate in the embedding<sup>10</sup>.

The interpretation of such minimization is that optimal coordinates should be independent (first constraint) and describe close points by close values, excluding obviously the uniform vector (second constraint).

Notice that, for  $k = 1$ , this minimization problem reduces to the one in eq. (5.25), meaning that the Fiedler vector  $\vec{e}_1$  is the optimal embedding of the graph on a line, as could have already been inferred from the discussion in 5.2.1. Indeed, the set of vectors  $\{\vec{f}^1, \dots, \vec{f}^k\}$  solving eq. (5.44) are exactly the first  $k$  (non-uniform) eigenvectors  $\{\vec{e}_1, \dots, \vec{e}_k\}$  of the Laplace-Beltrami matrix, and we will refer to this set as a  $k$ -dimensional *Laplacian eigenmap* of the graph.

For example, we can map vertices of a graph (or points of a manifold) on a 2-dimensional square by making a scatter plot of the set of coordinatized vertices  $\{(e_1(v), e_2(v))\}_{v \in V}$ , where  $\vec{e}_1$  and  $\vec{e}_2$  are the first 2 eigenvectors of the Laplace-Beltrami matrix (recalling that  $\vec{e}_s \equiv (e_s(v))_{v \in V}$ ).

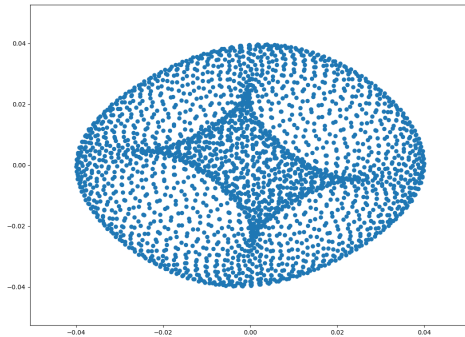
However, if  $k$  is lower than the dimension in which the graph or manifold can be embedded, distinct points could have the same coordinates. Nonetheless, this maps are effective in implementing a *Nonlinear dimensionality reduction*, where high-dimensional data is represented in a lower-dimensional space, and are extensively

---

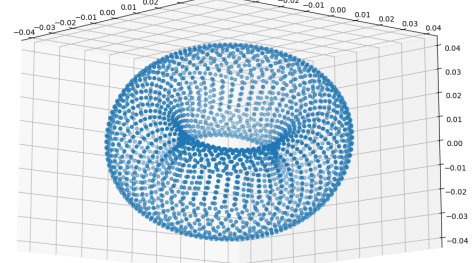
<sup>10</sup>In topology, an *embedding* is an injective continuous map between topological spaces. However, the maps obtained as Laplacian embeddings are usually not injective, and the most appropriate term would then be *Laplacian eigenmaps*.

employed in the context of machine learning.

### 5.5.1 Example: eigenmaps of tori



(a) 2D eigenmap of a 2-torus.



(b) Perspective projection of the 3D eigenmap of a 2-torus.

Figures 5.7a and 5.7b show the 2-dimensional and 3-dimensional Laplacian eigenmaps of a 2-dimensional torus represented by a periodic square-grid graph. Notice that, in the 2-dimensional eigenmap (figure 5.7a), some vertices are mapped to the same point in the square. This is expected, since a 2-dimensional torus, cannot be embedded on a 2-dimensional surface with the topology of a disc (otherwise it would be a disc!); nonetheless, in figure 5.7b, the points are arranged in a way that makes the familiar shape of the torus easily recognizable to the eye, and the same shape can be recognized with little effort also for the 2D map.

The 3-dimensional map in figure 5.7b is a true embedding, that is distinct points have all distinct coordinates (but this obviously cannot be shown by a figure, being planar).

Furthermore, the 2D map is the orthographic projection of the 3D map in the plane of the first and second directions (first two eigenvectors), so figure 5.7a can be interpreted as a view of the 3D object in figure 5.7b from above. It is somewhat surprising that, merely from the adjacency relations between abstract vertices and computing the first 3 non-null eigenvectors, a computer is able to represent the structure of a torus in a way pretty much similar to how a human would have drawn it on a sheet of paper!

Since spatial slices have topology  $S^3$ , they certainly cannot be embedded faithfully using a 3D eigenmap. Figure 5.8 should give an idea of how a smooth manifold, non-embeddable in 3 dimensions (here a 3-torus), looks like when represented with a 3D eigenmap.

### 5.5.2 2D and 3D eigenmaps of a spatial slice

Table 5.1 shows the 2-dimensional and 3-dimensional Laplacian eigenmaps for spatial slices near the center of volume for a typical configuration in the de Sitter phase

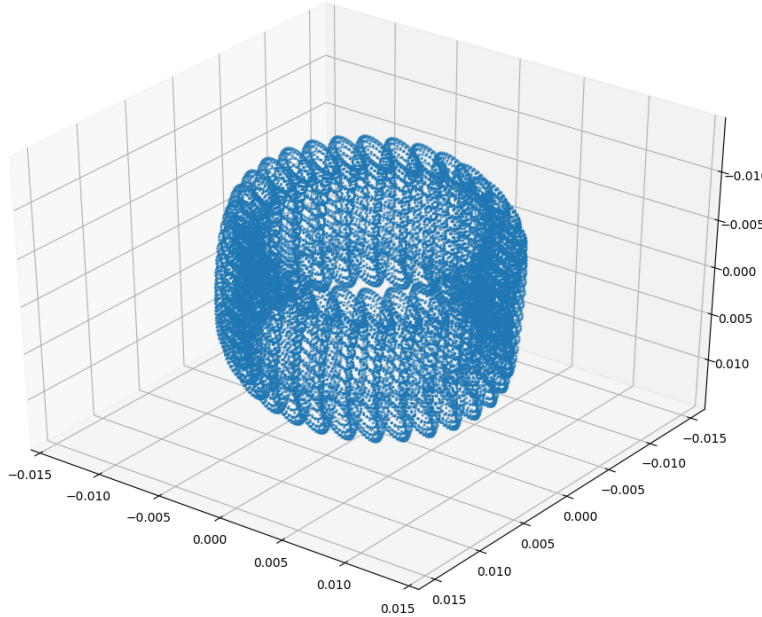


Figure 5.8: 3D eigenmap of a 3-torus graph with  $30 \times 30 \times 30 = 27k$  points. Notice that, from this perspective, the figure looks like many 2-tori ( $T^2 \cong S^1 \times S^1$ ) placed in a circle ( $S^1$ ); is it no coincidence since  $T^3 \cong S^1 \times S^1 \times S^1 \cong T^2 \times S^1$ .

( $k_0 = 2.2$ ,  $\Delta = 0.6$ ) and with total spatial volume fixed by  $N_4^{(4,1)} = 80k$ ; the column  $t_r$  specify the distance in time with respect to the slice nearest to the center of volume ( $t_r = 0$ ), and, to ease the visualization of the 3D structures, vertices have been colored according to the values of the Fiedler vector (recall the discussion in 5.2.1).

No familiar structures seem to be recognizable from these plots, but one can notice that points distribute mainly along “filaments”, even in the 3D eigenmap. By the simplicial manifold constraint (discussed in 3.1) the volume elements of a spatial triangulation cannot overlap, so the only reasonable explanation is that first three eigenvectors are not capable to describe the internal structures of those regions, since geometrical informations at shorter scales (higher eigenvalues) is required.

It is apparent that the filaments are scarcely connected with the rest, signalling the presence of bottlenecks, but we cannot tell how volume is distributed inside them. In fact, the spatial slices are euclidean, and there could be some connection with the *branched polymer phase* of Euclidean Dynamical Triangulation.

From the average spatial volume distribution of configurations in the de Sitter phase (see 4.2), fitting well with the one resulting from a  $S^4$  geometry, one could have hoped that the geometry of spatial slices would be the one of a  $S^3$  sphere on large scales, but this is not what we observe here by means of the eigenmaps (and the spectral dimension).

Recall from 3.1 that the Fiedler value is related to the presence of bottlenecks, and the Fiedler vector gives an heuristic algorithm to compute the optimal balanced

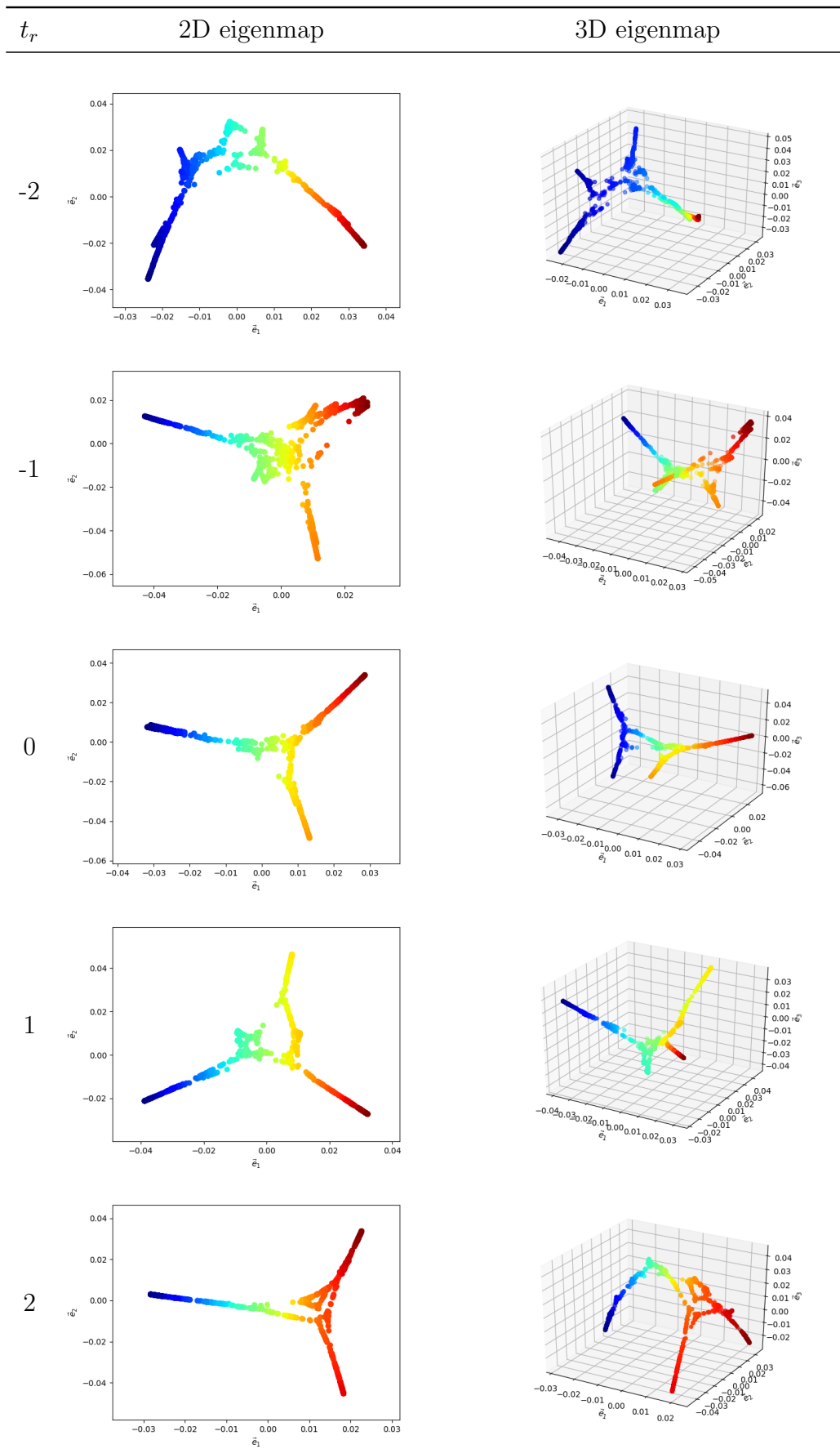


Table 5.1: 2D and 3D eigenmaps of spatial slices (see text for description).

min-cut. Indeed, we can use the idea of min-cut to disconnect the graph into two clusters and repeat the procedure on each of them independently. As the example in figure 5.1, all the links for which the Fiedler vector change sign form the min-cut of the graph, which disconnects the vertices with negative value of the Fiedler vector from the ones with non-negative value. If the min-cut is sufficiently small (recall the inequalities (5.28)), we can treat each component as almost disconnected from the other, so the geometric information about their structure, obtained by computing eigenvalues and eigenvectors on them independently, is plausibly reliable. Figure 5.9

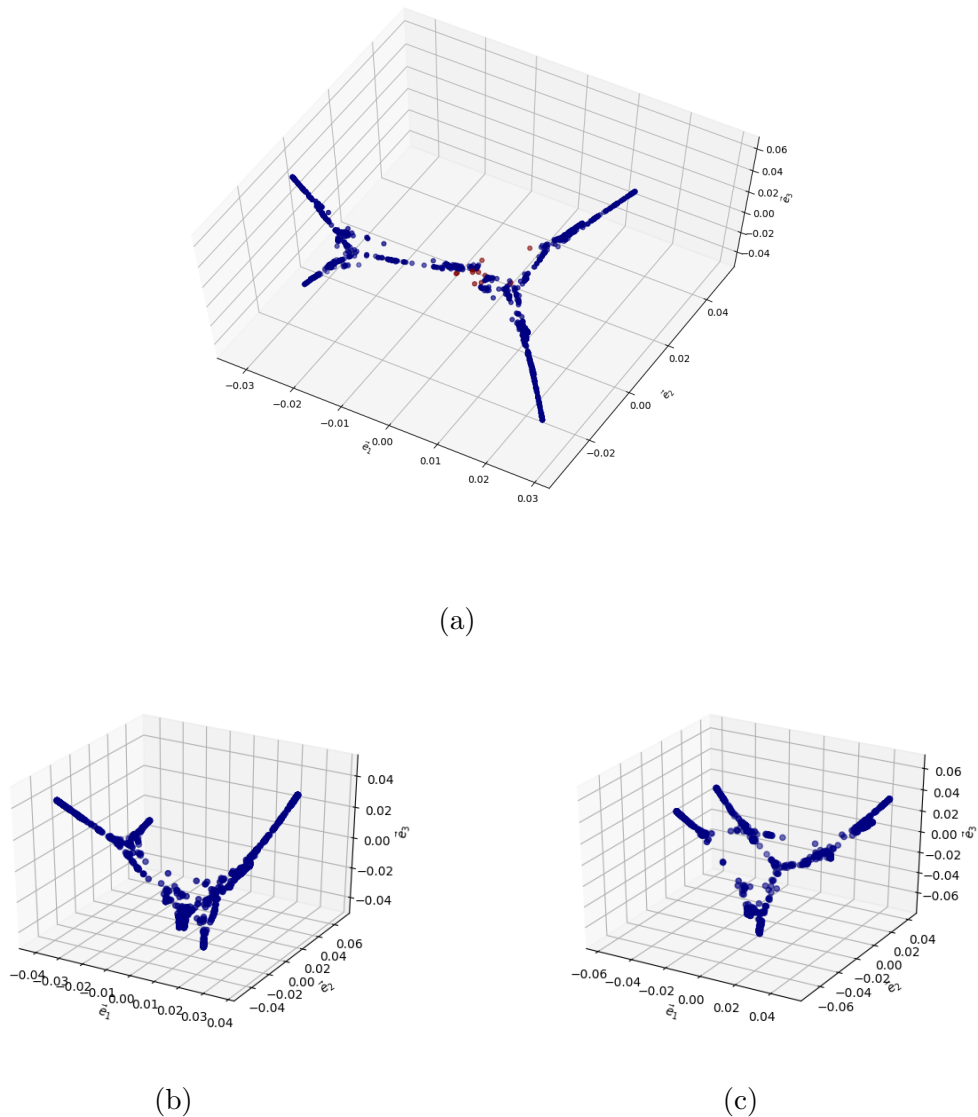


Figure 5.9: 3D eigenmaps and cutted components of the same slice with  $t_r = 0$  in table 5.1.

[figure a]: 3D eigenmap of the original graph (2642 tetrahedra), where vertices of links in the min-cut (14 links) has been highlighted by red.

[figures b and c]: 3D eigenmaps of subgraphs disconnected by the min-cut, with respective volumes of 1602 and 1040 tetrahedra.

shows the procedure outlined above for a single slice, where the 3D eigenmaps for

the disconnected components have been computed from the Laplace matrices on the respective subgraphs.

Also the resulting components appears to possess filamentous structures, indicating that the whole slice structure is somewhat self-similar like a fractal. In principle, further resolution could be obtained by repeating the procedure recursively on subgraphs<sup>11</sup>.

Here the fractality of slices should not come as surprise, since we have already shown that their spectral dimension is fractional and almost constant for a wide range of diffusion times.

One may wonder how this observation conciliates with the geometry of the full spacetime, where the asymptotic dimension is near the one expected from a smooth manifold.

The question could probably be answered only after having generalized the Laplace-Beltrami approach to full spacetimes (see 5.8), but one could make some educated guesses.

The simplest scenario that may come to mind is that pentachorons on slabs connect tetrahedra which would appear far in the slice, for example residing on different filamentous structures. These shortcuts would allow the random walkers of the 4-dimensional diffusion process to appear almost freely jumping between tetrahedra in the slice<sup>12</sup>.

So, the geometry of spatial slices could be merely unphysical, and comparing it with a slicing of  $S^4$  meaningless.

What is left to verify is the eventuality that the fractal structures of spatial slices could be somewhat correlated. If some correlation between geometric structures of neighbouring slices is present, this could only means that the spacetime must propagate them, and therefore its geometry would results affected in turn.

The eigenmaps in figures in 5.1 do not show particular similarities in the disposition of filamentous structures of neighbouring slices (even if the 2D eigenmaps could deceive). However, the optimal embedding for graphs with similar structures but different internal volume distributions might result in drastically different eigenmaps. Furthermore, these figures are based upon a single configuration, and we would to verify if such occurrence is true *on average*.

It is not clear how to define an average from the first eigenvectors of different configurations and slices, since, among other things, the are defined in spaces with different dimensions in general.

Nevertheless, some progress could be made by averaging the correlations between fluctuations in the first eigenvalues of neighbouring slices. This will be explained and analyzed in the following section.

To conclude the discussion about eigenmaps, we applied the same method to the maximal slice of a configuration in the  $B$  phase, resulting in figure 5.10. Here no filamentous structures emerge, and the vertices seems to be well distributed in

---

<sup>11</sup>This procedure is called *spectral clustering*, and its commonly used in in image segmentation (e.g., for medical purposes), where an automatic simplification into substructures for the object under analysis is required.

<sup>12</sup>We are considering the projection of the spacetime diffusion process onto slices, where each tetrahedron is associated to a  $(4, 1)$  pentachoron on the slice above or  $(1, 4)$  pentachoron on the slice below.

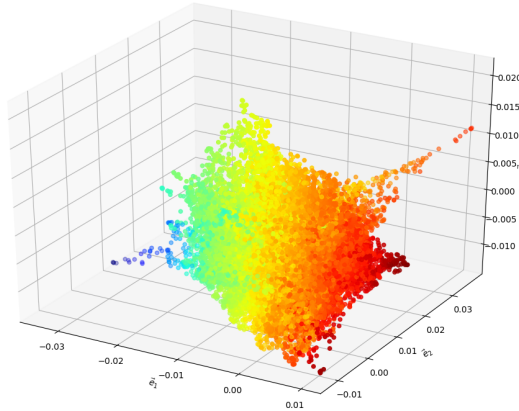


Figure 5.10: 3D eigenmap of the maximal slice well inside the  $B$  phase: ( $k_0 = 2.2, \Delta = -0.2$ ). The spatial volume of the configuration is completely concentrated in this slice, and the number of vertices in the graph is (almost)  $N_{3s} = \frac{N_4^{(4,1)}}{2} = 40k$ . The coloring is based upon the computed Fiedler vector.

space, and apart from some small bump, enhanced by the eigenmap coordinates. The procedure, outlined above, of cutting recursively the slices and analyzing the substructures, is meaningless here, since the min-cut found on the initial slice has a size of  $|\partial A| \simeq 5k$ , where  $A$  is one of the subgraphs that would be disconnected, and  $\partial A$  is the set of links that connect it to the complement  $G \setminus A$ , that is the min-cut. The resulting subgraphs  $A$  and  $G \setminus A$  have approximately half the volume of the original graph  $G$ , that is  $|A| \simeq 20k$ , so that the estimate<sup>13</sup> to the Cheeger constant<sup>14</sup> of this graph (recall the definition (5.27)) is very high, namely  $\tilde{h}(G) \simeq \frac{1}{4} = 0.25$ . Since the computed Fiedler value is  $\lambda_1 = 0.11$ , in this case the Cheeger inequalities (5.28) are satisfied by our estimate:

$$\frac{1}{2}\lambda_1 \simeq 0.05 \leq \tilde{h}(G) \leq \sqrt{8\lambda_1} \simeq 0.9. \quad (5.45)$$

The *spectral gap*  $\lambda_1 - \lambda_0 = \lambda_1$  computed for maximal slices of  $B$  phase configurations is much higher than the one one computed for slices of  $C$  phase configurations (e.g., see the histograms in figure 5.12); this means that  $\lambda_1$ , in the center of volume for example, could be actually used as order parameter for the  $C|B$  transition.

Another noteworthy fact, is that the first four (non-null) eigenvalues are very similar and approximately equal to  $\lambda_{1,2,3,4} \simeq 0.11$ . This quasi-degeneracy tells us that the first four eigenvectors, describing the largest scales, could be approximately treated as element of the same eigenspace with dimension 4, meaning that the system is quasi-isotropic in space. However, higher eigenvalues are not distributed into multiplets as would be expected from a  $S^3$  (see equation (5.8)), but seem to be continuously distributed over the gap. Furthermore, a computation of the spectral

<sup>13</sup>Remember that the spectral min-cut does not always coincides with the actual min-cut of the graph, but is an heuristic algorithm that tries to solve a relaxation of an NP-complete problem.

<sup>14</sup>Also called *algebraic connectivity*, since it quantifies how much connected a graph is.

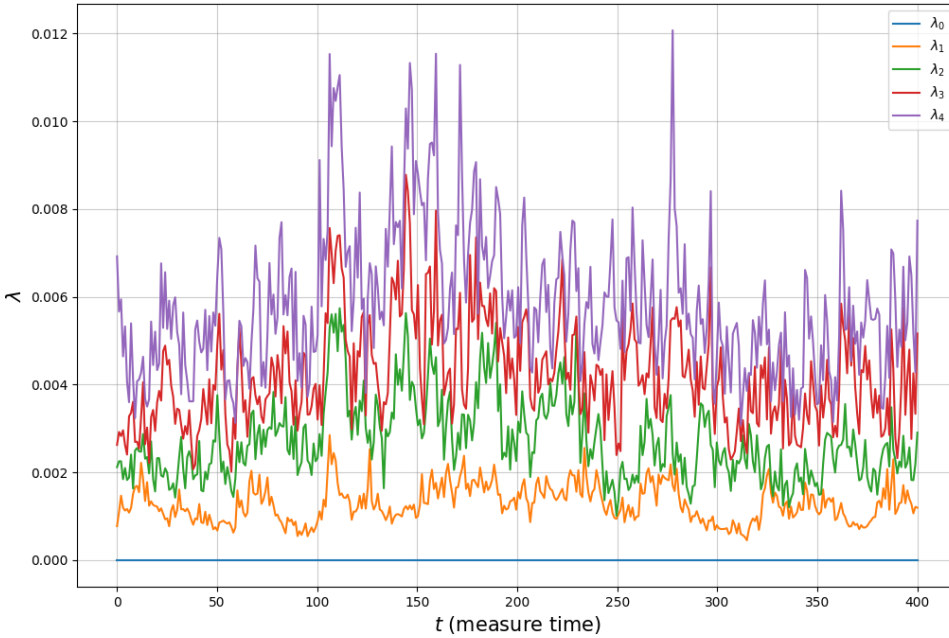


Figure 5.11: Histories of the first 5 smaller eigenvalues of a specific slice time  $t_r$  and for configurations, very correlated in simulation-time (spaced by only  $1M$  steps). De Sitter phase with volume fixing  $N_4^{(4,1)} = 80k$ .

dimension points out a dimension much higher than 3 and pretty dependent on the diffusion time (we hope to offer a more detailed analysis in future works).

Our interpretation of the results obtained is that the  $C|B$  transition in CDT is very much similar to the transition between the branched polymer phase and the crumpled phase that occurs in the phase diagram of Euclidean Dynamical Triangulations (DT) [30], at least from the point of view of spatial slices.

In DT, all transitions are found to be first order, while the  $C|B$  transition in CDT seems to be second order, at least using  $\text{conj}(\Delta)$  as order parameter. It would be interesting to investigate the behaviour of the spectral gap<sup>15</sup>  $\lambda_1$  as order parameter of the  $C|B$  transition in CDT.

## 5.6 Analysis of the spectra of eigenvalues

In this section we will discuss some properties of the spectrum of eigenvalues of spatial slices from numerical simulation well inside the de Sitter phase: ( $k_0 = 2.2$ ,  $\Delta = 0.6$ ), with spatial volume fixed by  $N_4^{(4,1)} = 80k$  and  $T = 80$  slices.

First of all, notice from figure 5.11 that the histories of the first eigenvalues associated to a particular slice time seem correlated also in simulation time, especially for the smallest eigenvalues like the Fiedler value. Secondly, there it seems to be a correlation in the fluctuations of different eigenvalues in simulation time, especially

<sup>15</sup>computed in the slice of center of volume for example.

the larger ones.

These observations has to be expected, since the algorithm performs local updates of the triangulation, and this reflects on the different rates of change at different scales, the larger one identified by  $|\lambda_1|^{-\frac{1}{2}}$ .

To conclude the discussion about spatial slices and their geometric significance in the de Sitter phase, we found useful to test the eventuality that the fluctuations of the smaller eigenvalues in the spectrum, encoding large scale features of the geometries (like the amount of bottlenecks), are correlated in the *slice time* direction (non simulation-time), signalling the possibility that the fractal structure of slices propagates along the spacetime or not.

### 5.6.1 Correlation of eigenvalues in the slice time direction

Let us consider a sample of independent configuration  $\{\mathcal{T}_i\}_{i=1}^M$ , which have been aligned in such a way that the slice at time  $t_r = 0$  is always the nearest to the center of volume.

We will denote by  $\lambda_\alpha(t_r, \mathcal{T}_i)$  the  $\alpha$ -th smaller eigenvalue computed on the slice with time label  $t_r$  from the center of volume of the configuration  $\mathcal{T}_i$ . The quantity in which we are interested is the fluctuation of the smallest  $\alpha$ -th eigenvalue for each slice time  $t_r$ , that is

$$\delta\lambda_\alpha(t_r, \mathcal{T}_i) \equiv \lambda_\alpha(t_r, \mathcal{T}_i) - \frac{1}{M} \sum_{j=1}^M \lambda_\alpha(t_r, \mathcal{T}_j), \quad (5.46)$$

where the second term on the right hand is an average over configurations in the sample. In particular, we are interested in possible correlations between the fluctuations happening at different slice times in the same configuration.

Using the standard definition, we obtain the *cross-correlation functions*  $C_\alpha$  across the slices and for each eigenvalue  $\alpha$ :

$$C_\alpha(t_r) = \frac{\langle \delta\lambda_\alpha(t_r, \mathcal{T}_i) \delta\lambda_\alpha(0, \mathcal{T}_i) \rangle}{(\langle \delta\lambda_\alpha^2(t_r, \mathcal{T}_i) \rangle)^{\frac{1}{2}} \cdot (\langle \delta\lambda_\alpha^2(0, \mathcal{T}_i) \rangle)^{\frac{1}{2}}}, \quad (5.47)$$

where the averages  $\langle \cdot \rangle$  are always taken across the triangulations sampled<sup>16</sup>. The result of this computation is displayed in the top panel of figure 5.12, whereas the bottom panel shows the distribution of eigenvalues.

First of all, we notice that the curves associated to different eigenvalues exhibit approximately the same behavior. Neglecting the noise coming from the stalk (for  $|t_r| \gtrsim 20$ ), it is apparent the presence of a positive correlation for slices near the center of volume and negative correlation for slices in the tails. This behaviour could be explained by the following reasoning: the value of the  $\alpha$ -th eigenvalue  $\lambda_\alpha$  depends on the total volume of the slice, since eigenvalues computed from the Laplace-Beltrami matrix are bounded in the range  $[0, 8]$ , and they become more denser for higher volumes. Moreover, the total spatial volume is kept fixed, and therefore, a fluctuation of volume in a slice on the tails would be followed by a fluctuation with opposite

---

<sup>16</sup>To estimate the errors on the averages we applied a bootstrap resampling methods, as usual.

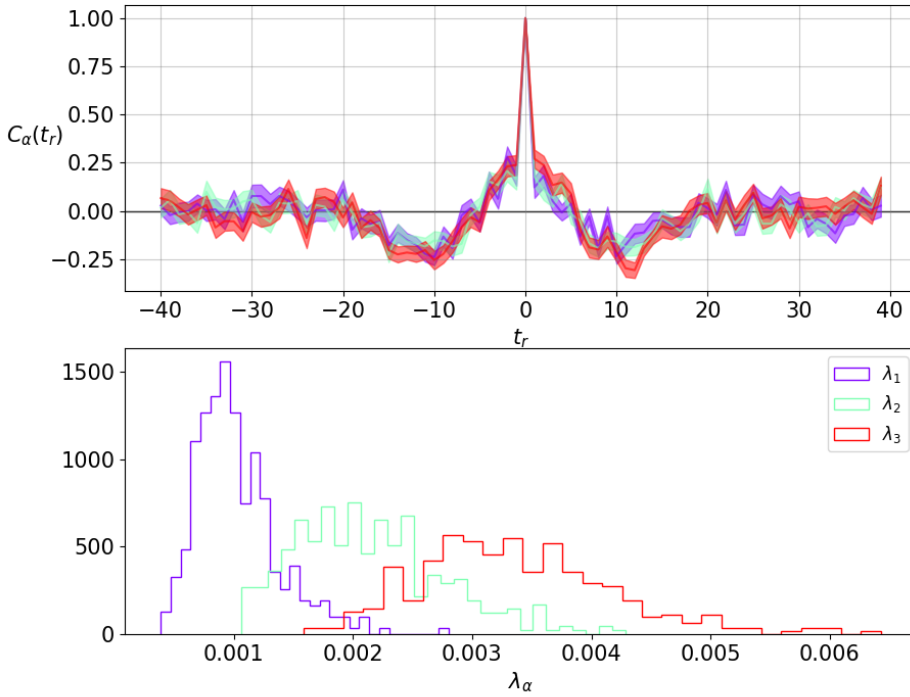


Figure 5.12: Correlation function  $C_\alpha(t_r)$  (top panel) and histograms for the first three (non-null) eigenvalues from a set of independent simulations with in the de Sitter phase with spatial volume fixing  $N_4^{(4,1)} = 80k$  and  $T = 80$  slices. The histograms are computed by measuring eigenvalues on the slice of center of mass.

sign of the volume somewhere else, but more probably inside the blob.

This is also supported by figure 5.13, which shows the correlation function of fluctuations in the spatial volume with respect to the slice in the center of volume.

From this analysis it seems that the spatial volume plays an important role in determining the correlations between fluctuations of eigenvalues from different slices. This suggests that the whole spectrum of eigenvalues should be rescaled by a factor depending on the spatial volume of the slices in which it is calculated, in order to subtract the contributions from the volume. At this stage of the analysis we cannot conclude yet if the hypothesis of propagation of the slice fractal structures in slice time is supported or not.

## 5.7 Analysis of the spatial scalar curvature

Here we want to apply to the scalar curvature of slices the ideas discussed in 5.1.1, where it is given meaning to the concept of Fourier transform and coarse-graining for observables defined microscopically on tetrahedra barycenters (vertices of the slice graph).

First of all, notice that the (euclidean) scalar curvature of slices is a quantity originally defined on links in the Regge interpretation, not on tetrahedra; this does not

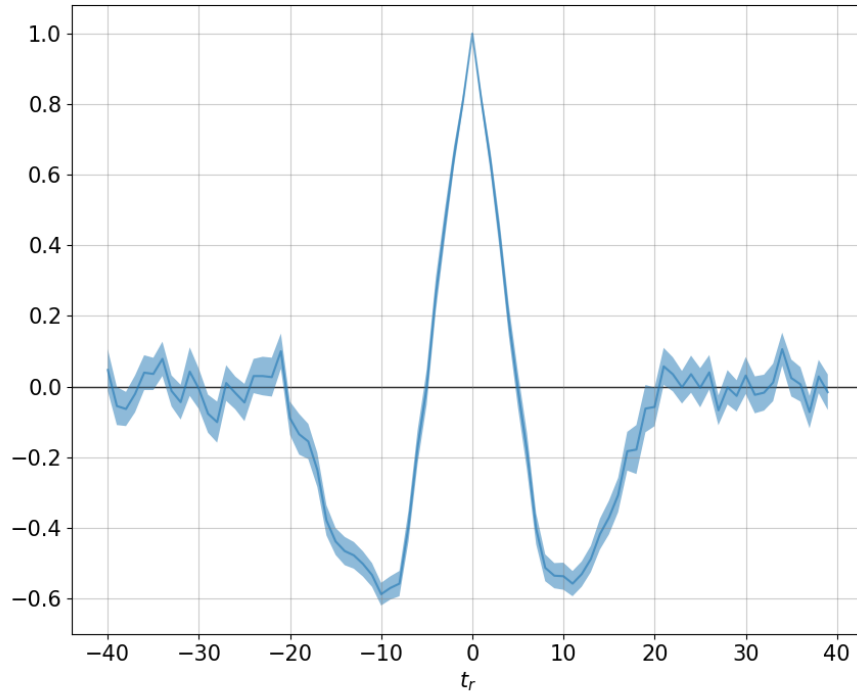


Figure 5.13: Correlation function  $C_V(t_r)$  of the volume. Same dataset of figure 5.12.

pose a conceptual problem for the large-scale analysis, since it is sufficient to *shift locally* the information from links to tetrahedra barycenter, and this procedure does not affect the large scale behaviour of the observable.

All we need to implement the local shift of the scalar curvature is a computation of the dihedral angle between spatial triangles sharing a link, and a new field in the links data structure containing their “spatial” coordination number (number of spatial tetrahedra owning a link); some details can be found in appendix B.

At the end, we obtain a function  $R : V \rightarrow \mathbb{R}$  (or vector  $\vec{R} \in \mathbb{R}^{|V|}$ ) representing the curvature distributed on vertices of the slice graph (tetrahedra barycenters).

Applying eq. (5.22) to  $R(v)$  we obtain the coefficients for the graph Fourier transform

$$\hat{R}_\alpha \equiv \sum_{v \in V} R(v) e_\alpha(v) \equiv (\vec{R}, \vec{e}_\alpha) \quad \forall \vec{e}_\alpha \in \mathcal{B}_G, \quad (5.48)$$

where the eventuality of degeneracies in the spectrum ( $\mu_\alpha \geq 2$ ) have been neglected (as is almost always the case for random graphs), and  $\vec{e}_\alpha \equiv \vec{e}_{\alpha,0}$ .

In continuum spectral analysis, the Fourier transform of a function  $f \in L^2(\mathbb{R})$  is a new function  $\hat{f} \in L^2(\mathbb{R})$ , and the most familiar way to represent these is probably by making plots of the ordered pairs  $\{(x, f(x))\}_{x \in \mathbb{R}}$  and  $\{(k, \hat{f}(k))\}_{k \in \mathbb{R}}$ ; recall that the eigenvalues of the Laplace operator in  $\mathbb{R}$  are  $\lambda_k = -k^2$ , where  $k \equiv |\lambda_k|^{\frac{1}{2}}$  is the same used in the plot of the Fourier-transformed function  $\hat{f}(k)$ .

So, by analogy, it is natural to represent the discrete scalar curvature on the graph by a scatter plot of the ordered pairs

$$\{(0, \hat{R}_0)\} \cup \{(|\lambda_\alpha|^{\frac{1}{2}}, |\hat{R}_\alpha|)\}_{\alpha=1,1,2,\dots}, \quad (5.49)$$

where, except for the component  $\alpha = 0$ , we chose to take the absolute value of the curvature, since the sign of the eigenvectors is arbitrary.

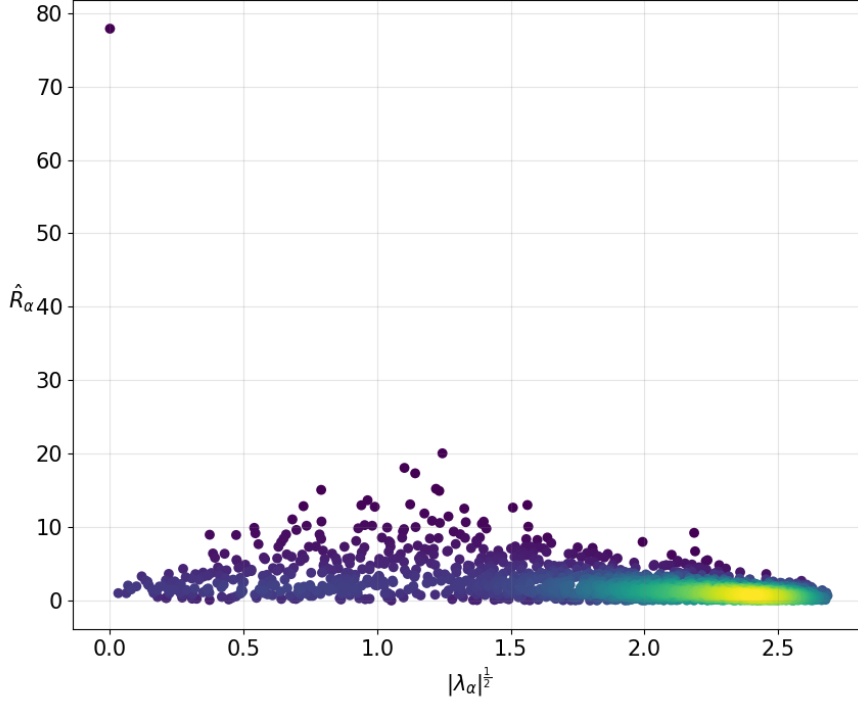


Figure 5.14: Fourier transform of the spatial scalar curvature (in the sense specified in the text) for a slice in the center of volume of a configuration well inside the de Sitter phase ( $k_0 = 2.2, \Delta = 0.6$ ) and with spatial volume fixing  $N_4^{(4,1)} = 80k$ . Brighter colors are proportional to an higher density of eigenvalues. Moreover, recall that eigenvalues are bounded in the range  $[0, 8]$ ; this is why the right limit of the abscissa is  $\sqrt{8} \simeq 2.83$ .

The Fourier transform of the spatial scalar curvature on a typical slice in the center of volume of a configuration in the de Sitter phase is shown in figure 5.14.

First of all, notice that the isolated dot, corresponding to the 0-th eigenvalue with  $\lambda_0 = 0$ , is nothing more than the average of the curvature over the slice (since  $\vec{e}_0 = \frac{1}{|V|}\vec{1}$  is uniform), resulting of positive value.

No well defined curve seems to emerge, but we notice what seems a relevant contributions from intermediate wavelength (recall the eigenvalue/wavelength relation  $l_\alpha \equiv \frac{2\pi}{|\lambda_\alpha|^{\frac{1}{2}}}$  discussed in 5.1.1).

In order to analyze data from simulations though, we need to define somewhat a procedure of average over different configurations.

Our strategy (non necessarily the best one) has been the following: we considered a sample of slices in the center of volume of possibly independent configurations in the de Sitter phase, and with fixed spatial volume  $N_4^{(4,1)} = 80k$ , and gathered all the lists of pairs  $(|\lambda_\alpha|^{\frac{1}{2}}, \hat{R}_\alpha)$  computed from each of them in a unique list of pairs. Then we made a binning in the  $k \equiv |\lambda|^{\frac{1}{2}}$  axis and averaged both coordinates of the points inside the bins, obtaining the red curve in figure 5.15.

This result is somewhat unexpected: the “bump” in this kind of “averaged curva-

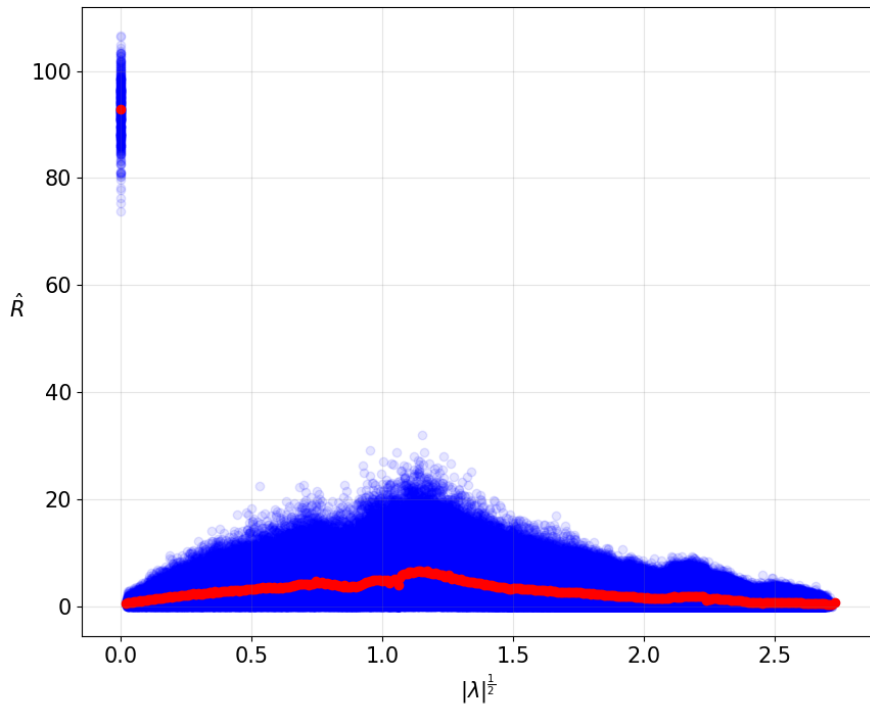


Figure 5.15: Binned average of eigenvalues and curvature

ture” at intermediate scales does suggests that spatial slices in the de Sitter phase have an internal structure richer than we thought at first sight. In particular, the visualization by means of eigenmaps could not probe there, since it can be applied only to describe large scale features, encoded in the lowest eigenvalues, and therefore only in the tiny region near  $\lambda = 0$ .

In any case, further work is required, and it would be interesting to repeat the analysis at different points of the phase diagram, especially by using the spectral methods generalized to the full triangulation, which will be presented in the following section.

## 5.8 Generalizations of the Laplace-Beltrami analysis

In this section we will discuss some ideas on generalizations and applications of the Laplace-Beltrami analysis that, because of constraints on time and resources, could not be implemented in this thesis and will be hopefully investigated in future works.

### 5.8.1 Generalization to the full triangulation

Even if we did extract interesting information about the geometry of slices, the analyses we did are still at a rudimentary stage, and further generalizations needs to be carried out, in order to make them useful to analyze full 4-dimensional geometries. It is highly likely that the geometric information residing within slices is insufficient

to characterize triangulations.

The reason why we have chosen to preliminarily apply the Laplace-Beltrami analysis on spatial slices and not on full spacetimes should be evident.

Indeed, the advantage of investigating spatial slices is that they are made by identical tetrahedra, whose barycenters are connected by edges with the same length size  $a$ ; a graph  $G = (V, E)$  is sufficient to describe the geometry of a slice without having to resort to other properties of the simplicial manifold, since the distinction between tetrahedra is encoded completely into adjacency relations.

The same reasoning does not apply to general triangulations, where simplices could have different edge lengths between them. Actually, the method used for slices can be applied, without modifications, to DT configurations, and CDT configuration with  $\Delta = 0$ , but we have not tested these cases however. In the general case, in CDT one should take into account the two different structures<sup>17</sup> of pentachoron types.

However, as we will discuss next, it is possible to compute eigenvalues and eigenvectors of the Laplace-Beltrami operator for a generic triangulation, even made by all different simplices, by means of a suitable modification to the eigenvalue equation (5.16).

This approach is based upon the *Finite Element Method* (FEM for short) [31], extensively studied and applied in many fields; here we will only make a brief introduction to the main ideas without bothering with details.

For simplicity consider the Poisson equation in a smooth manifold  $\mathcal{M}$  without boundaries:

$$\nabla^2 u(x) = f(x), \quad (5.50)$$

where  $u$  and  $f$  are functions in the Sobolev space  $H^1(\mathcal{M})$ <sup>18</sup>.

Multiplying both sides of eq. (5.50) by a arbitrary smooth test function  $\phi$ , we can put the problem in a form more convenient for our purposes, the so called *weak-form*:

$$\int_{\mathcal{M}} dx \phi(x) \nabla^2 u(x) = \int_{\mathcal{M}} dx \phi(x) f(x), \quad (5.51)$$

Integrating by parts becomes

$$-\int_{\mathcal{M}} dx \vec{\nabla} \phi(x) \cdot \vec{\nabla} u(x) = \int_{\mathcal{M}} dx \phi(x) f(x), \quad (5.52)$$

where the surface term is zero since the manifold is boundaryless<sup>19</sup>  $\partial\mathcal{M} = \emptyset$ .

Consider now a base of functions  $\{\phi_k(x)\}$  for the space  $H^1(\mathcal{M})$ . The functions  $u$  and  $f$  can be expanded in this base

$$u(x) = \sum_k u_k \phi_k(x), \quad (5.53)$$

$$f(x) = \sum_k f_k \phi_k(x), \quad (5.54)$$

---

<sup>17</sup>modulo time-reversal

<sup>18</sup> $H^1(\mathcal{M})$  is the (vector) space of  $L^2(\mathcal{M})$ -functions with first derivatives also contained in  $L^2(\mathcal{M})$ .

<sup>19</sup>This request is not necessary, but makes the argument simpler.

and substituting  $\phi := \phi_j$  in eq. (5.52) we get the equation

$$-\sum_k u_k \int_{\mathcal{M}} dx \vec{\nabla} \phi_j(x) \cdot \vec{\nabla} \phi_k(x) = \sum_k f_k \int_{\mathcal{M}} dx \phi_j(x) \phi_k(x). \quad (5.55)$$

At this point it is convenient to define following matrices:

$$L_{i,j} \equiv \int_{\mathcal{M}} dx \vec{\nabla} \phi_i(x) \cdot \vec{\nabla} \phi_j(x), \quad (5.56)$$

$$M_{i,j} \equiv \int_{\mathcal{M}} dx \phi_i(x) \phi_j(x). \quad (5.57)$$

so that eq. (5.55) can be read

$$-L\vec{u} = M\vec{f}. \quad (5.58)$$

Substituting  $f(x) \equiv -\lambda u(x)$  in eq. (5.58) we obtain

$$L\vec{u} = \lambda M\vec{u}, \quad (5.59)$$

which should remind the reader of the eigenvalue problem (5.16) for the Laplace-Beltrami matrix, apart from the presence of  $M$ .

The Finite Element Methods consists in approximating the Sobolev space by working with a basis  $\{\phi_k\}$  for a finite subspace  $V \subset H^1(\mathcal{M})$ ; furthermore these function are chosen in such a way that their support  $\{\mathcal{D}_k\}$  cover the manifold, but each one intersects only with few others<sup>20</sup>.

For piecewise-linear manifolds embeddable in an Euclidean space  $\mathbb{R}^D$ , like CDT triangulations after Wick-rotation, we can choose as basis the set of piecewise-linear functions  $\{\phi_k : \mathbb{R}^D \rightarrow \mathbb{R}\}$  which are 1 on the triangulation vertex labeled  $k$  and 0 outside the simplices containing it.

The function  $\phi_k$  and  $\phi_q$  will be overlapping only if the vertices labeled  $k$  and  $q$  in the triangulation are connected by a link. so the matrices  $L$  and  $M$  will be sparse, like for the graph case.

Regarding general triangulations, one should compute, for each pair of vertices the integrals represented by the matrices  $L$  and  $M$  defined respectively in eq. (5.56) and (5.57). Fortunately, for CDT triangulations, only a finite and pre-computable set of distinct elements needs to be calculated, since the types of simplices in a causal triangulation is limited.

The only things left in order to proceed along this direction, are a careful computation of the distinct coefficients for  $L$  and  $M$  for different values of the space-time asymmetry parameter  $\Delta$ , and actually solving the modified eigenvalue equation (5.58).

We hope for the future to have the possibility of implementing these ideas to exploit fully in CDT the insight coming from a spectral analysis of discretized manifolds.

---

<sup>20</sup>This property also should be reminiscent of the sparse adjacency relations between elements of a graph approximating a manifold, where localized supports take the role of vertices and the overlap between neighbouring supports take the role of links.

### 5.8.2 Applications to matter coupling

The procedure explained 5.2.1 and applied to the curvature in section 5.7, can be employed for analyzing the behaviour of any quantity defined on maximal simplices, or any microscopical structure which could be “shifted” there without affecting the large scale properties of its distribution.

In particular, the Laplace-Beltrami analysis of the full spacetime could be useful to study the large scale behaviour of matter fields, which degrees of freedom are localized into pentachorons of CDT triangulations in the same way in which they are localized on sites of hypercubic lattices in QFT simulations.

For example, the form of the path-integral used to represent CDT coupled to a scalar field is the following [32]<sup>21</sup>

$$Z = \sum_{\mathcal{T} \in \mathcal{S}} \int \prod_{p \in \mathcal{T}^{(4)}} d\phi(p) \frac{1}{C(\mathcal{T})} \exp(-S_{CDT}[\mathcal{T}] - S_M[\phi, \mathcal{T}]), \quad (5.60)$$

where  $\mathcal{T}^{(d)}$  is the set of pentachorons,  $S_{CDT}$  is the usual action for pure-gauge CDT,  $C(\mathcal{T})$  is the symmetry factor, discussed in 3.1, which enumerates the automorphisms of the triangulation  $\mathcal{T}$  (and can be neglected, usually), whereas the matter action term is taken to have only a kinetic term of the form:

$$S_M[\phi, \mathcal{T}] = \frac{1}{2} \sum_{\langle p_1 \leftrightarrow p_2 \rangle_{\mathcal{T}}} (\phi(p_1) - \phi(p_2))^2, \quad (5.61)$$

where the sum is over all adjacent pentachorons, denoted by  $\langle p_1 \leftrightarrow p_2 \rangle_{\mathcal{T}}$ , and dependent on the configuration  $\mathcal{T}$ .

Notice that the matter action term is a quadratic form  $\phi^T \tilde{L} \phi$ , where  $\tilde{L}$  would be the Laplace-Beltrami matrix of the triangulation if we neglect the space-time asymmetry parameter  $\Delta$  and consider the graph made by pentachorons.

Our proposal, is to study the behaviour of the Fourier transform of the scalar field  $\hat{\phi}$  as a function of  $k \equiv |\lambda|^{\frac{1}{2}}$ , by following the method explained in 5.1.1, and applied in section 5.7 for the case of scalar curvature. In this way, we hope to obtain an interesting coarse grained description of the field. In particular, if the Fourier transform of the field would present an exponential decay in the  $k$ , we could immediately recognize a properly defined correlation length!

---

<sup>21</sup>Actually, the equation discussed in [32] is referred to the 2-dimensional case. But we found no reasons why not to extend it to 4 dimensions.

# Chapter 6

## Conclusions

Even if the Quantum Gravity approach of Causal Dynamical Triangulations has provided many interesting results and insights, there are still many open questions and directions that could be explored further. Of utmost importance is the search for a continuum limit, which is currently being investigated by the CDT community. If attainable, the continuum limit would be represented by a point in the phase diagram of the theory, where a continuous order critical transition occurs jointly to the divergence of correlation lengths. However, we find that the actual lack of a proper and non-ad-hoc set of local observables, which would characterize the geometry of triangulations up to microscopic scales, is a serious open problem that needs to be tackled and should not be underestimated, since it allows to define an associated set of correlation lengths, which, at the present day, is not available yet.

If the CDT community do not solve the correlation length issue, we think it would be impossible to determine if a critical point indeed exhibits a continuum limit or not, even if the transition is found to be of continuous order by other means, for example by studying order parameters.

Other issues we identified are bound to the more technical problem of efficiency in numerical simulations. On one hand there is the effect of *slowing down* for simulations at the vicinity of critical transition lines; this is common to all numerical approaches to quantum field theories, and is represented by a divergent increase in the autocorrelation times for measured observables, corresponding in turn to long times for simulations before useful (independent) data could be extracted.

This fact raises the need to find always better algorithms in order to get reasonable times of simulations. If the situation in CDT simulations is not dramatical yet, it would certainly be when higher volumes will be investigated, resulting in the difficulty to properly analyze.

In this thesis we chose to investigate and seek solutions to the problems of algorithmic efficiency and lack of local observables outlined above, since they are both functional to a serious research of the continuum limit.

Regarding algorithmic efficiency, we analyzed carefully the standard implementation, and identified the slowest modes for simulations in the  $C_{dS}$  and  $C_b$  phases (see 4.1.1), the most interesting phases in CDT, either for their resemblance to the de Sitter phase, and because continuous order transition line separating them would hopefully allow for a continuum limit. From the blob/tails/stalk structure of configurations in the  $C$  phases, we found that the lowest mode is the one associated

to the time translational mode of blob variables like the time labels of the slices corresponding to the center of volume, and the fluctuations in the location of tails; this would result in a (quasi) random walk of these variables in simulation time. Our focusing on a cure for the slowest modes in simulations was motivated by the observation that relevant observables could depend non-trivially on these modes, resulting in autocorrelation times dominated by them. In particular, the standard algorithm performs moves selecting uniformly simplices from the whole set of simplices, but most of them are located in the blob, resulting in a suppressed evolution of the tails.

Our analysis of the standard algorithm has led us to generalization into a new family of algorithms, that we called *BlockLocal* (see section 3.4), and for which a specific subclass, dubbed *TBlocked*, evolves the configurations by selecting simplices more ‘democratically’ in slice time. This is implemented by distributing information about simplices into adjacent regions of spacetime we called *blocks*; the standard algorithm is modified by the introduction of a block selection, and then by a standard selection restricted within the block. In this way, subdividing for example the triangulation into two blocks, one containing the blob interior, and the other containing the tails, guarantees a faster evolution of the tails.

In chapter 4, our implementations of the standard and TBlocked algorithms were tested in correctness and in efficiency. While both algorithms seem to reproduce the sufficiently compatible behaviour, the hopes on an improvement in efficiency in favour of the the TBlocked algorithm were not satisfied. Performing a careful analysis of the autocorrelation times and relative speeds for the two algorithms, their performance is quite similar. However even if the results in performance of the TBlocked algorithm are not outstanding, the class of BlockLocal algorithms is sufficiently general to provide a base to construct efficient algorithms in the future. In particular, the distribution of simplices information into (almost) separate regions of spacetime makes possible to implement a parallelization of the algorithm where each block is evolved independently from the others, except for boundary information, that must be properly transmitted between processors. This would means, for example, that a parallelized TBlocked algorithm with  $n$  blocks distributed among  $n$  processors would be, in the best scenario,  $n$  times faster than the serialized TBlocked. Unfortunately, for time and resource constraints, we have not implemented a parallelized version of the TBlocked algorithm yet, but we hope in the future to explore this direction further.

Regarding the issue of lacking definitions for observables, we found it wise to focus on recent techniques from Mathematics and Computer Science. In the age of full bloom for disciplines like Machine learning, shape recognition, imaging and many others, the techniques to extract and analyze features from complex geometric data, and the possibilities to implement them have evolved in an stately way. Our intent was to apply some of these ideas to CDT, by studying preliminarily the geometries of slices due to their simple structure.

Since spatial slices can be faithfully represented by regular graphs where tetrahedrons take the role of vertices and adjacency relations between tetrahedrons take the role of links, the most natural choice was to resort to methods from *spectral graph analysis*, which studies the many properties of the eigenvalues and eigenvectors of

the Laplace-Beltrami matrix of graphs<sup>1</sup>.

Indeed, the Laplace-Beltrami operator is undoubtedly one of the most important objects in physics, since Fourier analysis is nothing more than an decomposition into its eigenspaces.

The famous words “Can One Hear the Shape of a Drum?” by Mark Kac [21] well represent the idea that analyzing the spectrum of eigenvalues of the Laplace-Beltrami operator one can learn quite a lot from a geometry. Furthermore, the discretized version of the Laplace-Beltrami operator allows also for an interpretation similar to that of continuous cases and in particular, it is useful to discriminate the characteristic scales of the discrete geometry. We found this property well suited to describe the behaviour of observables defined at the microscopic scales of the random geometries generated by CDT simulations, since it defines how that observable behaves at different scales, and in particular allows for a coarse graining of that observable in the form of a cut-off of the Fourier components associated to high eigenvalues (small wavelengths).

By studying the eigenspectrum and eigenvalues of the Laplace-Beltrami matrix of graphs associated to slices, we have obtained various interesting qualitative and quantitative results, and we have questioned the physical interpretation of slices and their relation with the full spacetime, considering also partial results coming from other methods. In particular, by studying the first eigenvectors, associated to the lowest eigenvalues and corresponding to large-scale descriptors of geometry, we observed that, even if the topology of the slices is fixed to the one of a 3-sphere  $S^3$ , the geometry of slices for a typical configuration in the de Sitter phase is completely different. This observation could also be inferred from the fractional value of the spectral dimension on slices ( $d \simeq \frac{3}{2}$ ).

However, a complete analysis of discrete spacetimes would require to take into account the geometry of the full triangulation. A different, but conceptually equivalent, form of the spectral analysis we did for spatial slices, can be performed, also to full triangulations. However, for the reasons explained in subsection 5.8.1 it does require some implementative efforts, and, again for time constraints, we could not pursue this direction further. Nevertheless, again in subsection 5.8.1, we explained the ideas about how to actually implement the analysis in general. In the future, we hope to implement this generalization in order to propose a definition of correlation length for pure-gauge and matter-coupled CDT, based on local observables like the scalar curvature, defined à la Regge as associated to  $(d - 2)$ -simplices.

---

<sup>1</sup>As follows from the discussion in section 5.1, the Laplace-Beltrami matrix on a lattice or graph is a discretization of the definition of the Laplace-Beltrami operator on a manifold which the lattice or graph are approximating.

# Appendix A

## Data structures

Here we will give a schematic definition of the data structures, representing triangulations, used in the codes for Monte Carlo simulations.

A causal triangulation in 4 dimensions can be completely specified, in principle, simply by the adjacency relations between labeled pentachorons and the time label of their vertices. However, configurations would be updated during simulations, and many checks necessary to perform the moves would be extremely complicated to implement using merely this minimal-memory representation<sup>1</sup>.

It is then convenient to maintain data structures encoding information about the types of simplices that are selected during moves. Furthermore, no information about tetrahedra needs not to be maintained.

### A.1 Data structures for the standard implementation

The 4-dimensional Alexander moves described in 3.2.3 suggest to maintain information about the following special types of simplices:

- vertices with coordination 8,
- spatial links with coordination 6,
- timelike links with coordination 4,
- spatial triangles with coordination 4,
- timelike triangles with coordination 3,
- pentachorons of type (4, 1) or (1, 4),
- pentachorons of type (3, 2) or (2, 3).

---

<sup>1</sup>The minimal-memory representation is actually useful to store configurations space-efficiently, so that a data-compression and data-reconstruction is performed whenever one saves or load a configuration file.

In the computations of selection probabilities we need to count how many simplices of the types listed above are present in the triangulation, so it is useful to define global variables encoding these numbers, as defined in the following table<sup>2</sup>:

<code>num0</code>	total number of vertices
<code>num80</code>	number of vertices with coordination 8
<code>num1</code>	total number of links
<code>num61s</code>	number of spatial links with coordination 6
<code>num41t</code>	number of timelike links with coordination 4
<code>num2</code>	total number of triangles
<code>num42s</code>	number of spatial triangles with coordination 4
<code>num32t</code>	number of timelike triangles with coordination 3
<code>num4</code>	total number of pentachorons
<code>num444</code>	number of pentachorons of types (4, 1) or (1, 4)

To each  $k$ -simplices in the triangulation (except for tetrahedra) a unique label<sup>3</sup> is assigned to distinguish it from other  $k$ -simplices.

This label is used to access and modify data structures of the individual simplex to which it refers.

Recall that for each Monte Carlo steps one first selects the move type, and then select a simplex characterizing the initial cell for the move (see the example in 3.3.1); in 4-dimensional simulations, this selection can be implemented efficiently by maintaining the following lists of labels, where the ranges of indices associated to a given type of simplex is specified:

- `list0`:
  - $[0, \text{num80} - 1]$ : vertices with coordination 8,
  - $[\text{num80}, \text{num0}]$ : other types of vertices;
- `list1`:
  - $[0, \text{num61s} - 1]$ : spacelike links with coordination 6,
  - $[\text{num61s}, \text{num61s} + \text{num41t} - 1]$ : timelike links with coordination 4,
  - $[\text{num61s} + \text{num41t}, \text{num1} - 1]$ : other types of links,
- `list2`:
  - $[0, \text{num42s} - 1]$ : spacelike triangles with coordination 4,
  - $[\text{num42s}, \text{num42s} + \text{num32t} - 1]$ : timelike triangles with coordination 3,
  - $[\text{num42s} + \text{num32t}, \text{num2} - 1]$ : other types of triangles,
- `list4`:
  - $[0, \text{num444} - 1]$ : pentachorons of types (4, 1) or (1, 4),
  - $[\text{num444}, \text{num4}]$ : pentachorons of types (3, 2) or (2, 3).

<sup>2</sup>As for names, in our code we used the same conventions employed in the code gently provided by the group of Ambjörn et al.

<sup>3</sup>We used non-negative integers as labels.

In the following we report the definition of the data structures of individual simplices:

```

struct Vertex{ // Vertex data structure
    int id;           // index in list0
    int t_slice;      // time label of the slice
    int coord_num;    // number of adjacent Pentas
    Label near_p;     // label of a neighbouring Penta
    int r;            // index in mV ()
};

struct Link{ // Link data structure
    int id;           // index in list1
    Label v[2];        // labels owned vertices
    int coord_num;    // number of adjacent Pentas
    Label near_p;     // label of a neighbouring Penta
};

struct Triangle{ // Triangle data structure
    int id;           // index in list3
    Label v[3];        // labels of owned vertices
    int coord_num;    // number of adjacent Pentas
    Label near_p;     // label of a neighbouring Penta
};

struct Penta{ // Pentachoron data structure
    int id;           // index in list4
    Label v[5];        // labels of owned Vertices
    Label l[10];       // labels of owned Links
    Label t[10];       // labels of owned Triangles
    Label n[5];        // labels of adjacent Pentas (opposite to vertices)
};

```

Finally, arrays containing (instances of) such objects must be maintained, and the label of a simplex is used as an index for the corresponding array:

<b>verts</b>	array of <b>Vertex</b> objects
<b>links</b>	array of <b>Link</b> objects
<b>tris</b>	array of <b>Triangle</b> objects
<b>pentas</b>	array of <b>Penta</b> objects

Selecting a label from one of the ranges in above, allow the access to the data structure of that specific simplex type.

For example, in the  $(8 \rightarrow 2)$  move a random vertex of coordination 8 must be selected, so one first of all generates a random integer  $i$  in the range  $[0, \text{num80} - 1]$  and get the label  $v$  of the corresponding vertex by the assignment  $v = \text{list0}[i]$ . Then the actual **Vertex** object can be accessed by **verts**[ $v$ ]. The information about the full cell for the move  $(8 \rightarrow 2)$  can be reconstructed thanks to the field **near\_p** of the **Vertex** structure, which allow the access to a pentachoron (labeled **near\_p**) owning that vertex.

## A.2 Data structures for the TBlocked implementation

The main difference between our implementations of the standard and TBlocked algorithm is the presence of a covering of (overlapping) blocks to which a given simplex may or may not belong.

In section 3.4 we explained that, for each move, a preliminary selection of a random block is performed, and then a selection of a simplex characterizing the initial cell of the move must be carried out inside that block.

Therefore, for each block labeled `bid` the selection must be restricted inside the block, and we need separate lists `klistX[bid]` and counting variables `knumY[bid]`, defined in a way exactly analogous to `listX` and `numY`.

Data structures for the individual simplices differ from the standard ones only by the presence of fields specifying the block `bid` (or blocks) to which they belong, and the index `kid` (or indices) of the corresponding list `klistX[bid]`. If the simplex accessed is shared by two blocks the fields `bid2` and `kid2` are used, otherwise `bid2` is set to `-1`.

```

struct Vertex{ // Vertex data structure (TBlocked)
    int id;           // index in list0
    int bid;          // block label (no bid2 for vertices)
    int kid;          // index in klist0[bid]
    int t_slice;      // time label of the slice
    int coord_num;   // number of adjacent Pentas
    Label near_p;    // label of a neighbouring Penta
    int r;            // index in mV ()
};

struct Link{ // Link data structure (TBlocked)
    int id;           // index in list1
    int bid;          // primary block label
    int kid;          // index in klist1[bid]
    Label v[2];       // labels owned vertices
    int bid2;         // secondary block label (-1 if non-existent)
    int kid2;         // index in klist1[bid2] if bid2 > -1
    Label v[2];       // labels owned vertices
    int coord_num;   // number of adjacent Pentas
    Label near_p;    // label of a neighbouring Penta
};

struct Triangle{ // Triangle data structure (TBlocked)
    int id;           // index in list3
    int bid;          // primary block label
    int kid;          // index in klist1[bid]
    Label v[2];       // labels owned vertices
    int bid2;         // secondary block label (-1 if non-existent)
    int kid2;         // index in klist2[bid2] if bid 2> -1
};

```

```

Label v[3];           // labels of owned vertices
int coord_num;        // number of adjacent Pentas
Label near_p;         // label of a neighbouring Penta
};

struct Penta{ // Pentachoron data structure (TBlocked)
    int id;             // index in list4
    int bid;             // primary block label
    int kid;             // index in klist1[bid]
    Label v[2];          // labels owned vertices
    int bid2;            // secondary block label (-1 if non-existent)
    int kid2;            // index in klist2[bid2] if bid > -1
    Label v[5];          // labels of owned Vertices
    Label l[10];          // labels of owned Links
    Label t[10];          // labels of owned Triangles
    Label n[5];          // labels of adjacent Pentas (opposite to vertices)
};

```

# Appendix B

## Scalar curvature on the slices

Here we will show how to compute the scalar curvature on  $d$ -dimensional spatial slices and “shift” this information from  $(d - 2)$ -simplices to barycenters of  $d$ -simplices<sup>1</sup>.

For simplicity let us consider the 2-dimensional case first, where the Regge scalar curvature is encoded on the vertices  $\{\tilde{v}\}$  of the triangulated slice by the formula<sup>2</sup>

$$R_{\tilde{v}} \equiv 2 \varepsilon_{\tilde{v}} \text{vol}(\tilde{v}) = 2(2\pi - \beta_2 n_{\tilde{v}}) = 2\pi(2 - \frac{n_{\tilde{v}}}{3}), \quad (\text{B.1})$$

where  $\beta_2 \equiv \frac{\pi}{3}$  is simply the (dihedral) angle between links of equilateral triangles, and  $n_{\tilde{v}}$  is the number of triangles sharing the vertex  $\tilde{v}$ ; for convenience let us call it the *spatial coordination number*.

We want to distribute the scalar curvature from vertices to triangle barycenters, that we will indicate with the variable  $v$  since they corresponds to vertices of the graph dual to the slice. The curvature associated to each vertex  $\tilde{v}$  of the triangulation should be distributed equally amongst the neighbouring triangles so that the “shifted” curvature could be written by the formula

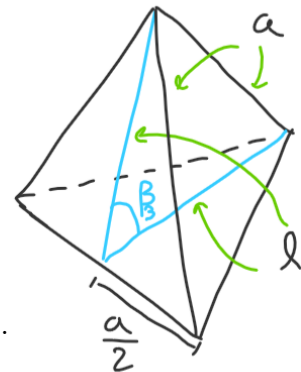
$$R_v \equiv \sum_{\tilde{v} \in \mathbb{V}_v} \frac{R_{\tilde{v}}}{n_{\tilde{v}}} = 2\pi \sum_{\tilde{v} \in \mathbb{V}_v} \left( \frac{2}{n_{\tilde{v}}} - \frac{\beta_2}{\pi} \right) = 4\pi \sum_{\tilde{v} \in \mathbb{V}_v} n_{\tilde{v}}^{-1} - 2\beta_2 \cdot \frac{d(d+1)}{2}, \quad (\text{B.2})$$

where  $\mathbb{V}_v$  is the set of vertices  $\tilde{v}$  of the triangulation which belong to the triangle with barycenter  $v$

The case of 3-dimensional slices is only slightly more involved, since we need an explicit expression of the (dihedral) angle  $\beta_3$  between triangles of the same tetrahedron.

The draw on the right comes to help, and  $\beta_3$  can be found by solving the system:

$$\begin{cases} a = 2l \sin(\frac{\beta_3}{2}); \\ l = \sqrt{a^2 - (\frac{a}{2})^2} = \frac{\sqrt{3}}{2}a; \end{cases} \implies \beta_3 = 2 \arcsin\left(\frac{1}{\sqrt{3}}\right) \simeq 1.23. \quad (\text{B.3})$$



<sup>1</sup>Here  $d$  is the dimension of maximal simplices in spatial slices, not the dimension of the full spacetime triangulation.

<sup>2</sup>By convention  $\text{vol}(\tilde{v}) = 1$ .

Finally, the 4-dimensional version of equation (B.2) becomes

$$R_v \equiv \sum_{\tilde{l} \in \mathbb{L}_v} \frac{R_{\tilde{l}}}{n_{\tilde{l}}} = 2\pi \sum_{\tilde{l} \in \mathbb{L}_v} \left( \frac{2}{n_{\tilde{l}}} - \frac{\beta_3}{\pi} \right) = 4\pi \sum_{\tilde{l} \in \mathbb{L}_v} n_{\tilde{l}}^{-1} - 2\beta_3 \cdot \frac{d(d+1)}{2} = 4\pi \sum_{\tilde{l} \in \mathbb{L}_v} n_{\tilde{l}}^{-1} - 24 \arcsin \frac{1}{\sqrt{3}}, \quad (\text{B.4})$$

where  $\mathbb{L}_v$  is the set of links  $\tilde{l}$  of the triangulation which belong to the tetrahedron with barycenter  $v$ , and  $n_{\tilde{l}}$  is the spatial coordination number of the link  $\tilde{l}$ .

Eq. (B.4) is the expression actually employed to perform the Fourier transform of the spatial curvature described in section 5.7.

# Bibliography

- [1] Marc H. Goroff and Augusto Sagnotti. “The ultraviolet behavior of Einstein gravity”. In: *Nuclear Physics B* 266.3 (1986), pp. 709 –736. ISSN: 0550-3213. DOI: [http://dx.doi.org/10.1016/0550-3213\(86\)90193-8](http://dx.doi.org/10.1016/0550-3213(86)90193-8).
- [2] D. Oriti, ed. *Approaches to Quantum Gravity. Toward a New Understanding of Space, Time and Matter*. Cambridge University Press, 2009.
- [3] Carlo Rovelli. “Loop Quantum Gravity”. In: *Living Reviews in Relativity* 11.1 (July 2008), p. 5. ISSN: 1433-8351. DOI: [10.12942/lrr-2008-5](https://doi.org/10.12942/lrr-2008-5). URL: <http://dx.doi.org/10.12942/lrr-2008-5>.
- [4] J. Ambjorn et al. “Nonperturbative Quantum Gravity”. In: *Phys. Rept.* 519 (2012), pp. 127–210. DOI: [10.1016/j.physrep.2012.03.007](https://doi.org/10.1016/j.physrep.2012.03.007). arXiv: [1203.3591 \[hep-th\]](https://arxiv.org/abs/1203.3591).
- [5] T. Regge. “General relativity without coordinates”. In: *Il Nuovo Cimento (1955-1965)* 19.3 (1961), pp. 558–571. ISSN: 1827-6121. DOI: [10.1007/BF02733251](https://doi.org/10.1007/BF02733251).
- [6] J. Laiho et al. “Lattice Quantum Gravity and Asymptotic Safety”. In: (2016). arXiv: [1604.02745 \[hep-th\]](https://arxiv.org/abs/1604.02745).
- [7] Tobias Rindlisbacher and Philippe de Forcrand. “Euclidean Dynamical Triangulation revisited: is the phase transition really 1st order? (extended version)”. In: *JHEP* 05 (2015), p. 138. DOI: [10.1007/JHEP05\(2015\)138](https://doi.org/10.1007/JHEP05(2015)138). arXiv: [1503.03706 \[hep-lat\]](https://arxiv.org/abs/1503.03706).
- [8] Jan Ambjorn et al. “On the relation between Euclidean and Lorentzian 2-D quantum gravity”. In: *Phys. Lett.* B475 (2000), pp. 24–32. DOI: [10.1016/S0370-2693\(00\)00058-7](https://doi.org/10.1016/S0370-2693(00)00058-7). arXiv: [hep-th/9912267 \[hep-th\]](https://arxiv.org/abs/hep-th/9912267).
- [9] J. Ambjorn et al. “New higher-order transition in causal dynamical triangulations”. In: *Phys. Rev.* D95.12 (2017), p. 124029. DOI: [10.1103/PhysRevD.95.124029](https://doi.org/10.1103/PhysRevD.95.124029). arXiv: [1704.04373 \[hep-lat\]](https://arxiv.org/abs/1704.04373).
- [10] S. Jordan and R. Loll. “Causal Dynamical Triangulations without preferred foliation”. In: *Physics Letters B* 724.1 (2013), pp. 155 –159. ISSN: 0370-2693. DOI: <http://dx.doi.org/10.1016/j.physletb.2013.06.007>.
- [11] Jan Ambjorn, J. Jurkiewicz, and R. Loll. “Dynamically triangulating Lorentzian quantum gravity”. In: *Nucl. Phys.* B610 (2001), pp. 347–382. DOI: [10.1016/S0550-3213\(01\)00297-8](https://doi.org/10.1016/S0550-3213(01)00297-8). arXiv: [hep-th/0105267 \[hep-th\]](https://arxiv.org/abs/hep-th/0105267).
- [12] Ben Simons. *Phase transitions and collective phenomena*. University of Cambridge, 1997.
- [13] Martin Reuter and Frank Saueressig. “Quantum Einstein Gravity”. In: *New J. Phys.* 14 (2012), p. 055022. DOI: [10.1088/1367-2630/14/5/055022](https://doi.org/10.1088/1367-2630/14/5/055022). arXiv: [1202.2274 \[hep-th\]](https://arxiv.org/abs/1202.2274).

- [14] J. Ambjorn et al. “Renormalization Group Flow in CDT”. In: *Class. Quant. Grav.* 31 (2014), p. 165003. DOI: [10.1088/0264-9381/31/16/165003](https://doi.org/10.1088/0264-9381/31/16/165003). arXiv: [1405.4585 \[hep-th\]](https://arxiv.org/abs/1405.4585).
- [15] Joshua H. Cooperman. “Comments on ”Searching for a continuum limit in CDT quantum gravity””. In: (2016). arXiv: [1604.01798 \[gr-qc\]](https://arxiv.org/abs/1604.01798).
- [16] M.E.J. Newman & G.T. Barkema. *Monte Carlo Methods in Statistical Physics*. Oxford University Press, 1999.
- [17] Marcus Spradlin, Andrew Strominger, and Anastasia Volovich. “Les Houches lectures on de Sitter space”. In: *Unity from duality: Gravity, gauge theory and strings. Proceedings, NATO Advanced Study Institute, Euro Summer School, 76th session, Les Houches, France, July 30-August 31, 2001*. 2001, pp. 423–453. arXiv: [hep-th/0110007 \[hep-th\]](https://arxiv.org/abs/hep-th/0110007).
- [18] Andrzej Goerlich. “Causal Dynamical Triangulations in Four Dimensions”. PhD thesis. Jagiellonian U., Astron. Observ., 2010. arXiv: [1111.6938 \[hep-th\]](https://arxiv.org/abs/1111.6938). URL: <https://inspirehep.net/record/1079199/files/arXiv:1111.6938.pdf>.
- [19] Steven Carlip. “Spontaneous Dimensional Reduction in Short-Distance Quantum Gravity?” In: *AIP Conf. Proc.* 1196 (2009), p. 72. DOI: [10.1063/1.3284402](https://doi.org/10.1063/1.3284402). arXiv: [0909.3329 \[gr-qc\]](https://arxiv.org/abs/0909.3329).
- [20] Franois Treves. “Review: M. A. Shubin, Pseudodifferential operators and spectral theory”. In: *Bull. Amer. Math. Soc. (N.S.)* 19.1 (July 1988), pp. 343–346. URL: <https://projecteuclid.org:443/euclid.bams/1183554660>.
- [21] Mark Kac. “Can One Hear the Shape of a Drum?” In: *The American Mathematical Monthly* 73.4 (Apr. 1966), pp. 1–23. ISSN: 00029890. DOI: [10.2307/2313748](https://doi.org/10.2307/2313748). URL: <http://dx.doi.org/10.2307/2313748>.
- [22] Martin Reuter, Franz-Erich Wolter, and Niklas Peinecke. “Laplace-Beltrami Spectra As ’Shape-DNA’ of Surfaces and Solids”. In: *Comput. Aided Des.* 38.4 (Apr. 2006), pp. 342–366. ISSN: 0010-4485. DOI: [10.1016/j.cad.2005.10.011](https://doi.org/10.1016/j.cad.2005.10.011).
- [23] S. T. Barnard, A. Pothen, and H. D. Simon. “A Spectral Algorithm for Envelope Reduction of Sparse Matrices”. In: *Proceedings of the 1993 ACM/IEEE Conference on Supercomputing*. Supercomputing ’93. Portland, Oregon, USA: ACM, 1993, pp. 493–502. ISBN: 0-8186-4340-4. DOI: [10.1145/169627.169790](https://doi.acm.org/10.1145/169627.169790). URL: <http://doi.acm.org/10.1145/169627.169790>.
- [24] Lawrence Page et al. *The PageRank Citation Ranking: Bringing Order to the Web*. Technical Report 1999-66. Previous number = SIDL-WP-1999-0120. Stanford InfoLab, 1999. URL: <http://ilpubs.stanford.edu:8090/422/>.
- [25] S. Brin and L. Page. “The Anatomy of a Large-Scale Hypertextual Web Search Engine”. In: *Seventh International World-Wide Web Conference (WWW 1998)*. 1998. URL: <http://ilpubs.stanford.edu:8090/361/>.
- [26] M. H. Protter. “Can One Hear the Shape of a Drum? Revisited”. In: *SIAM Review* 29.2 (1987), pp. 185–197. DOI: [10.1137/1029041](https://doi.org/10.1137/1029041). eprint: <https://doi.org/10.1137/1029041>. URL: <https://doi.org/10.1137/1029041>.

- [27] H. P. McKean and I. M. Singer. “Curvature and the Eigenvalues of the Laplacian”. In: *Henry P. McKean Jr. Selecta*. Ed. by F. Alberto Grünbaum, Pierre van Moerbeke, and Victor H. Moll. Cham: Springer International Publishing, 2015, pp. 53–76. ISBN: 978-3-319-22237-0. DOI: [10.1007/978-3-319-22237-0\\_6](https://doi.org/10.1007/978-3-319-22237-0_6). URL: [https://doi.org/10.1007/978-3-319-22237-0\\_6](https://doi.org/10.1007/978-3-319-22237-0_6).
- [28] Conrad Sanderson and Ryan Curtin. “Armadillo: a template-based C++ library for linear algebra”. In: *The Journal of Open Source Software* 1.2 (2016). DOI: [10.21105/joss.00026](https://doi.org/10.21105/joss.00026). URL: <https://doi.org/10.21105/joss.00026>.
- [29] Mikhail Belkin and Partha Niyogi. “Laplacian Eigenmaps and Spectral Techniques for Embedding and Clustering”. In: *Advances in Neural Information Processing Systems 14*. Ed. by T. G. Dietterich, S. Becker, and Z. Ghahramani. MIT Press, 2002, pp. 585–591. URL: <http://papers.nips.cc/paper/1961-laplacian-eigenmaps-and-spectral-techniques-for-embedding-and-clustering.pdf>.
- [30] J. Ambjorn et al. “Euclidian 4d quantum gravity with a non-trivial measure term”. In: *JHEP* 10 (2013), p. 100. DOI: [10.1007/JHEP10\(2013\)100](https://doi.org/10.1007/JHEP10(2013)100). arXiv: [1307.2270 \[hep-lat\]](https://arxiv.org/abs/1307.2270).
- [31] Mats G. Larson and Fredrik Bengzon. *The Finite Element Method: Theory, Implementation, and Applications*. Springer Publishing Company, Incorporated, 2013. ISBN: 3642332862, 9783642332869.
- [32] Jan Ambjorn et al. “The spectral dimension in 2D CDT gravity coupled to scalar fields”. In: *Mod. Phys. Lett. A* 30.13 (2015), p. 1550077. DOI: [10.1142/S0217732315500777](https://doi.org/10.1142/S0217732315500777). arXiv: [1412.3434 \[gr-qc\]](https://arxiv.org/abs/1412.3434).